Cover Page

The handle holds various files of this Leiden University dissertation

Author: Antonov, Pavel
Title: Towards thermo- and superlubricity on the macroscopic scale : from nanostructures to graphene and graphite lubrication
Date: 2017-10-18

Towards thermo- and superlubricity on the macroscopic scale: from nanostructures to graphene and graphite lubrication

Proefschrift

ter verkrijging van
de graad van Doctor aan de Universiteit Leiden,
op gezag van Rector Magnificus prof. mr. C.J.J.M. Stolker,
volgens besluit van het College voor Promoties
te verdedigen op woensdag 18 oktober 2017
klokke 16.15 uur

door

Pavlo Volodymyrovych Antonov

geboren te Kharkov, Oekraïne
in 1990

Promotor: prof. dr. J.W.M. Frenken

Promotiecomissie:

           prof. dr. D. Bonn (Universiteit van Amsterdam)
           prof. dr. A. Fasolino (Radboud Universiteit, Nijmegen)
           prof. dr. ir. T.H. Oosterkamp
           prof. dr. E.R. Eliel

Cover: Henk-Jan Boluijt

Content

Chapter 1

Introduction

Tribology - the study of friction, wear and lubrication of contacting materials - is a relatively new scientific discipline that has existed for only about 50 years. By contrast, the phenomenon of friction establishes one of the oldest engineering problems with roots dating back many thousands of years: first attempts to sledge on snow (10000 BC), the concept of the wheel (3500 BC), the transportation of massive pyramid stones by the Egyptians (2000 BC), etcetera. It has always remained a challenge to reduce that resistance of motion (friction) when one object rubs against another. Over time people have put much effort in understanding the nature of friction forces [1]. In particular, simple models were set up and phenomenological laws were derived [2], based on observations and measurements of friction forces for dry and lubricated interfaces. This has made it possible to provide a description of the behavior of simple mechanical systems on a practical level and to estimate the frictional energy losses. The experimental efforts got strengthened significantly by progress in microscopy techniques [3], which enabled research of the contacting surfaces down to the atomic scale and shed more light on the more microscopic aspects of the mechanisms of solid-solid interaction and lubrication. In turn, progress in the field of tribology contributes greatly to progress in many modern mechanical systems: wind turbines, brakes, hard-drives, valves, transmissions, wheels and others.

In the era of present-day technology, hand in hand with the development of nano- and microelectromechanical systems (NEMS/MEMS) [4] and other high-tech devices, the demand is increasing for a truly microscopic understanding and control of friction and wear. New, revolutionary approaches are called for at the nano- and microscale. On these small scales, most conventional lubricants (e.g. oil-based) fail to reduce friction for several reasons. Liquids introduce enormous capillary forces, while they bring in the risk of a variety of chemical reactions and they can add to the generation of wear debris [5].

In this PhD Thesis we demonstrate our first steps towards the reduction and control of dry, unlubricated friction on various geometrical scales, with solutions that have the promise to satisfy the boundary conditions set by some of the most pressing modern technological challenges. In Chapter 2 we describe the first stage of an experiment aimed at making the friction-lowering phenomenon of *thermolubricity* [6] active on the macroscopic scale. Our approach is based on earlier studies of friction, conducted in our research group with a Friction Force

Microscope (FFM). In these studies, it was shown that random thermal fluctuations change the familiar, atomic stick-slip motion of the atomically sharp tip of such a microscope into a thermal drifting motion, when these fluctuations are strong enough with respect to the barriers in the energy landscape. These excitations are concentrated in the last nanometers of the tip, because of the extremely small mass and the flexibility of the tip apex. Figure 1.1 shows a calculated dependence of the mean friction force on the true potential corrugation of the contact between the FFM tip and the substrate. The potential corrugation can be varied by adjusting the normal force on the contact [6]. Due to the thermal fluctuations of the tip apex there is a significant increase of the normal force required to see the friction force start increasing (Fig. 1.1).
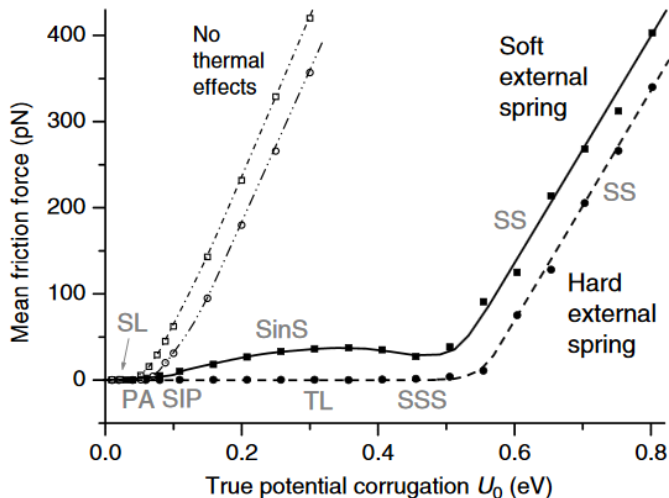
Figure 1.1. Mean friction force as a function of the corrugation of the interaction potential between the substrate and the AFM cantilever [6]. Note that the true potential corrugation is proportional to the actual normal load on the contact. Reprinted with permission from the authors [6].

To achieve similar behavior in a macroscopic contact with an area well beyond that of the very specific tip-surface geometry of an FFM, we have shaped one of the two, macroscopic contacting surfaces in the form of a micro-fabricated array of silicon nanopillars, each with a well-defined spring coefficient, similar to that of a standard FFM tip. This pattern can be regarded as a large multitude of FFM-like tips, each one exhibiting the thermal fluctuations that we identified as

lubricating the single-tip motion in an FFM. We discuss our friction experiments with these fabricated patterns and address the role of the elasticity of the Si nanopillars, the specific choice of the counter-surface, the influence of humidity and that of the normal load. The fabrication process of the Si nanopillar arrays is discussed in detail in Chapter 3 and in ref. [7].

As the second approach to tackle the problem of dry, unlubricated friction at the macroscopic scale, we use a monolayer graphene coating in an attempt to observe the effect of the phenomenon, known as *superlubricity*, on the macroscopic scale. In previous experiments, our group has demonstrated that graphite can bring down friction in nanometer-scale contacts by orders of magnitude [8]. Superlubricity is based on the incommensurability of two contacting crystal lattices that are rotated out of registry. On the nanoscale this can render the friction forces almost negligible. Figure 1.2 demonstrates the average friction force acting at the interface between a graphite nanoflake and an extended graphite surface as a function of the rotational angle between their lattices. Chapter 6 describes our exploration of the potential of superlubricity in a practical context; the grand challenge is to evoke this lattice-mismatch behavior on the macroscopic scale. To this end, we use centimeter-scale, flat surfaces covered with a specially grown, high-quality, single-orientation, single monolayer of graphene. Friction force traces are measured with a novel friction force microscope. First results indicate that graphene indeed has a significant effect on macroscopic friction. In Chapter 6 we also discuss the effect of oxidation of the substrate on friction properties of graphene at the nanoscale.
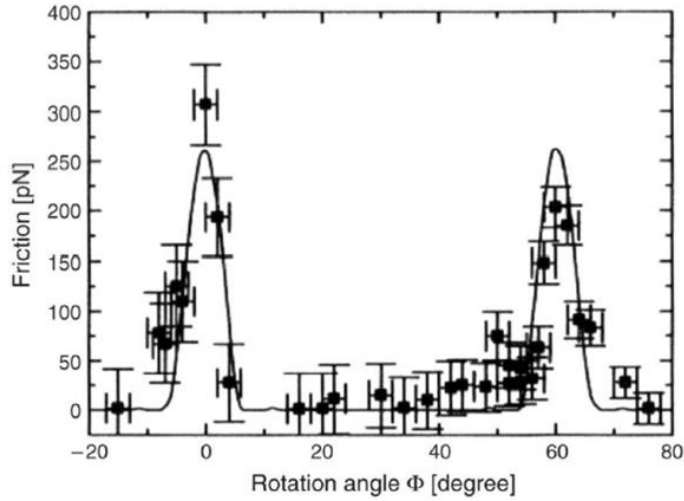
Figure 1.2. Friction force measured versus rotational angle by sensitive friction force microscopy between a nanometer-sized graphite flake and an extended graphite surface [8]. When the two graphite lattices are commensurate, at rotation angles of 0° and 60°, the friction force is high. When the lattices are rotated out of registry by only a few degrees, friction is low. This superlubricity effect has served as the source of inspiration for our experiments on friction between graphene-covered surfaces, described in Chapter 6. Reprinted with permission from the authors [8].

Interestingly, the signature of superlubricity can be associated not only with layered materials, such as graphite, molybdenum disulfide, boron nitride, etcetera [e.g. 9], but also with carbon-based, composite materials, such as Diamond-Like Carbon (DLC) coatings [10]. Even though DLC's form a well-known class of materials that reduce abrasive wear and friction, the origin of their low friction remains poorly understood. In Chapter 4 we report an experiment to explore the lubricating mechanism of DLC coatings. We describe our investigations of the frictional behavior of DLC coatings and draw conclusions about a possible influence of superlubricity in reducing the macroscopic friction of these coatings. For our experiments, we use a novel friction force microscope combined with more conventional surface characterization techniques. By micro-patterning one of the contacting surfaces, we have limited the region where mechanical contact can occur. This has enabled us to follow *all* changes in the contacting surfaces and directly observe the transformation of their structure and composition. In Chapter 5, we present an analysis of the frictional behavior of the micropatterned DLC

5

coatings as a function of relative humidity and sliding velocity, from which we draw conclusions about the lubricating mechanism of DLC and the role of wear particles, generated at the interface during sliding.

Bibliography

1. Gao, J. *et al*. Frictional forces and Amontons' law: from the molecular to the macroscopic scale. *Journal of Physical Chemistry* **108**, pp.3410-3425 (2004)

2. Andersson, S. *et al*. Friction models for sliding dry, boundary and mixed lubricated contacts. *Tribology International* **40**, pp. 580-587 (2007)

3. Croft, W.J. Under the microscope: a brief history of microscopy. Singapore (2006)

4. Bogue, R. Recent developments in MEMS sensors: a review of applications, markets and technologies. *Sensor Review* **33**, pp. 300-304 (2013)

5. Huang, Y. *et al*. MEMS reliability review. *IEEE transactions on device and materials reliability* **12**, pp. 482-493 (2012)

6. Krylov, S.Y. & Frenken, J. Thermal contact delocalization in atomic scale friction: a multitude of friction regimes. *New Journal of Physics* **9**, 398 **(**2007)

7. Antonov, P.V., Zuiddam, M.R. & Frenken, J.W.M. Fabrication of high-aspect ratio silicon nanopillars for tribological experiments. *Journal of Micro/Nanolithography, MEMS and MOEMS* **14**, 044506 (2015)

8. Dienwiebel, M. *et al.* Superlubricity of graphite. *Physical Review Letters* **92**, 126101 **(**2004)

9. Martin, J.M., Donnet, C. & Mogne, Th. Superlubricity of MoS2. *Physical Review B* **48**, 10583 (1993)

10. Erdemir, A. & Donnet, C. Tribology of diamond-like carbon films: recent progress and future prospects, *Journal of Physics D: Applied Physics* **39**, pp. 311-327 (2006)

Chapter 2

Towards thermolubricity on the macroscopic scale

2.1 Introduction

With their invention of the Atomic Force Microscope (AFM), Binning et al. [1] opened a new era in surface science. The AFM enabled them to image surfaces with roughly a thousand times higher resolution than the diffraction limit of an optical microscope, down to the level of 0.1 nm and lower. Since its introduction, the AFM has quickly become a standard laboratory tool with applications in numerous fields, ranging from solid state physics to biology. Shortly after its invention, it was recognized that the AFM can also be used as a so-called Friction Force Microscope (FFM), to perform direct atomic-scale measurements of lateral forces between a sample and a mechanical probe [e.g. 2, 3].

Both the AFM and the FFM provide spatially localized two-dimensional information by scanning the sharp mechanical probe with respect to the surface in very close proximity to each other and monitoring the probe-sample interactions. While most of the AFM applications are based on the data obtained during vertical displacement of the probe, the FFM senses the lateral forces on the substrate that are generated by moving the probe in horizontal plane back and forth, and in this way accesses friction. Figure 2.1 presents the schematics of both microscopes. Structurally, they are very similar. In most cases, the mechanical probe consists of a flexible cantilever beam and a sharp tip. The shape of the cantilever may vary, depending on the application and the anticipated stiffness of the contact. The bending and torsion of the cantilever, caused by the interaction of the tip with the substrate, are measured e.g. with an optical system consisting of a laser emitter and a photodiode. The laser light is focused on the surface of the cantilever. The light that is reflected from the cantilever is being received on the photodiode, which is split in either two halves (AFM) or four quadrants (FFM). The ratios between the light intensities recorded by the sections of the photodiode are transformed directly into electrical signals that indicate the relative position of the reflected laser spot on the photodiode. When the cantilever's normal and torsional spring coefficients K_N and K_τ are known, the corresponding (normal and lateral) interaction forces between the tip and the substrate can be calculated. In this way, a single FFM scan provides a complete map of the interaction forces between the tip and the surface, either two-dimensional (normal plus one lateral direction) or even

three-dimensional (normal plus both lateral directions), depending on the sophistication of the cantilever and the force analysis. The typical spatial resolution of the AFM and FFM is 1 Å. The typical force resolutions can be down to the picoNewton regime. Reviews of recent developments in the AFM and FFM technology and their applications can be found in e.g. [2,4-7].
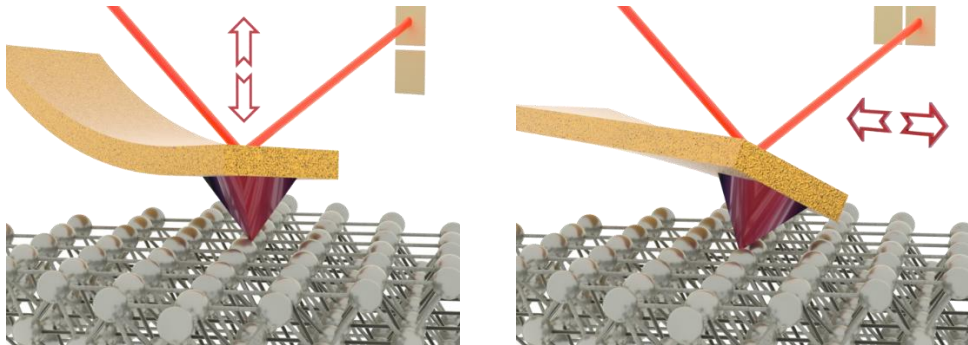
Figure 2.1. Sketches of the principles of the AFM (left) and the FFM (right).

As was mentioned above, the lateral bending of the cantilever beam in the FFM is proportional to the lateral force between the tip and the substrate. Due to its extreme sensitivity, the FFM has contributed greatly to the rapid development of the field of nanotribology: the study of nanoscale friction, adhesion, wear, etcetera [7-11]. The FFM has made it possible to study friction between single-asperity contacts. The fundamental FFM studies have shown that friction laws at the atomic-scale are different from those at macroscopic interfaces [e.g. 11-14]. One of the most important observations by this technique is that the tip during its lateral motion slips over the atomic potential barriers with a saw-tooth-like variation of the lateral force (see, e.g. Fig. 2.2). This effect is known as stick-slip motion.
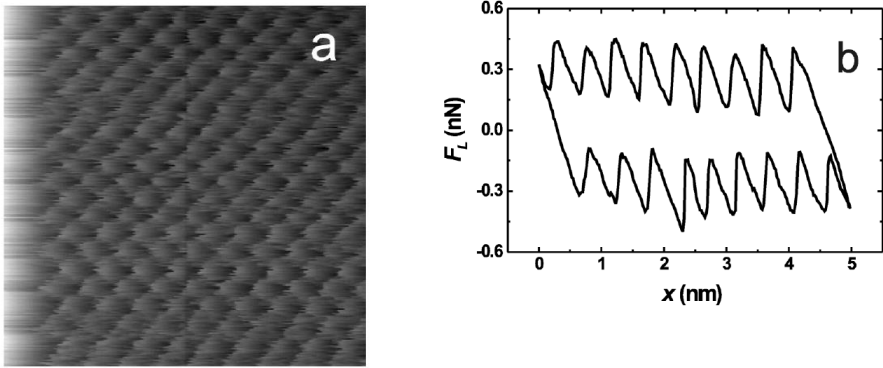
Figure 2.2. (a) Atomic lateral force map of NaCl(100) measured with a silicon tip at $F_N = 0.65\ nN$, and $v = 25\ nm/sec$. (b) Friction loop formed by two scan lines measured along the forward and backward directions. Reprinted with permission from the authors [12].

A simple way to describe the physical interaction between the tip apex and the atomic lattice of the substrate is the Prandtl-Tomlinson model [15, 32]. This quasistatic model assumes that the tip moves in a periodic potential field formed by its interaction with the substrate atomic lattice, while it is being dragged along by an external spring (the cantilever). The sketch in Fig. 2.3 visualizes the model. The cantilever here is described by its spring coefficient K. The interaction of the tip with the atomic lattice is characterized by a periodic potential with a constant amplitude U_0 and a period equal to that of the substrate lattice constant a. The spring support and substrate are moving with respect to each other at a low, constant velocity v. Once the lateral force exerted on the cantilever by the displaced substrate is high enough to drag the tip apex over the atomic barrier, the tip-cantilever combination slips to the next potential-energy well. In this model, the excess energy is removed 'instantaneously', after which the tip sticks in its new well of residence until the substrate has moved sufficiently again to make it slip further. Following this simple mechanistic model, the motion of the tip over the lattice reproduces the symmetry of their joint potential-energy map.
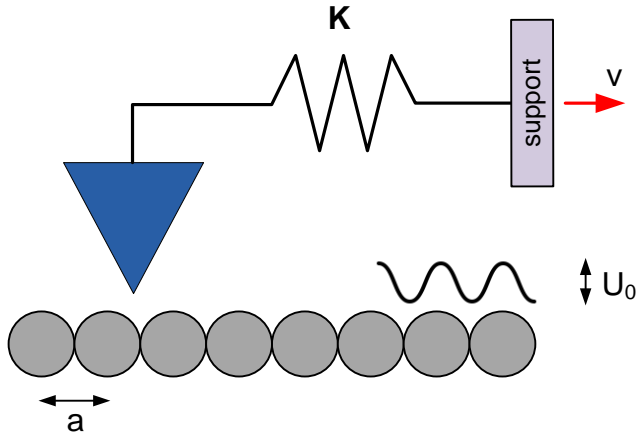
Figure 2.3. Prandtl-Tomlinson model applied to friction-force microscopy [15].

The traditional Prandtl-Tomlinson model is used commonly to describe friction phenomena for many interfaces, typically at low speeds and at wide ranges of normal loads and vacuum or atmospheric conditions. This model clearly oversimplifies even the most basic friction process on the single-asperity scale. Indeed, if we consider the FFM as the simplest practical example, we should realize that there is always a second spring hidden in the system. This is the tip itself, which is so narrow near its apex that its spring coefficient for lateral deformations is even lower than that of most cantilevers used in AFM and FFM experiments [e.g. 2, 12, 21, 22]. Due to the extremely low mass of this tip apex, its lateral eigenfrequency should nevertheless be extremely high. By all means, the tip apex should be considered as a separate mechanical element in the description of FFM experiments and therefore as a component that should be added to come to a more appropriate description than the Prandtl-Tomlinson model.

Recently, Krylov *et al.* [16-18] have analyzed basic tribological experiments [16, 19-23] to motivate the importance of the tip apex flexibility and of the thermally activated character of its lateral motion. The model adopted by Krylov *et al.* is based on a two-mass-two-spring description of the cantilever system (see Fig. 2.4), where the second spring and the second mass are associated with the tip apex. In this description, the tip apex flexibility is represented by a spring coefficient *k*,

11

which is typically in the order of 1 N/m, similar to the stiffness of a single atomic bond. The tip apex mass m is estimated to be $m_{eff} \leq 10^5 m_{at}$. This combination of spring coefficient and mass corresponds to a high effective lateral vibration frequency of the tip apex of at least several GHz [16, 23]. Therefore, even when the potential barriers are much higher than the thermal energy $k_B T$, the tip explores the potential energy landscape with such a high attempt frequency that it can spontaneously overcome these barriers and 'jump' between neighboring potential wells. As a result, the lateral force between the tip apex and the substrate can vanish (almost) completely. This thermally induced slipperiness is referred to as *thermolubricity* [23].
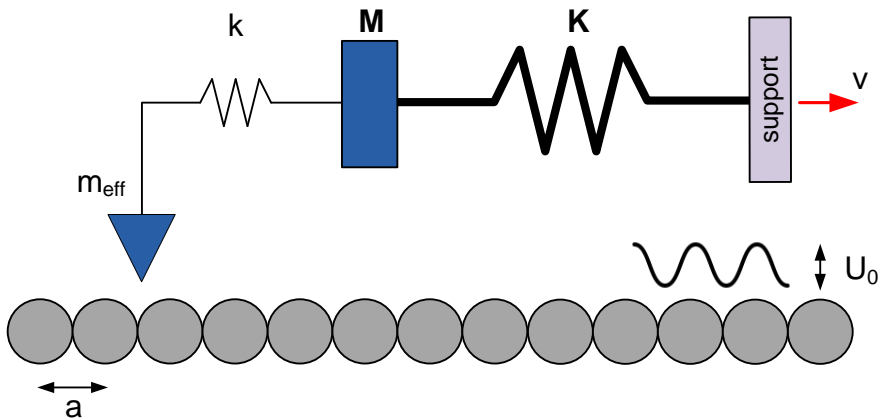

Figure 2.4. Two-mass-two-spring model of the cantilever and the tip apex: m_{eff}, k and M, K are the parameters of the tip and the cantilever, respectively; the cantilever support and the substrate are moving with respect to each other with velocity v.

2.2 Design of nanopillar array

So far, the lubricating role played by temperature has been considered and observed only at the nanoscale, associated with the FFM tip. Here, we pose the logical next question: can the effect of *thermolubricity* be extended to the larger scale of technologically relevant, macroscopic systems? Probably the easiest approach that one could imagine, would be to simply scale up the complete geometry of the FFM tip. Unfortunately, this approach is doomed to fail. While its geometrical size gets larger, the mass of the tip apex increases proportionally to the third power of the linear size, while the spring coefficient of the tip apex scales proportionally to d^4/L^3, where d is the diameter and L is the length of the tip (see below), which is proportional to the linear size. The eigenfrequency therefore reduces inversely proportionally with the linear size, while the root-mean-square displacement of the thermal motion reduces inversely proportionally with the square root of the linear size. Both reductions strongly reduce the rate at which the larger system can overcome the same energy barriers, whereas the lateral energy barriers for a larger contact (under a higher load) should certainly be expected to be higher. Thus due to inconsistency of these parameters one should choose for another solution. To save low mass and required eigenfrequency of the frictional contact, we decided to extend a number of FFM-like tips which simultaneously can be brought into direct contact with the surface. One of the ways to do it is to shape one of the two contacting surfaces in the form of a vast array of nanopillars (NP). The mechanical properties of each NP should match to the ones of the FFM tip apex, in terms of typical eigenfrequency, mass and hence vibrational amplitude. This assumes that each NP wills mimic lubrication properties of the tip, due to its similar thermal activation. We utilize their mechanical properties in an attempt to influence the friction between dry, unlubricated surfaces. We expect friction to be affected significantly by the simultaneous, spontaneous motion of the NPs. We choose the dimensions of the NPs such that they exhibit transverse vibrations similar to the typical FFM tip apex. Two aspects are of specific importance, here, namely the extremely high natural frequency of the FFM tip apex, of $f_0 \geq 0.1\ GHz$, and the thermal vibration amplitude at room temperature $(T = 300\ K)$, typically in the order of an interatomic distance, $\sqrt{<x^2>}$ ~0.1 nm. Though, due to restrictions in size of the NPs and available cleanroom tools (see below), we have also to accept

the NPs with lower values of the vibrational amplitude ($\sqrt{<x^2>}\sim 50\ pm \div$ 0.1 nm). When these conditions are met, we foresee that when the NPs are brought into mechanical contact with a flat counter-surface, each NP will conduct an independent, diffusive random walk over the counter-surface. This should reduce the lateral force, required to translate the entire NP array over the counter-surface to nearly zero at low sliding velocities.
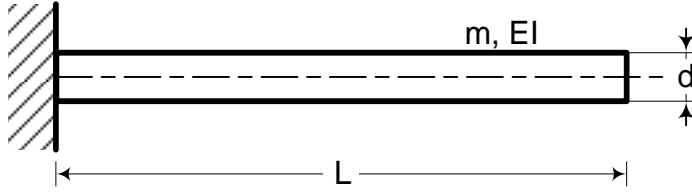
Figure 2.5. A cylindrical cantilever beam fixed at one end as a model of the mechanical properties of a single NP.

We treat the NPs as nanoscale cylinders. This relatively trivial geometrical shape allows us to easily change the necessary parameters of individual contacts: their natural frequency, stiffness and vibrational amplitude. We define the NP geometry (Fig. 2.5) by two variables – the diameter of the pillar d and its length L. According to simple thermodynamics [9], we associate an average thermal energy of $\frac{1}{2}k_B T$ with the one-dimensional lateral motion of each NP. When we relate this to the NP's root-mean-square vibrational excursion, we obtain

$$\frac{1}{2}k\langle x^2\rangle = \frac{1}{2}k_B T \ , \tag{2.1}$$

where k is the effective lateral spring coefficient of the pillar. Mechanically, each NP can be described as a cylindrical cantilever beam fixed at one end. Therefore, its spring coefficient k can be written as

$$k = \frac{3EI}{L^3} \ , \tag{2.2}$$

where E is the Young's modulus of the beam material and I is the area moment of inertia of the beam, which is given by

$$I = \frac{\pi}{64} d^4 \ . \tag{2.3}$$

Combining these relations, we obtain

$$\frac{d^4}{L^3} = \frac{64 k_B T}{3\pi E <x^2>} , \tag{2.4}$$

with the requirement that $\sqrt{<x^2>}$ represents the thermal vibration amplitude of the NP, in the order of a fraction of an angstrom to 1 Å. Our second condition on the NP dimensions comes from the required, high lateral vibration frequency. The natural frequencies of the NP are given by

$$f_n = \frac{a_n^2}{2\pi} \sqrt{\frac{EI}{mL^4}} \ . \tag{2.5}$$

The number $n = 1,2,3, \ldots \infty$ indicates the vibrational mode and the first three modes have $a_n = 1.875, 4.694, 7.885$, respectively. The mass per unit length m of the beam is given by

$$m = \frac{\pi}{4} d^2 \rho \ . \tag{2.6}$$

where ρ is the mass density of the beam.

For a given value of the fundamental frequency f_1 we obtain the following condition for the NP dimensions.

$$\frac{d^2}{L^4} = \frac{64\pi^2 \rho f_1^2}{a_1^4 E} \ . \tag{2.7}$$

Combining the two equations for the NP shape, we find

$$L = \left(\frac{a_1^8 k_B T E}{192\pi^3 \rho^2 f_1^4 <x^2>} \right)^{1/5} \text{ and} \tag{2.8}$$

$$d = \left(\frac{64 \, a_1^{12} k_B^4 T^4}{81 \, \pi^2 \rho^3 E f_1^6 <x^2>^4} \right)^{1/10} . \tag{2.9}$$

For example, for $\sqrt{<x^2>} = 0.14 \, nm$ and $f_1 = 1 \, GHz$, we obtain NP dimensions of $d = 10 \, nm$ and $L = 100 \, nm$. As the requirements for the amplitude and frequency of the NP vibrations are no more than approximate, we have a relative 'freedom' in our choices for d and L. Table 2.1 represents a comparison of these parameters for different settings of nanopillar sizes. The inked cells point at those combinations which satisfy the requirements for the amplitude and frequency. Though pillars with diameter less than $50 \, nm$ are a big challenge to manufacture by means of conventional cleanroom tools. Such combinations are marked with red. However, green color suggests an order of sizes which can be fabricated and are close to the vibrational requirements at the same time. In Table 2.2 we show the corresponding value of the lateral spring coefficient for the nanopillar settings from Table 2.1.

$\dfrac{f_1, Hz}{\sqrt{<x^2>}, m}$	L					
	10 nm	50 nm	100 nm	500 nm	1 µm	10 µm
2 nm	21 GHz 0.1 nm	0.84 GHz 1.3 nm	0.21 GHz 3.6 nm	8.4 MHz 40 nm	2.1 MHz 0.1 µm	21 kHz 3.6 µm
10 nm	0.1 THz 4.5 pm	4.2 GHz 51 pm	1 GHz 0.14 nm	42 MHz 1.6 nm	10.5 MHz 4.5 nm	0.1 MHz 0.14 µm
50 nm	0.5 THz 0.18 pm	21 GHz 2 pm	5.2 GHz 5.8 pm	0.21 GHz 64 pm	52 MHz 0.18 nm	0.52 MHz 5.7 nm
100 nm	1 THz 45 fm	42 GHz 0.5 pm	10.5 GHz 1.4 pm	0.42 GHz 16 pm	0.1 GHz 45 pm	1 MHz 1.4 nm
500 nm	5.2 THz 1.8 fm	0.21 THz 20 fm	52 GHz 58 fm	2.1 GHz 0.65 pm	0.52 GHz 1.8 pm	5.2 MHz 58 pm
1 µm	10 THz 0.45 fm	0.42 THz 5 fm	0.1 THz 14 fm	4.2 GHz 0.16 pm	1 GHz 0.45 pm	10 MHz 14 pm

Table 2.1. Natural frequency and vibrational amplitude of nanopillar as a function of its diameter (D) and length (L), varying in the range of $2\ nm \div 1\ \mu m$ and $10\ nm \div 10\ \mu m$, correspondently. All inked cells indicate the pillar configuration with acceptable order of the natural frequency and vibrational amplitude. However, red color corresponds to pillar dimensions which are difficult to fabricate. Green color points at the order of the nanopillar size which can be reproduced with conventional cleanroom techniques.

$k, N/m$		L					
		10 nm	50 nm	100 nm	500 nm	1 µm	10 µm
D	2 nm	3E-01	3E-03	3E-04	3E-06	3E-07	3E-10
	10 nm	2E+02	2E+00	2E-01	2E-03	2E-04	2E-07
	50 nm	1E+05	1E+03	1E+02	1E+00	1E-01	1E-04
	100 nm	2E+06	2E+04	2E+03	2E+01	2E+00	2E-03
	1 µm	2E+10	2E+08	2E+07	2E+05	2E+04	2E+01

Table 2.2. Lateral spring coefficient of nanopillar as a function of its diameter (D) and length (L), varying in the range of $2\,nm \div 1\,\mu m$ and $10\,nm \div 10\,\mu m$, correspondingly. The cells colored in green correspond, similar to Table 1, to nanopillars which satisfy the requirements of the vibrational amplitude, the natural frequency and can be manufactured by means of conventional cleanroom techniques.

There are several combinations of the NP dimensions, which were used by us for the tribological experiments. They combine a sufficiently large vibration amplitude at room temperature with a sufficiently high frequency:

- $d = 70\,nm, L = 800\,nm$: leads to $f_1 = 0.15\,GHz$, $\sqrt{<x^2>} = 70\,pm$, and $k = 0,93\,N/m$
- $d = 100\,nm, L = 1000\,nm$: leads to $f_1 = 0.1\,GHz$, $\sqrt{<x^2>} = 45\,pm$ and $k = 2\,N/m$.

NPs of these dimensions are convenient for nanofabrication with conventional cleanroom techniques. The detailed nanofabrication process of the NP arrays is discussed in the following chapter and in ref. [25]. It was decided to manufacture a number of NP arrays, each with a different NP stiffness k, in order to test the influence of this parameter on the friction coefficient. Another critical parameter in the design of the pillar array is the pitch, i.e. the distance between neighboring NPs. By changing this parameter, one can adjust the normal force per pillar, which, depending on the chosen counter-surface, should not exceed a few nN. The particular range of the normal force is chosen in analogy with the AFM experiments [e.g. 21-23], where sufficiently low potential corrugation, proportional to the normal load between the tip and the substrate, was a significant factor

allowing thermally activated excursions of the tip apex between the atomic potential wells.

2.3 Experimental setup

Our friction experiments on the NP arrays were conducted by means of a Bruker Scanning Probe Microscope 'Multimode 8'. The samples were mounted into the microscope on Al pucks with a diameter of $1\ cm$ by means of a special adhesive tape. The microscope was installed in an isolated chamber made of Plexiglas to control the relative humidity (RH). The RH was varied by means of flushing the chamber with a vapor of liquid nitrogen and could reach a lower value of 0.7%. In all experiments the temperature was kept at $\sim22 \pm 2°C$.

2.4 Experimental results and discussion

As the first fabricated pillar patterns were relatively small, just $50 \times 50\ \mu m^2$, an AFM or, rather, an FFM was the only standard tool that we could use to conduct local friction tests. In a traditional FFM experiment one measures the lateral forces on the sharp tip at the end of a cantilever, while the tip is dragged over an extended substrate. In the particular case of the NP arrays, the geometry is reversed. With many FFM-tip-like NPs acting as the 'substrate', one should measure the lateral force between the NP array and an 'extended probe. In order to avoid local damage to the NP array, we aimed for making mechanical contact simultaneously between the probe and as many NPs as possible. For this purpose, obviously, a traditional FFM cantilever with a pyramidal tip would not be suitable, due to its extremely small contact area. Instead, we used a spherical probe (Fig. 2.6). This particular probe consists of a polymethyl methacrylate (PMMA) sphere glued on the tip location on a standard AFM cantilever. The idea here is that the part of the sphere that is the first to come into contact with the NPs first will automatically be parallel to the plane of the NP apices, while for a sufficiently large diameter, the curvature of the sphere will be low enough that its contact force will always be distributed over a large number of NPs. In the example of Fig. 6, the sphere has a diameter of $7\ \mu m$, which is 35 times the pitch of the typical NP patterns of $200\ nm$.
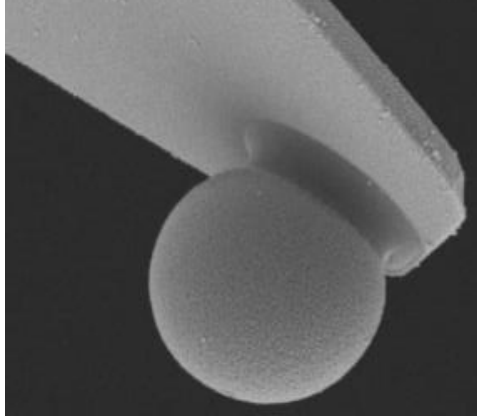
Figure 2.6. An AFM/FFM cantilever with a 7 μm diameter PPMA sphere glued near the end. SEM image adopted from the [35].

The normal (bending) spring coefficient k_N of our beam-shaped Si cantilevers was measured directly using the Thermal Noise Method [33]. According to the equipartition theorem, the thermal energy of the cantilever can be expressed as

$$\tfrac{1}{2}k_N\langle x_N^2\rangle = \tfrac{1}{2}k_B T \; ,$$
(2.10)

where $\langle x_N^2\rangle$ is the mean square deflection of the cantilever, which vibrates due to thermal noise; k_B is the Boltzmann constant and T is the temperature. By measuring the power spectrum of the thermal fluctuations, one can find

$$k_N = \frac{k_B T}{p},$$
(2.11)

where p is the area of the power spectrum and equals to $\langle x_N^2\rangle$.

For the particular cantilevers the typical values of the normal spring coefficient varied in the range of $k_N = 0.3 \pm 0.1 \; N/m$. The lateral (torsional) spring coefficient K_L of the cantilever was estimated theoretically with elasticity theory, based on the dimensions of the beam and the geometry of the colloidal sphere attached to it. The dimensions of the cantilever were measured with scanning

electron microscopy to be a length L of $450 \pm 3\ \mu m$, a width w of $20 \pm 1\ \mu m$, a thickness t of $2 \pm 0.1\ \mu m$ and a height of tip h of $7 \pm 0.1\ \mu m$. Therefore, the lateral spring constant k_L of was calculated based on geometry of the cantilever [34]:

$$k_L = \frac{Gwt^3}{3h^2 L} \tag{2.12}$$

where G is the shear modulus ($G = E/2(1 + v)$, E is the Young's modulus and v is the Poisson's ratio). Typical values of k_L for the used cantilevers are in the range of $110 \pm 10\ N/m$. The error margin given here for the lateral spring coefficient reflects the uncertainties in the measured dimensions, but does not include possible systematic shortcomings in the simple, mechanical description of the torsional stiffness of the cantilever-sphere combination. Lateral and normal force calibration procedure was conducted according to [33, 34]. Normal force was determined based on measured voltage response of the photo-diode V_N during normal bending of the cantilever in contact with the substrate. Force-distance curves were recorded in order to determine the normal sensitivity S_N. The resulting force value can be calculated as follows:

$$F_N = k_N S_N V_N \,. \tag{2.13}$$

In the calculations, we took the total value of the normal force, which besides the mechanical force applied with the cantilever, takes into account the adhesive interaction between the ball-tip and the pillars. Thus, $F_N = F_{mech} + F_{adh}$ (Fig. 2.10).

To calculate the actual value of the lateral force, we used a relation between the lateral S_L and normal sensitivity S_N. According to [34] the following holds:

$$F_L = k_L S_N V_N = \frac{3}{2} k_L \frac{h}{L} S_N V_L \,, \tag{2.14}$$

where V_L is the relative change in voltage signal from the photo-diode due to lateral bending of the cantilever.

In order to stay close to the conditions at which thermolubricity has been recognized in FFM experiments, we need to apply low normal forces on each NP,

in the order of 1 nN or lower. At such a low normal force, the Hertzian contact area between the NP and the PMMA sphere will be small and also the maximum lateral force that can build up on each contacted NP will remain low (below 1 nN). Even for the low lateral spring coefficient of the NPs, in the order of 1 N/m, this level of forces should be expected to lead to no more than a modest bending of the NPs, in the order of 1 nm or less. Nevertheless, this flexibility is sufficient to enable the PMMA sphere to establish simultaneous contact with an ensemble of NPs. An artist impression of this situation is given in Fig. 2.7. The surface roughness of PMMA [e.g. 26], in the order of $10 \div 25\ nm$, and the formation of capillary water bridges in ambient atmosphere between the contacting asperities provide extra reasons for the sphere to engage into contact with multiple, neighboring NPs. During sliding, the ensemble will be 'refreshed' all the time, with new NPs coming into contact with the sphere and others going out of contact. Due to the flexibility of the NPs, the sliding should be expected to be accompanied by hysteresis, both in the selection of NPs that the sphere is in contact with and in the average bending direction of these NPs. These effects should depend on the total normal load and on the degree to which the contact with the NP ensemble is slippery due to thermolubricity or other forms of lubrication.
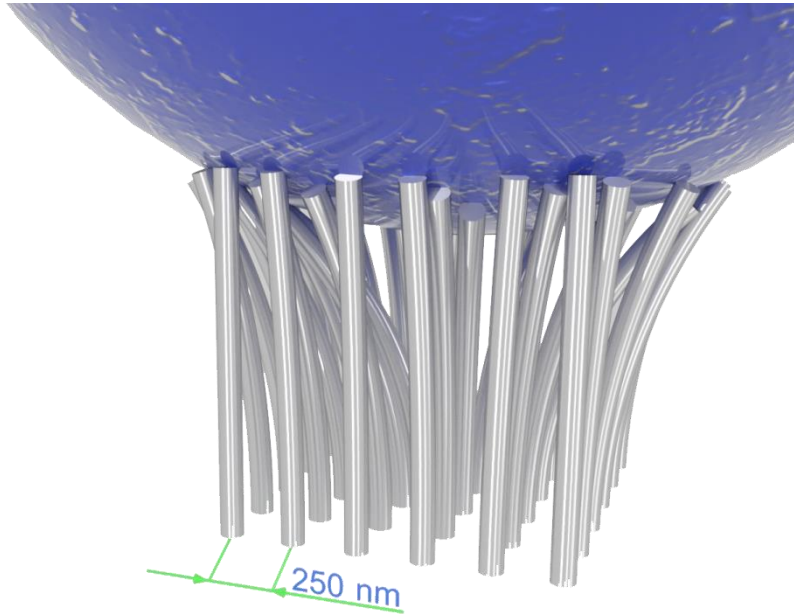
Figure 2.7. Artist impression of the simultaneous contact of a spherical tip with multiple NPs under normal load.

In preparations for the tests, we found that adhesion between the pillars may lead to their lateral bending. Their flexibility is an essential factor in concern of their mechanical contact with colloidal AFM probe. A direct illustration of this flexibility is provided by the SEM images of Fig. 2.8. They were taken quickly after a 1:24 aspect-ratio NP array had been immersed in water. Due to the capillary bridges formed by residues of water between some of the neighboring NPs, some pairs of NPs become bent, after removal of the NP array from the water. Fig. 2.8 demonstrates that this effect is even visible in the (modest) vacuum of the SEM. The bending is extreme, with the NPs touching each other over the full NP-to-NP distance of $200\ nm$, for the particular design. This corresponds to a bending of $100\ nm$ per pillar. Taking into account the spring coefficient of the specific pillars of $k = 3,6\ N/m$, it indicates that a capillary attraction between the pillars is at least $360\ nN$.
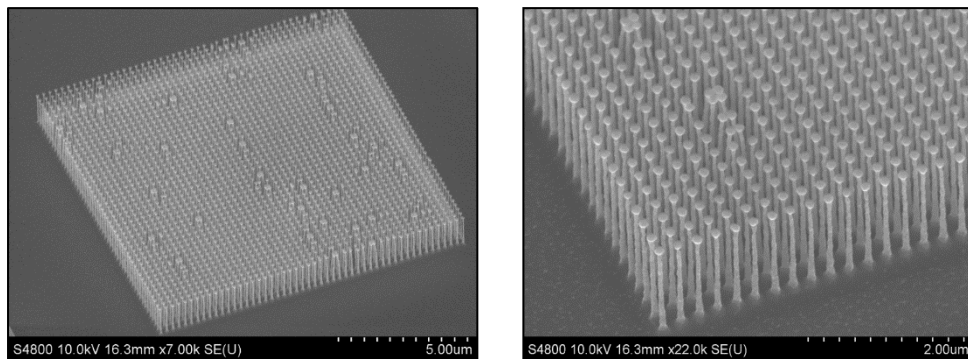
Figure 2.8. SEM micrographs, overview and detail, of the 1:24 aspect ratio NP array, recorded within approximately 10 min after being removed from immersion in water.

The NPs, even after removing of the resist residues, were found to be adhesive to the PMMA colloidal probe too. Force-distance curves [29] measured between the PMMA sphere and the NP array at two different RH levels are presented in Fig. 2.9. Indeed, we see that under ambient conditions the adhesion is measured to be up to five times higher than in a relatively dry environment.
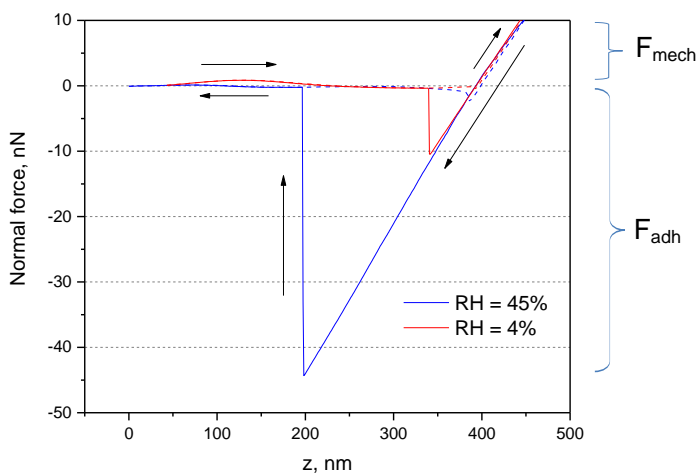
Figure 2.9. Force-distance curves measured between the PMMA sphere and the Si NP arrays after removing of resist at relative humidities of 4% (red curve) and 45% (blue curve). Solid and dashed parts of the curves correspond to approach and retraction of the tip, respectively. The total normal force is calculated as $F_N = F_{mech} + F_{adh}$.

We have explored the mechanical behavior of the contact between the PMMA sphere and a Si NP array in a series of FFM experiments at various normal loads. Figures 2.10 and 2.11 show height and lateral force maps at normal loads of 30 and 50 nN, respectively. The measurements are done on the $5x5\ \mu m^2$ area of the NPs with $100\ \mu m$ diameter and $1000\ \mu m$ height, while the pitch is $250\ nm$. The scan direction in the images is from left to right. In both measurements the minimum lateral force (dark color) is recorded every time when the sphere is located in the highest vertical positions, i.e. on top of one of the pillars (bright color). The 2D height profiles, plotted in Figs. 2.10b and 2.11b, show that along each scan line the vertical position of the sphere is modulated with a variation in the order of $10\ nm$, the precise amplitude and the shape of the trajectory depending on the applied normal force. As was mentioned above, essential for the large vertical motion of the sphere is the lateral flexibility of the NPs. Besides the normal load another major force influencing this vertical amplitude, is supposed to be adhesion. This might occur mostly due to formation of capillary bridges [e.g. 27-28] between the apices of the NPs and the sphere. This particular interface is extremely sensitive to the RH level, because both contacting surfaces are hydrophilic. Therefore the adhesion force between them can become significant, even at relatively modest RH values.

At a normal load of $30\ nN$ the sphere moves up and down over almost $14\ nm$, as shown in Fig. 2.10 (a, b). Naïvely, we had expected the sphere to be in contact only with the apices of at most four NPs at any point in time and the resulting amplitude of its vertical motion to be below $1\ nm$. What the experiment strongly suggests is that the sphere travels between locations at which it is directly above a single (straight) NP and locations in between NPs, where it sinks into the NP array by virtue of the sideways flexibility of the NPs. This is the situation illustrated in the artist impression of Fig. 2.7. The humidity, in this case $RH = 45\%$, may have contributed to this effect, because the variation in the number of NPs that the sphere is in contact with should be accompanied by a significant variation in the adhesive force in the order of $1000\ nN$ [36] with which the sphere is pulled towards the NP array, due to the capillary bridges between the sphere and the NPs that it is in contact with. In the top positions the number of (capillary) sphere-NP contacts can be as small as one, whereas in the lower positions, it can be in the order of thirty. Our interpretation of the height signals in Figs. 2.10 (a, b) is

supported by the lateral force measurements in Figs. 2.10 (c, d). The darker colors in Fig. 2.10c indicate lower lateral forces. The minimal lateral forces are observed for positions on top of individual NPs (Fig. 2.10a), where the sphere experiences a relatively small contact area and, correspondingly, the minimal capillary adhesion. Nevertheless, even at these positions the tip seems to be able to interact with the neighboring bended pillars, which explains a presence of local maxima of the lateral force at the corresponding to positions on top of NP (Fig. 2.10c). The average values of force minima in this situation correspond to $F_L = 1.5 \pm 1\,nN$. By contrast, at positions between the NPs, the lateral force rapidly increases to $F_L = 9 \pm 2\,nN$ at the half-pitch position.

It is important to realize that the observed minima in the lateral force should not be associated with an effect of thermolubricity of the NP array. In fact, we have to assume that the capillary necks between the sphere and the NPs severely damp the thermally activated lateral vibrations of the NPs that would be essential for thermolubricity. A possible solution to this issue is discussed later in this chapter.
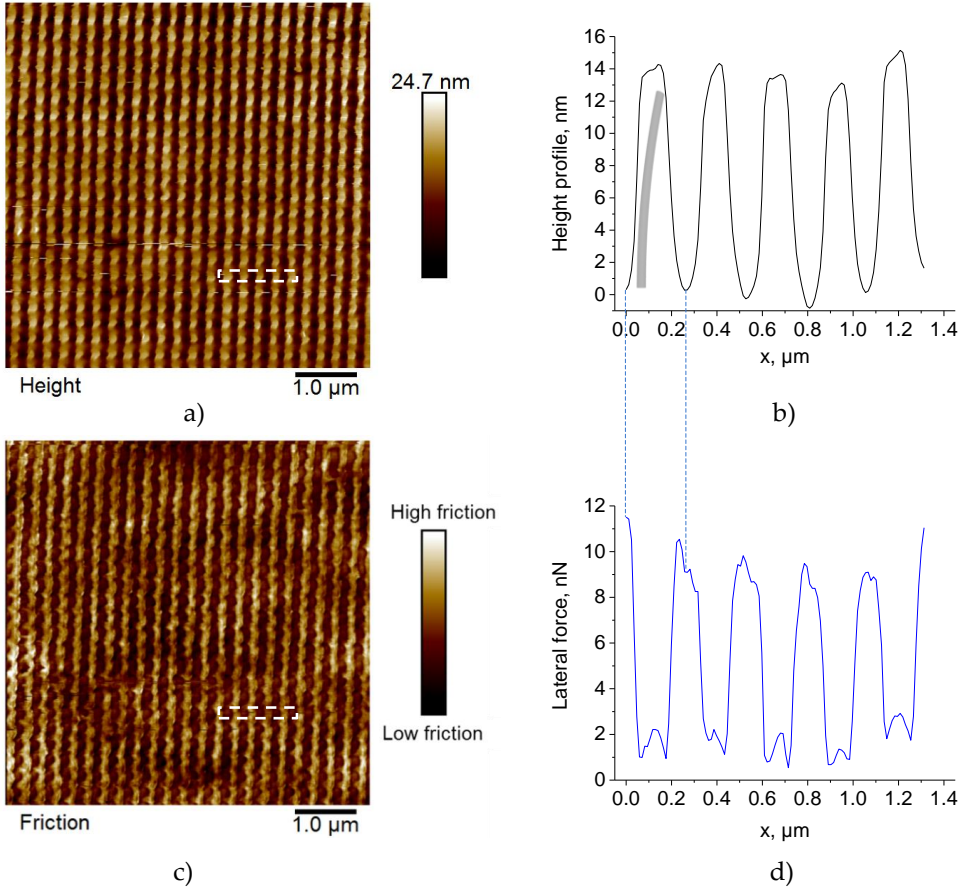
Figure 2.10. FFM measurements for a 7 μm diameter PMMA sphere sliding over a Si NP array, for a pillar height of 1 μm, a pillar diameter of 100 nm (aspect ratio of 1:10) and a pitch of 250 nm. Displayed are the simultaneously measured height (a,b) and lateral force (c,d) for the sphere sliding from left to right. Total normal load 30 nN, $F_N = F_{mech} + F_{adh} = 5\,nN + 25\,nN$. RH = 45%. The local height and friction profiles b and d are plotted along the center of the nanopillars within the regions marked with a white dotted line. Schematics of the nanopillar in (b) is not on the actual scale and is meant to assist in comparison of the height and lateral signal.

At the higher load of 50 nN (Fig. 2.11), the signature of the elastic bending of the NPs becomes even stronger. The signature of the pillars in the height map (Fig. 2.11a) is more distorted, than at $30\,nN$. Between the NP rows, height variations become visible that we associate with trajectories of the sphere between rows of bent pillars. In contrast to the height profile measured at $30\,nN$, the height variations at $50\,nN$ load (Fig. 2.11b) are smaller, with the maximum amplitude,

measured for trajectories with the sphere centered on the NP rows, remaining limited to $8\,nm$. In Fig. 2.12 we compare typical height trajectories of the sphere locally measured on the NPs at normal loads of $30\,nN$ and $50\,nN$. We think that the higher load is sufficient to let the sphere first bend a NP forward and to overcome it without the NP stretching out during the passage. This implies that the sphere performs a stick-slip type of motion with respect to that NP. This is supported by the asymmetric height profiles, with a tilted shoulder on the ascending (left) part of each NP (Fig. 2.11b). Another consequence of the hysteretic type of motion is that the measured diameter of the NPs appears larger ($\sim 150\,nm$) at the higher loading force, than the actual NP diameter ($100\,nm$) that can be recognized at the lower load.
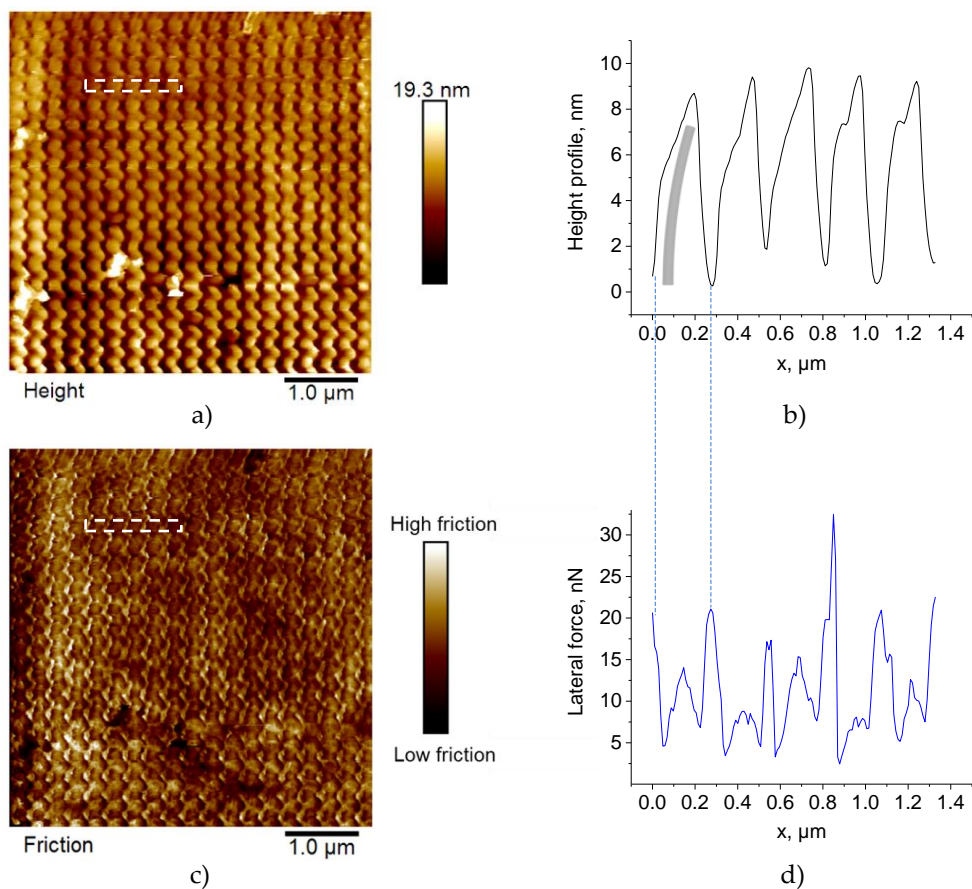
Figure 2.11. FFM measurement of the NPs with an aspect ratio of 1:10. A comparison between a height (a,b) and a lateral force channels (c,d) in trace direction. Total normal load $50\,nN$ ($F_N = F_{mech} + F_{adh} = 22\,nN + 28\,nN$). $RH = 45\%$. The local height and friction profiles b and d are plotted along the center of the nanopillars within the areas marked with a white dash line. Schematics of the nanopillar in (b) is not on the actual scale and is meant to assist in comparison of the height and lateral signal.
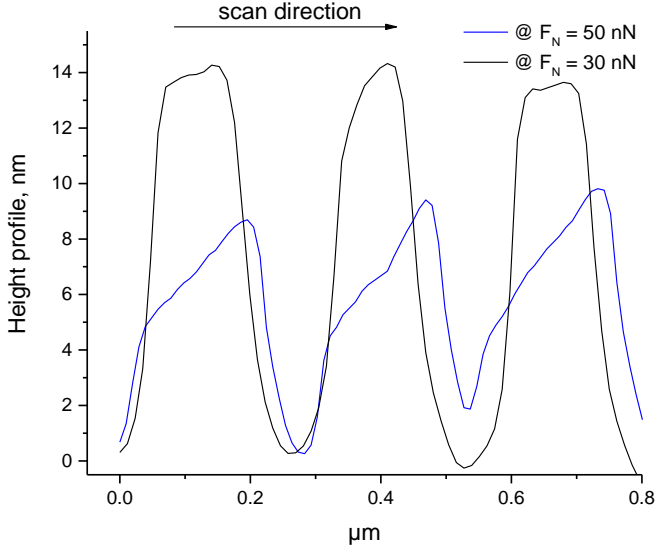
Figure 2.12. Comparison between the height profiles of Figs. 2.11 and 2.12, scanned from left to right with a the ball-shaped FFM tip over a NP array (diameter-to-height aspect ratio of 1:10) at two different normal loads. RH = 45%.

Also the lateral force pattern (Fig. 2.11c) has features that are caused by the lateral deformation of the NPs when the sphere is dragged over the NP rows. During each 'climbing' event, the lateral force between the sphere and the NPs gradually increases (Fig. 2.11d), caused primarily by the bending of the NP directly in front of the sphere. At the normal load of $F_N = 50 \, nN$, this leads to a new, local peak in the lateral force of approximately $F_L \approx 10.5 \, nN$. Before the sphere reaches the highest point, on top of the NP, the lateral force decreases again. The lower values of the lateral force, measured both before and after the on-top position, are $F_L = 5 \pm 2 \, nN$. Again, the global force maxima correspond to configurations with the sphere midway between the on-top positions, where it sinks in maximally between the bending NPs and makes simultaneous contact with the largest number of NPs. On re-inspection of the data at lower load (Fig. 2.10), we recognize that a local maximum in the lateral force was also present in those data, for the on-top positions of the spherical tip, albeit much more modest than at the higher load.

Following the discussion of the effect of RH on frictional behavior of the NPs, we conducted a test at dry conditions ($RH = 4\%$) and a normal load of

30

12 nN. The test was conducted on a NP array of $10\,x10\,\mu m^2$, with NPs of $70\,nm$ diameter, $800\,nm$ height (aspect ratio 7:80) and arranged with a $250\,nm$ pitch. As was mentioned above, the adhesion part of the force-distance curve (Fig. 2.9) is decreased by almost a factor five 5 at the lower humidity, compared to adhesion in the ambient humidity of RH 45%. Fig. 2.13 shows height and lateral force data obtained at dry conditions. We expect that the number of capillary bridges acting at every point in time between the tip and the NPs should be lower, causing less adhesive interaction. Thus, the tip height variations presumably should be decreased too. Indeed, due to lower normal force and adhesion, the maximum height difference in this case equals $6\,nm$ (Fig. 2.13b), which is indeed below the height variations in Figs. 2.10 and 2.11. Nevertheless, the qualitative lateral force response remains the same: directly on top of a pillar the sphere experiences the lowest lateral force of $F_L = 0.8 \pm 0.5\,nN$, which significantly increases to $F_L \approx 4.0 \pm 1.5\,nN$, during its passage to the next pillar. Even though these lateral forces are much lower than those in Figs. 2.10 and 2.11, the corresponding coefficients of friction remain nearly unchanged, varying between a lower value in the order of 0.07 and a higher value of 0.33.
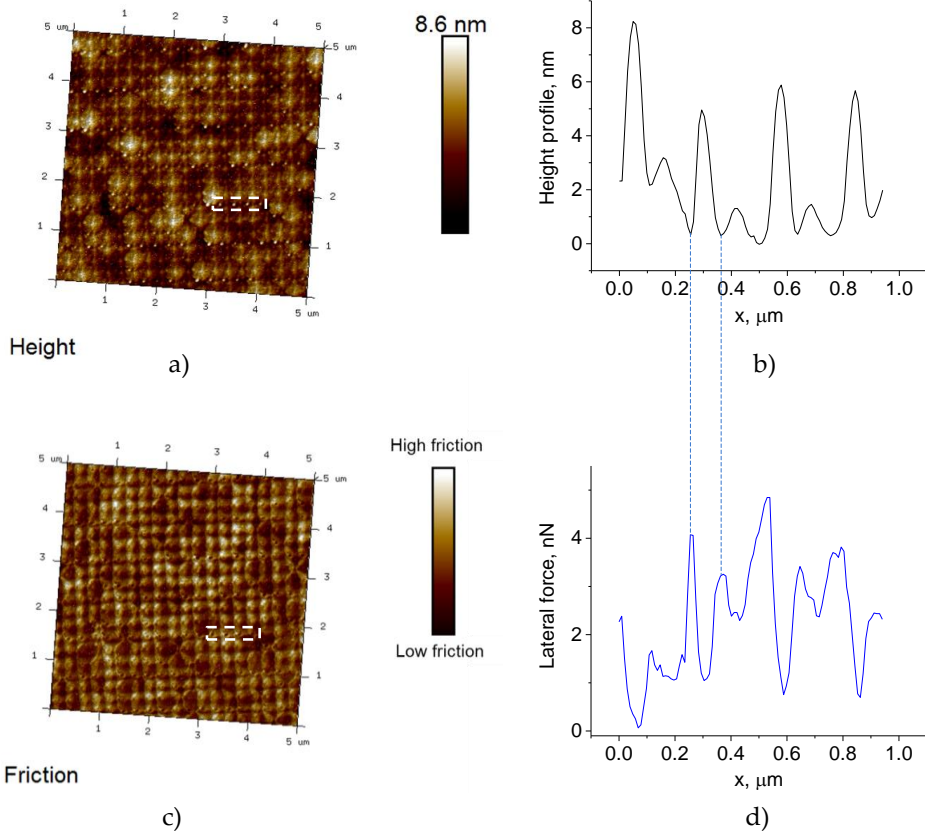
Figure 2.13. FFM measurement of the NPs with an aspect ratio of 7:80. A comparison between height (a, b) and lateral force channels (c, d) in trace direction. Normal load $12\,nN$ ($F_N = F_{mech} + F_{adh} = 4\,nN + 8\,nN$). $RH = 4\%$. The local height and friction profiles b and d are plotted along the center of the nanopillars within the areas marked with a white dash line. Schematics of nanopillar in (b) is not on the actual scale and is meant to assist in comparison of the height and lateral signal.

To summarize the observations, opposite to our original expectations, the chosen PMMA ball-shape tip cannot provide contact with a sufficiently large number of NPs simultaneously. On the other hand, its spherical shape allowed us to conduct the first validation measurements on the fabricated patterns without having to deal with the problem of alignment of the slider with respect to the NP substrate structure. The observation that for all investigated values of the normal load and the relative humidity, the trajectory of the spherical tip exhibits height

variations, suggests that the sphere is in more intimate contact with the NPs than originally anticipated. As a consequence, it might severely damp the thermal vibrations of the NPs that it touches. The essence of this problem resides in the geometry of the sphere, which combines simultaneous contacts between NPs and the surface of the sphere that range from strongly attractive to strongly repulsive. The obvious solution to this problem should be to increase the radius of curvature of the sphere. The most extreme realization of this would be to use a completely flat counter-surface.

We approach this non-trivial solution of a completely flat counter-surface in three different ways, as is summarized in the next section.

2.5 Sliding flat surfaces over NP arrays

In this section, we describe three approaches to realize the ideal contact geometry between a completely flat surface and a nanopillar array. The first two approaches are for special AFM tips with a flat contact surface, while the third is for an extended NP array and a macroscopic counter-surface. In the Bruker Multimode 8 AFM that we have used for our AFM/FFM experiments, the cantilever is positioned in its standard slot under a fixed angle of 13.5°. For most applications, this is extremely useful, because this positioning angle prevents undesired mechanical contact of the specimen with the cantilever beam itself during the AFM and FFM scans. Even with this large positioning angle, the ball-shape tip that we introduced in the previous section, was very easy to use as it did not require any adjustments of the orientation of the cantilever holder. Truly flat contact geometries introduce major alignment difficulties in the AFM/FFM experiments.

Approach 1: Focused Ion Beam milled AFM tips

We have used the PMMA ball-shaped tip, introduced in the previous section and cut its lower part by means of a Focused Ion Beam (FIB). Over the last decades the FIB has developed into a powerful technique in the manipulation of nanostructures and the characterization of materials [30]. For example, it can be used for preparation and analysis of cross-sections and for the nanofabrication of devices. It allows one to mill down surfaces with a controlled flux of ions, reaching nanometer precision. In our application, we used FIB milling to adjust the shape of the PMMA ball-shaped AFM tip. In this way, we obtained a flat section with a relatively low surface roughness. Prior to the FIB milling, we deposited a thin layer of Au on it to avoid surface charging and heat-related problems during the milling. The cut was performed under an angle of 13.5° with respect to the cantilever (Fig. 2.14 a, b). This angle was necessary to compensate for the inclination of the cantilever in the AFM holders, discussed above. The diameter of the resulting flat area was approximately 5.5 µm, thus scaling up the contact area of the probe by an order of magnitude with respect to the area encountered for the contact to the PMMA sphere (previous section). Even though the SEM images are difficult to quantify, we estimate the surface roughness of the flat face to be below 10 nm.

<div align="center">a)   b)</div>
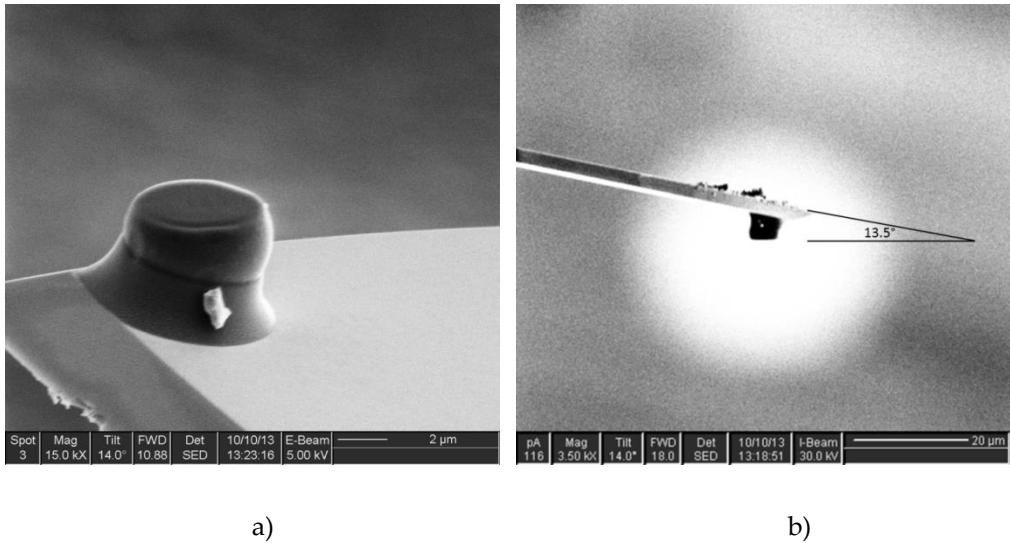
Figure 2.14. SEM micrographs of the FIB processed PMMA probe. Note the 13.5° inclination angle that compensates for the standard mounting orientation of the cantilever in the AFM/FFM cantilever holder.

Ideally, the flat section on the PMMA tip should be parallel to the NP array and remain always in proper mechanical contact due to the strong adhesion force. We also counted on the adhesion force to be the mechanism to compensate for minor, residual misalignments, keeping the tip in intimate contact with the NP array. In a first test, we brought the flat tip in contact with a flat Si surface. Figure 2.15 displays height and force measurements. Even though the scan size of $500 \ x \ 500 \ nm^2$ is smaller than the flat section on the tip, the height and lateral force images show a significant amount of structure. This probably reflects an angular misalignment between the flat tip and the Si surface, which we estimate to be in the order of $\pm 0.5°$. In addition, due to imperfections of the FIB milling (local heat melting of PMMA etc.), we could not avoid some sharp edges. Therefore, the FIB milled tip still is not flat enough, which has added to the resolution with which the Si surface topography was imaged by the AFM and FFM scans (Fig. 2.15a,c). Presumably for the same reasons, the adhesive interaction between the tip and the substrate was relatively low (Fig. 2.15d). The average friction coefficient between these sharp edges and the Si was measured to be $\mu \approx 0.44$ (Fig. 2.15b). The surface

of the PMMA tip was not inspected for possible wear after the test, in view of the high risk of e-beam induced melting during SEM inspection.
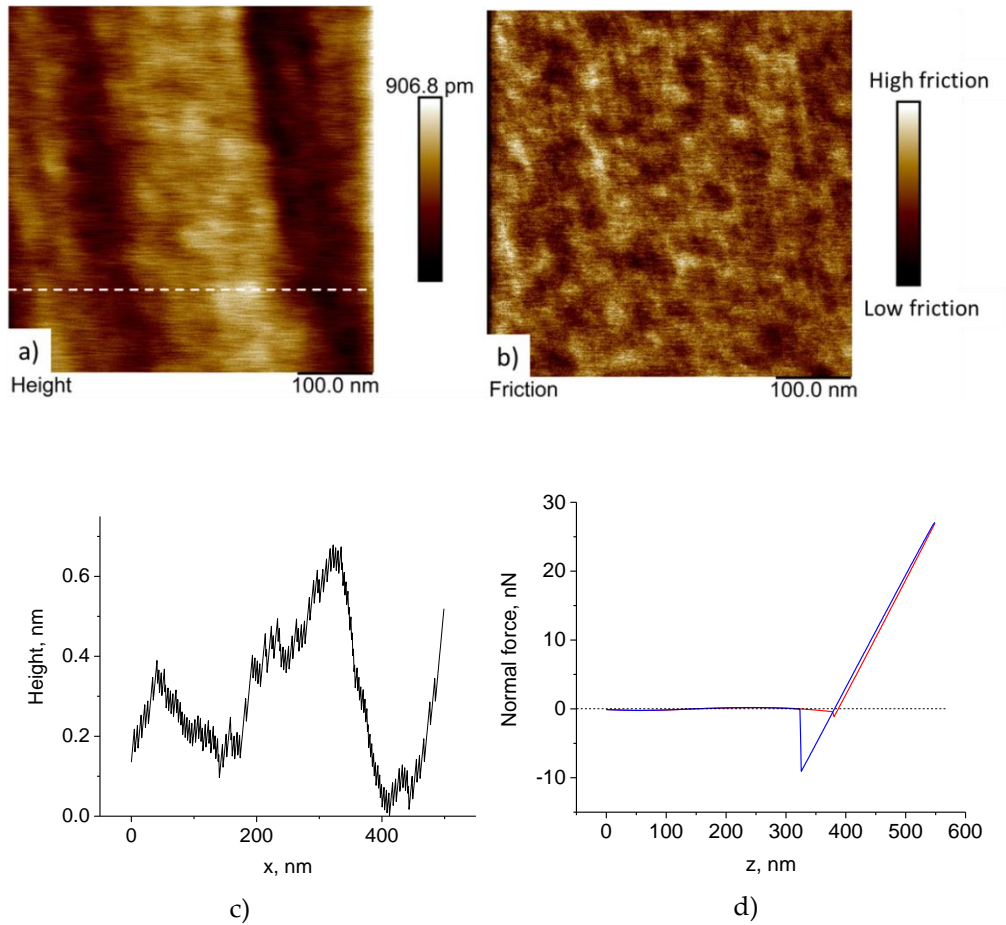
Figure 2.15. FFM measurement of a flat Si surface 500×500 nm² with the FIB processed PMMA tip. A comparison between height (a) and lateral force channel (b) in trace direction. A height cross-section (c) is taken along a dash line in (a). d) Force-distance curve measured on the flat Si with flat tip. Normal load 37 nN ($F_N = F_{mech} + F_{adh} = 28\ nN + 9\ nN$). RH = 45%.

Unfortunately, in none of the measurements that we conducted with the flat PMMA-tip on the NP arrays did we manage to establish the ideal, parallel contact in a sufficiently controlled manner. Several attempt to engage into contact between the flat tip and the NPs resulted in local damage to the NP array, i.e. massive

breaking of nanopillars. Fig. 2.16 shows an example of the destroyed test pattern $3x3 \ \mu m^2$ as a result of mechanical contact with the flat PMMA tip.
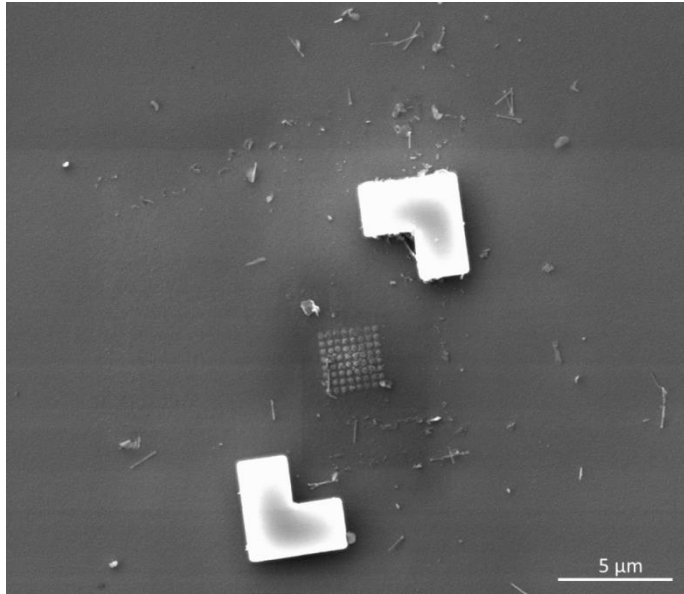
Figure 2.16. Consequence of the attempt to scan with the flat PMMA tip on top of the $3x3 \ \mu m^2$ NP array. The SEM image shows the complete destruction of the nanostructures due to the misalignment between the flat surface of the ball-tip and the NP array.

Apparently, even for a modest angular misalignment of $\pm 0.5°$ with respect to the NPs, one of the sharp edges of the milled surface of the tip would touch a sub-set of the NPs first, causing an uneven distribution of the normal and lateral forces per pillar and locally exceeding the maximum allowed force levels. Our estimate is that the angular alignment precision of the FIB milling was 0.5° and that the mounting accuracy of the cantilever in the AFM was 0.2°. We suspect that the cantilever that we used was too stiff ($k_N = 0,4 \ N/m$) to make the adhesion compensate for these errors by bending the cantilever into the desired, truly parallel orientation of the flat area on the ball tip with respect to the NP array. In view of this problem we decided not to continue our experiments with milled tips.

Approach 2: AFM with plateau-probes.

As the next method to enlarge the contact between an AFM probe and the NP arrays we chose to use plateau-ended probes. Unlike standard AFM probes, they have a truncated pyramid playing a role of a tip (Fig. 2.17). Their bottom surface is completely parallel to the cantilever beam, because both are manufactured from a single Si wafer. As no further treatment is applied to the tip, its surface roughness remains unchanged at approximately $0.5\ nm$ root mean square roughness (rms). The diameter of the plateau in Fig. 2.17 is approximately $7\ \mu m$. The cantilever beam has a normal stiffness of $k_N = 0.4\ N/m$, similar to one of the ball-shape probes discussed earlier.

The main advantage of the plateau probes is that their contacting side is extremely smooth ($0.5\ nm$ rms). They are commonly used for measurement of adhesion forces on flat samples. These measurements are typically done at high normal force in order to bend the cantilever and establish full contact between the plateau and the specimen. In our study the normal forces must remain low, so we had to revise the way to use these cantilevers.

In the first experimental solution that we tested, we installed the cantilever parallel to the specimen. For this purpose, a new cantilever holder unit for the AFM Multimode 8 system was fabricated, in which the cantilever is positioned in a slot under zero angle, instead of 13.5°. This solution allowed us to conduct several friction measurements under mild normal forces on a flat Si samples, because the cantilever does not have to bend much to establish proper mechanical contact with the surface. On the other hand, we found out that since tip height is just $7\ \mu m$, the position of the scan area on the sample had to be not further from its edge than the length of the cantilever beam ($450\ \mu m$). Otherwise, the cantilever was touching the specimen rather than the tip. For this purpose, the NPs array should be near the sample edge too; either the array is manufactured near the edge or the sample should be carefully diced to bring one of the NP arrays close to the sample edge. Unfortunately, both options are rather difficult from the technological point of view, for example due to the high risk of contamination with Si debris particles produced during dicing of the sample, the deviating thickness of the photoresist layer at the sample edge etc. In view of these complications, it was decided not to

continue with this approach and to keep the manufactured AFM holders for tribological experiments with less delicate solid samples.
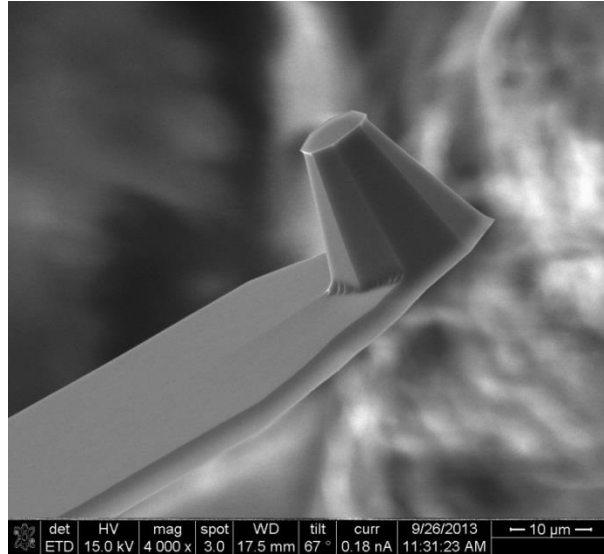

Figure 2.17. SEM micrograph of a flat-plateau AFM tip facilitated by NanoandMore [35].

Approach 3: extended flat contact.

Finally, we step away from the microscopic geometry of local contact with a small-scale NP array, which introduces, as we have seen, a number of practical difficulties. Instead, we explore the possibility to address the contact with a NP array on a macroscopic length scale. To bridge the gap between the nanosize effect of thermolubricity and the 'macro-world', we patterned a large NP array on a total area of $3 \times 3\ cm^2$. The tailored pattern on a 4-inch-diameter Si wafer (Fig.2.18) is arranged in a periodic lattice of NPs of $100\ nm$ diameter, $1\ \mu m$ height and $1\ \mu m$ pitch. The combination of their dense packing with the large area with NPs allows us to use a macroscopic piece of Si wafer as the counter-surface for the NPs. For example, if we use a piece of $1 \times 1\ cm^2$ Si wafer with a thickness of $500\ \mu m$ and make it rest by its own gravity on the NP array, the resulting normal load per pillar should be $1.5\ nN$. With this interface geometry, the sliding contact remains always fully populated with NPs. In this scenario, at low sliding speeds the entire contact should be 'lubricated' as a consequence of the thermolubricity effect. The major advantage of this approach is that the two contacting surfaces naturally maintain their mutual alignment during the sliding motion as they are placed on top of each other under the influence of gravity. The only factor that could reduce the real contact area with respect to the combined area of the covered NPs, could be a distortion (warp) of the sliding Si wafer or the wafer in which the NP array is manufactured. Over the $1\ cm$ macroscopic length scale of the overall contact, typical (out-of-plane) distortions can be in the order of one micron, strongly depending on the thicknesses of the wafers. Even in the case of such distortions, the radii of curvature involved are so large that we should expect a significant number of the NPs to be in simultaneous mechanical contact with the Si counter-surface. This makes this flat-surface approach very promising for our experiment.

Taking into account the macroscopic sizes of the samples and the correspondingly high normal and lateral forces that should be expected, the AFM/FFM setup is no longer the appropriate instrument for these experiments. Instead, the UMT friction microscope (see Chapter 4) will be a suitable measurement tool. Currently, this experiment is in its final preparation stage. The results will be reported in a separate publication.
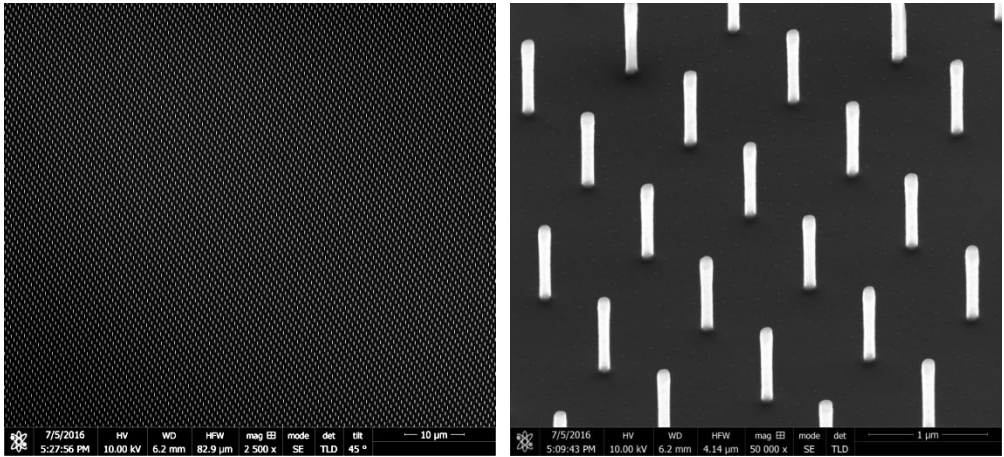
Figure 2.18. SEM micrographs of parts of a large-scale array of nanopillars ($3 \times 3\ cm^2$). Parameters of nanopillars: diameter $100\ nm$, height $1\ \mu m$, pitch $1\ \mu m$.

2.6 Summary

In summary, in this chapter we have shown the following:

1.   A Si NP can be used as a model to mimic the mechanical behavior of a single FFM tip apex, combining a high lateral vibration frequency with a large thermal vibration amplitude at room temperature. Extended arrays of such NPs potentially could be used to reduce dry, unlubricated friction at the macroscopic scale due to the effect of thermolubricity.

2.   An application of DRIE at cryogenic temperatures produces large, absolutely reproducible and well-ordered arrays of NPs with different aspect ratios up to 1:24 over distances of at least $50\ \mu m$. We have also applied RIE plasma etching to vary the shape of the pillar apices by means of etching of the HSQ resist residues. In combination with e-beam lithography, the method shows excellent versatility, anisotropy and selectivity. For details see the next chapter.

3.   The first friction tests with an AFM ball-shape tip on the produced NP arrays were conducted and have demonstrated (1) a high mechanical strength of the NPs, (2) a strong correlation between the applied normal load and the sideways bending of the NPs, and (3) a minimum in the lateral force when the spherical tip is place directly on top of one of the NP apices. The observed vertical motion of the probe indicates that the spherical tip periodically goes through geometries in which it is in simultaneous, intimate contact with a large number of bent NPs and we expect this to lead to severe damping of the thermal motion of the NPs. Possibly, this has been the reason that a clear role of thermal effects, such as thermolubricity, could not be identified.

4.   The contact area between a slider and the NP array plays a crucial role and it should be made as large as possible. A large, flat counter-surface will not have the freedom to 'sink' in between NPs that bend sideways, which may reduce the damping of the thermal fluctuations of the NPs. A complicating factor is that a larger contact is more difficult to align, while misalignments may damage the NPs when they are brought into contact with the counter-surface.

5.   A macroscopic NP array of several square centimeters is proposed as the next step towards realization of thermolubricity on a macroscopic scale.

2.7 Bibliography

1. Binnig, G., Quate, C. & Gerber, C. Atomic Force Microscope. *Physical Review Letters* **56**, 930 (1986)

2. Bennewitz, R. Friction force microscopy. *Materials Today* **8**, pp. 42-48 (2005)

3. Ruan, J.-A. & Bhushan, B., Atomic-scale friction measurements using friction force microscopy. *Journal of Tribology* 116, pp. 377-388 (1994)

4. Giessibl, F.J., Atomic Force Microscopy in ultrahigh vacuum. *Japanese Journal of Applied Physics* **33**, 6B (1994)

5. Butt, H.-J., Capella, B. & Kappl, M. Force measurements with the atomic force microscope: Technique, interpretation and applications. *Surface Science Reports* **59**, pp. 1-152 (2005)

6. Maver, U., Velnar, T., Gaberscek, M. & Planinsek, M. Recent progressive use of atomic force microscopy in biomedical applications. *Trends in Analytical Chemistry* **80**, pp. 96-111 (2016)

7. Carpick, R. & Salmeron, M. Scratching the surface fundametal investigation of tribology with atomic force microscopy. *Chemical Review* **97**, pp. 1163-1194, 1997

8. Bhushan, B. Nanotribology, nanomechanics and nanomaterials characterization. *Philosophical Transactions of the Royal Society of London A: Mathematical, Physical and Engineering Sciences* **366**, pp. 1351-1381, 2008

9. Jinesh, K., Krylov, S.Y., Valk, H., Dienwiebel, M. & Frenken, J. Thermolubricity in atomic-scale friction. *Physical Review B* **78**, 15440 (2008)

10. Li, Q., Dong, Y., Perez, D., Martini, A. & Carpick, R. Speed Dependence of Atomic Stick-Slip Friction in Optimally Matched Experiments and Molecular Dynamics Simulations. *Physical Review Letters* **106**, 126101 (2011)

11. Hölscher, H., Schirmeisen, A. & Schwarz, U. Principles of atomic friction: from sticking atoms to superlubric sliding. *Philosophical Transactions of the Royal Society A: Mathematical, Physical and Engineering Sciences* **366**, pp. 1383-1404 (2008)

12. Gnecco *et al.* Velocity Dependence of Atomic Friction. *Physical Review Letters* **84**, pp. 1172-1175 (2000)

13. Fujisawa, S., Kishi, E., Sagawara, Y. & Morita, S. Atomic-scale friction observed with a two-dimensional frictional-force microscope. *Physical Review B* **51**, pp. 313-318 (1995)

14. Dienwiebel, M., Pradeep, N., Verhoeven, G., Zandbergen, H. & Frenken, J. Model experiments of superlubricity of graphite. *Surface Science* **576**, pp. 197-211 (2005)

15. Tomlinson, G.A. A molecular theory of friction. *The London, Edinburgh, and Dublin Philosophical Magazine and Journal of Science* **7**, pp. 905-939 (1929)

16. Krylov, S.Y., Dijksman, van Loo & Frenken, J. Stick-Slip Motion in Spite of a Slippery Contact: Do We Get What We See in Atomic Friction? *Physical Review Letters* **97**, 166103 (2006)

17. Krylov, S.Y. & Frenken, J. Atomic-scale friction experiments reconsidered in the light of rapid contact dynamics. *Physical Review B* **80**, 235435 (2009)

18. Krylov, S.Y., Jinesh, K., Valk, H., Dienwiebel M. & Frenken, J. Thermally induced suppression of friction at the atomic scale. *Physical Review E* **71**, 065101 (2005)

19. Verhoeven, G., Dienwiebel, M. & Frenken, J. Model calculations of superlubricity of graphite. *Physical Review B* **70**, 165418 (2004)

20. Zhao, X., Hamilton, M., Sawyer, G. & Perry, S. Thermally Activated Friction. *Tribology Letters* **27**, pp. 113-117 (2007)

21. Gnecco, E., Riedo, E., Bennewitz, R., Meyer, E. & Brune, H. Thermally activated phenomena observed by atomic force microscopy. *Mrs Proc* **790**, P1.3 (2003)

22. Socoliuc, A., Bennewitz, R., Gnecco E. & Meyer, E. Transition from stick-slip to continuous sliding in atomic friction: entering a new regime of ultralow friction. *Physical review letters* **92**, 134301 (2004)

23. Krylov, S.Y. & Frenken, J. Thermal contact delocalization in atomic scale friction: a multitude of friction regimes. *New Journal of Physics* **9**, 398 (2007)

24. Meirovitch, L. Fundamentals of Vibrations. *McGraw-Hill Education* (2003)

25. Antonov, P.V., Zuiddam, M.R. & Frenken, J.W.M. Fabrication of high-aspect ratio silicon nanopillars for tribological experiments. *Journal of Micro/Nanolithography, MEMS and MOEMS* **14**, 044506 (2015)

26. Jiao, F. & Cheng, K. An experimental investigation on micro-milling of polymethyl methacrylate components with nanometric surface roughness.

Proceedings of the Institution of Mechanical Engineers, Part B: Journal of Engineering Manufacture **228**, pp. 790-796 (2013)

27. Riedo, E., Lévy, F. & Brune, H. Kinetics of Capillary Condensation in Nanoscopic Sliding Friction. *Physical Review Letters* **88**, 185505 (2002)

28. van Zwol, P.J., Palasantzas, G. & Hosson, Th.J.M. Influence of roughness on capillary forces between hydrophilic surfaces. *Physical Review E* **78**, 031606 (2008)

29. Capella, B. & Dietler, G. Force-distance curves by atomic force microscopy. *Elsevier*, Lausanne (1999)

30. Munroe, P.R. The application of focused ion beam microscopy in the material sciences. *Materials Characterization* **60**, pp. 2-13 (2009)

31. Liu, W., Bonin, K. & Guthold, M. Easy and direct method for calibrating atomic force microscopy lateral force measurements. *Rev Sci Instruments* **78**, 063707 (2007)

32. Prandtl, L. Ein Gedankenmodell Zur Kinetischen Theorie Der Festen Körper. *Journal of Applied Mathematics and Mechanics* **8**, pp. 85-106 (1928)

33. Palacio, M. & Bhushan, B. Normal and Lateral Force Calibration Techniques for AFM Cantilevers. *Critical Reviews in Solid State and Materials Sciences* **35**, pp. 73-104 (2010)

34. Meyer, E., Overney, R.M., Dransfeld, K. & Gyalog, T. Nanoscience: Friction and Rheology on the Nanometer Scale. *World Scientific Publishing*, Singapore (1998)

35. https://www.nanoandmore.com/afm-tips.php *Visited on 18/10/2016*

36. We assume that in Fig. 2.9 the maximum value along the retraction curve corresponds to adhesive interaction of the ball-tip with a single NP and equals approximately to $40\,nN$. Considering a number of pillars simultaneously participating in the direct contact with the ball-tip during its sliding ($\approx 25 \div 30$ NPs, see Fig. 2.7), a total adhesion force at the interface is estimated to be $\approx 1000 \div 1200\,nN$.

Chapter 3

Fabrication of high-aspect ratio silicon nanopillars for tribological experiments

3.1 Introduction

3.1.1 Overview of relevant nanomanufacturing techniques

Over the past decade, nanostructured surfaces have become widely used in electronics [1], biomedicine [2], photonic crystals [3], battery technology [4], solar cells [5], etc. Independently of the area of application, the most important points of interest of nanofabrication control are the shapes that can be manufactured, including the aspect ratios of extreme shapes such as nanopillars (NPs), and the reproducibility with which the final structures can be produced.

From a technological point of view, the manufacturing process of NPs over macroscopic areas presents a relatively complex task, even though a wide range of literature is available describing various methods for producing NP arrays. As an example, the traditional method of so-called 'natural lithography' [7,8] serves as a flexible and affordable technological platform, both technically and economically, that provides good control over the pitch and sharpness of the structures [9,12]. The natural lithography method employs self-assembly of nano- or microparticles from a solution that is spin-coated on top of the substrate. The resulting layer of particles serves as a mask for the subsequent process of etching. However, it is not possible to avoid irregularities due to the uneven distribution in the self-assembled pattern of particles. The latter may result in height variations after etching, thus inhomogeneity in the nanopillar array.

Conventional ultraviolet- (UV) and holography-based lithography could also be effective approaches [23]. Generally, these methods are based on the optical projection of a geometrical pattern from a photomask, directly to the substrate that is coated with a photoresist. With this method, modifications in the final structures (size, shape, distribution) are restricted, because one needs to fabricate a separate photomask for each pattern, which is costly. Moreover, conventional cleanroom ultraviolet lithography (instead of deep or extreme ultraviolet) delivers a resolution of $\sim 0.5\ \mu m$ [10, 11]. This modest resolution may not be sufficient to produce nanopillars, which, in our case, have to be as small as $50\ nm$ in diameter.

Another conventional method is nanoimprint lithography [13, 22]. Conceptually the method employs the imprinting of a nanoscale template ('stamp') onto the substrate ('replica') under the action of a certain normal force. Recently, an

extreme vertical resolution below $2\,nm$ was achieved with this method [22]. On the other hand, similar to the case of UV lithography, this method requires separate stamps for different patterns.

These factors explain our preference for electron beam lithography [14-16]. With this method, it is possible to produce large areas, up to several square centimeters, of round shape patterns with a precision of $2 \div 5\,nm$. Electron beam lithography enables us to manufacture these NP patterns following well-established recipes and to reach high quality and reproducibility. The versatility of this method is also due to the fact that an electron beam can directly write any desired pattern in an electron-beam-sensitive resist layer. Therefore, no photomasks or stamps are needed.

3.2 NP fabrication

Figure 3.1 shows schematically the main steps of the NP fabrication process. As substrates, we used $10 \times 10\,mm^2$ pieces of Si(100) wafer (p-type). Prior to processing, samples were cleaned in two steps. Firstly, they were placed for $5\,min$ in acetone in an ultrasonic bath and were then rinsed with DI water. Secondly, the samples were transferred to a fuming nitric acid (99.9%) HNO_3 bath and kept there for $7\,min$. They were then rinsed with DI water and dried with N_2. In order to remove residual moisture, the Si samples were baked for $2\,min$ at $250°C$. To write a pattern on the Si samples we used a negative tone hydrogen silsesquioxane (HSQ) resist (XR-1541 Dow Corning, 6% in H_2O). This particular choice is motivated by two factors: first, this resist provides a high resolution and a high selectivity during its exposure to the electron beam in the Electron beam pattern generator (EBPG); second, it has a subsequent low etch rate [7], which enables etching of the high-aspect-ratio NPs. The HSQ resist was first heated to room temperature, after which it was applied directly to the Si substrate, as it did not require any primer due to its strong atomic binding to the substrate. Spin coating was conducted for $55\,sec$ at rotation speeds in the range of 4000 to $5500\,RPM$, depending on the required aspect ratio of the pillars. The final resist layer thickness ranged between $80\,nm$ at low rotation speeds and $60\,nm$ at high speeds.
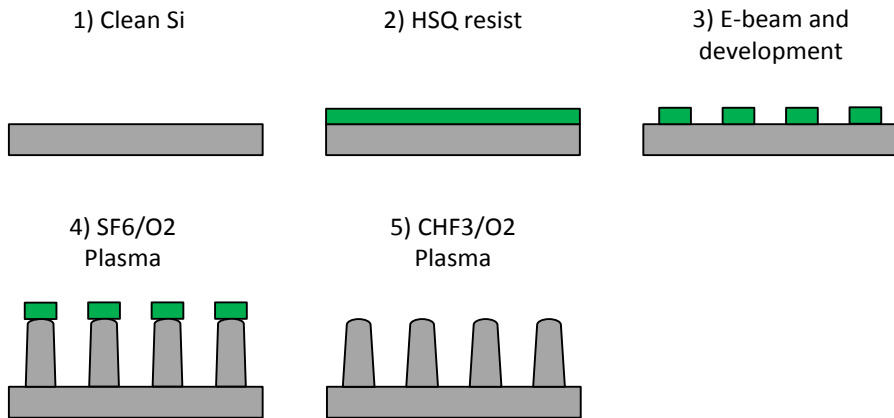
Figure 3.1. Schematic of the step-by-step fabrication process of the NP arrays.

To obtain a high lithography contrast, the samples were then baked at $80°C$ for $4\,min$. The nanopatterns were written in the HSQ layer by means of a Vistec 5000+ Electron Beam Pattern Generator (EBPG). The thinnest NPs that we have manufactured, had a diameter of $50\,nm$. All patterns were specified by use of the AutoCAD 2013 program and then converted to the corresponding EBPG format. Typically, each of the NP arrays was generated over an area of $50×\,50\,\mu m^2$. Optimum resolution was achieved for an electron dose of approximately $1950\,\mu C/cm^2$ at an acceleration voltage of $100\,kV$. After exposure, the patterns were developed in a 25% tetramethylammonium hydroxide solution (TMAH) in H_2O for $30\,sec$ at a temperature of $80°C$. Immediately afterwards the samples were carefully rinsed with DI water for $30\,sec$ and flushed with N_2. We have used cryogenic Deep Reactive Ion Etching (DRIE) to etch the pillars. This technique is the most powerful and precise method for manufacturing high-aspect-ratio structures in Si [11, 17-19]. The etching was carried out in an Adixen AMS-100 Plasma Etcher. The discharge was generated by an RF Inductively Coupled Plasma (ICP) source, directly connected to the working chamber, as shown in Fig. 3.2. The second RF source was connected directly to the specimen table, to provide sufficient directional ion bombardment onto the surface of the sample.
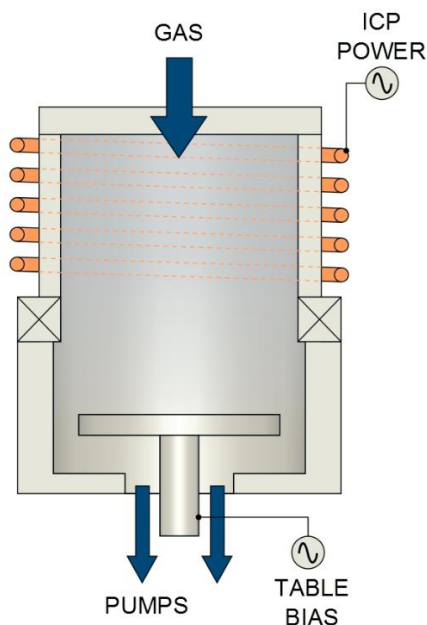
Figure 3.2. Schematic of RF Inductively Coupled Plasma system [21], used for the Deep Reactive Ion Etching of the NP patterns.

The sample was clamped to a cryogenic holder that was cooled by a flow of liquid N_2. Helium was back-streamed below the holder in order to provide enough thermal contact between the sample and the holder so as to maintain a working temperature of $-120°C \pm 0.5°C$. SF_6 was chosen as the working gas, as this provides active fluorine atoms on the sample to react and form an etching product with Si, which is volatile SiF_4. Oxygen was added to the SF_6, in order to passivate the sidewalls of the vertical structures during etching and thus avoid potential undercut. The optimal gas flow ratio for this process was established experimentally as $SF_6 : O_2 = 6.7 : 1$; specifically, the flow rate of SF_6 was $200 \ sccm$ and that of O_2 was $30 \ sccm$, at a total chamber pressure of $6 \ mbar$. An important point to note is that the optimal oxygen gas flow depended strongly on the size of the individual NP, their density on the surface and the exposed area of the silicon sample. The RF power was set to $1100 \ W$, and the bias voltage to $-40V$. With these moderate conditions we achieved a typical etch rate of Si of approximately

2400 nm/min with a selectivity of 80:1 with respect to the HSQ resist. This process produced NP arrays with varying aspect ratios (Fig. 3.3).
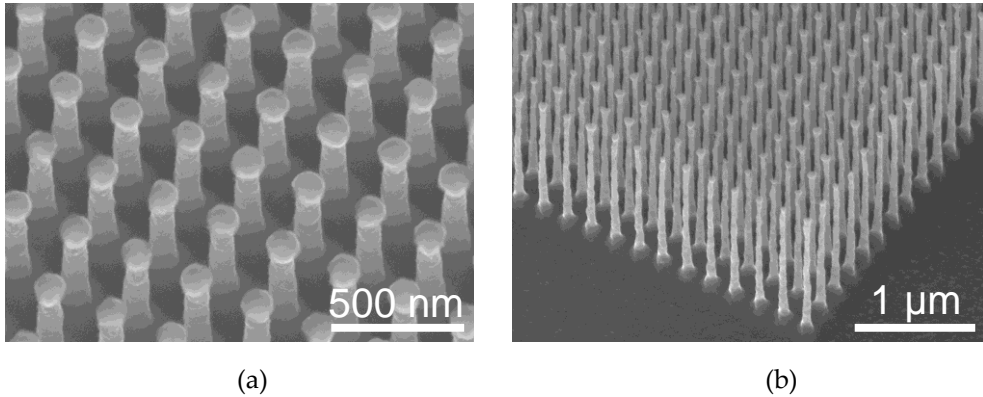

(a)   (b)

Figure 3.3. Scanning electron microscopy images of arrays of Si NPs with different aspect ratios. a) Aspect ratio 1:4, pillar diameter 95 nm, pillar length 400 nm, pitch between pillar centers 250 nm. b) Aspect ratio 1:24, pillar diameter 55 nm, pillar length 1.35 μm, pitch 200 nm. Note the resist residue, decorating the top of each NP.

3.3 Removal of resist residues

Since the prime objective of producing these structures was to study their tribological (i.e. frictional) properties, it was important to have control over the shape, composition and mechanical properties of the apices of the pillars. This issue was addressed in combination with the removal of the resist residues that remained on top of the pillars after the DRIE procedure. We considered three options for the removal of the HSQ residues. The first option was to dissolve these residues, which are chemically similar to SiO_2, in a hydrofluoric acid solution. We found that a 7% buffered HF solution readily dissolved the HSQ residues, as was expected, but that this treatment had a deleterious effect on the shapes of the pillars, especially for aspect ratios more extreme than 1:12. After HF etching, these had become very rough. In turn, certain pillars, which had undergone the under-etching effect below the resist after the DRIE (see Fig. 3.3a), showed an inhomogeneous height distribution after etching. Their thin top part had the smallest diameter, which thus was etched away faster than the thicker bottom part.

The second option was to use wet etching of the pillars themselves, in order to shrink their diameter uniformly, until the residues would detach. It was reported in [20] that it is possible to slowly and uniformly shrink the diameter of pillars by etching them in dilute aqua regia. In line with the recipe of Ref. [20], we immersed our samples in a solution of HNO_3 : HCl : H_2O = 1 : 3: 6 (volume fractions) for approximately 12 hours. However, the result showed a negligible etch rate and did not provide any significant changes. We speculate that the DRIE etching at $-120°C$ with O_2 for passivation had provided extra smooth side faces with low densities of chemically active sites, which could have resulted in the negligible effect of dilute aqua regia on the NPs.

The third and only successful option was to again resort to the method of plasma etching. Utilizing an inductively coupled CHF_3 plasma in combination with O_2 for passivation provided the required combination of high anisotropy and selectivity between silicon dioxide and silicon. The etching process was conducted in a Leybold Heraeus Plasma Etcher at room temperature. The following etching parameters were found to achieve the optimal result: a flow of 50 sscm CHF_3 and 2.5 $sccm$ O_2, 50 W RF power and $-680\,V$ bias voltage, at a typical, total pressure of 6 to 7 $mbar$. Under these conditions, the etch rate of silicon dioxide was approximately $36\,nm/min$, while that of silicon was some 3 times lower. This method allowed us to avoid excess undercut and to sharpen the pillars from the top. In Fig. 3.4 we demonstrate this effect for the example of pillars with an aspect ratio of 1:10. A minor smoothening effect was observed on the pillars during the etching process. We note that this treatment had a deleterious effect on the shapes of pillars with extreme aspect ratios, such as 1:24 (not shown here). That is why we decided not to (completely) remove the HSQ residues for those pillars. Depending on the etching time, the average radius of curvature of the apices of the pillars with aspect ratios less extreme than 1:10 varied from approximately 30 nm to 12 nm. This effect is illustrated in Fig. 3.5 for the case of NPs with an aspect ratio of 1:10.

(a)   (b)
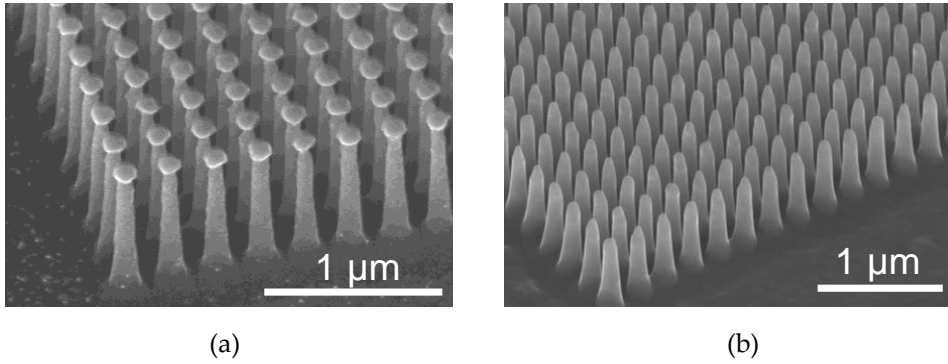
Figure 3.4. Scanning electron microscopy images, illustrating the effect of CHF₃/O₂ etching. On the left are the pillars before etching, with aspect ratio 1:10, pillar length 800 nm, pillar diameter 80 nm, pitch 200 nm. Each pillar is still decorated by a residue of the resist. The image on the right shows the result after etching. Note that the resist residues have been removed and that the pillars are slightly rounded at their apex.
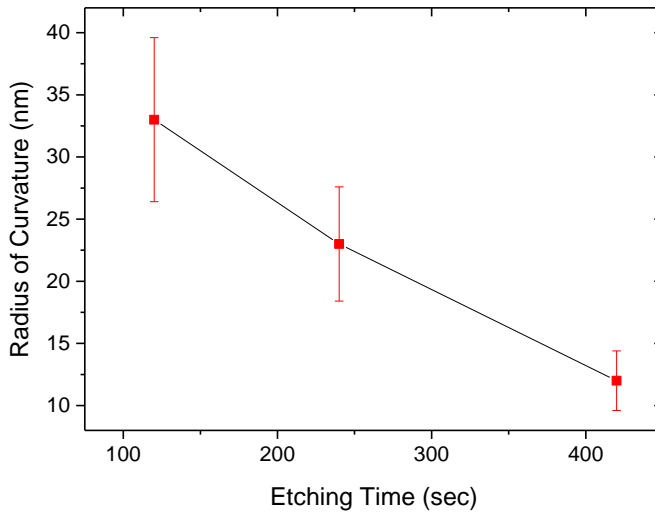
Figure 3.5. Average radius of curvature of the apices of NPs with an aspect ratio of 1:10, plotted as a function of CHF₃/O₂ etching time.

3.4 Summary

In conclusion, we have shown that DRIE at cryogenic temperatures can be used to produce large, highly reproducible and well-ordered arrays of nanopillars with various width : length aspect ratios up to 1:24 over distances of at least 50 μm. We have also applied reactive-ion plasma etching to vary the shape of the pillar apices by means of etching of the HSQ resist residues. In combination with e-beam lithography, the method shows excellent versatility, anisotropy and selectivity. In Chapter 2, the produced nanostructures are used to study their tribological properties, in an attempt to reduce dry, unlubricated friction by means of the effect of thermolubricity.

3.5 Bibliography

1. Ko H. *et al.* Multifunctional, flexible electronic systems based on engineered nanostructured materials, *Nanotechnology* **23**, 344001 (2012)

2. de Souza Antunes, A.M. *et al.* Trends in nanotechnology patents applied to the health sector, *Recent Patents on Nanotechnology* **6**, pp. 29-43 (2012).

3. Kiraly, B., Yang, S.K. & Huang, T.J., Multifunctional Porous Silicon NP Arrays, *Nanotechnology* **24**, 245704 (2013)

4. Chan, C.K. *et al.* "High-performance lithium battery anodes using silicon nanowires", *Nat. Nanotechnology* **3**, 31 (2008)

5. Liang, D. *et al.* High-Efficiency Nanostructured Window GaAs Solar Cells, *Nano Letters* **13**, pp. 4850-4856 (2013)

6. Krylov, S.Yu. & Frenken, J.W.M. The physics of atomic-scale friction: basic considerations and open questions, *Phys. Status Solidi B* **251**, 711 (2014)

7. Deckman, H.W. & Dunsmuir, J.H. Nanosphere lithography: A materials general fabrication process for periodic particle array surfaces, *Applied Physics Letters* **41**, 377 (1982)

8. Chitu, L. *et al.* Modified Langmuir-Blodgett deposition of nanoparticles - measurement of 2D to 3D ordered arrays, *Measurement Science Review* **10**, 5 (2010)

9. Hsu, C.-M., Wafer-scale silicon NPs and nanocones by Langmuir–Blodgett assembly and etching, *Applied Physics Letters* **93**, 133109 (2008)

10. Ito, T. & Okazaki, S., Pushing the limits of lithography, *Nature* **406**, 1027-31 (2000)

11. Hung, Y.-J. *et al.* Fabrication of Highly –ordered Silicon Nanowire Arrays with Controllable Sidewall Profiles for Achieving Low Surface Reflection, *Mater. Res. Soc. Symp. Proc.* **1258** (2010)

12. Huang, Z. "Fabrication of Silicon Nanowire Arrays with Controlled Diameter, Length, and Density", *Advanced Materials* **19**, pp. 744-748 (2007)

13. Torres, C.M.S. *et al.* "Nanoimprint lithography: an alternative nanofabrication approach", Mater. Sc. Eng. C **23**, pp. 23-31 (2003)

14. Vieu, C. *et al.* Electron beam lithography: resolution limits and applications, *Applied Surface Science* **164**, pp. 111-117 (2000)

15. Kaleli, B. *et al*. Electron Beam Lithography of HSQ and PMMA Resists and Importance of their Properties to Link the Nano World to the Micro World, *STW ICT Conference 2010*, Veldhoven, The Netherlands (18-19 Nov 2010)

16. Grigorescu, A.E., van der Krogt, M.C. & Hagen, C.W. Limiting factors for electron beam lithography when using ultra-thin hydrogen silsesquioxane layers, *Proceedings of SPIE* **6519** (2007)

17. Tachi, S. *et al*. Low-temperature reactive ion etching and microwave plasma etching of silicon, *Applied Physics Letters* **52**, 616 (1988)

18. Liu, Z. *et al*. Super-selective cryogenic etching for sub-10 nm features, *Nanotechnology* **24**, 015305 (2013)

19. Boufnichel, M. et al. Profile control of high aspect ratio trenches of silicon. Effect of process parameters on local bowing, *Journal Vacuum Science Technology* B **20**, pp. 1508-1513 (2002)

20. Chang, Y.-F. *et al*. Fabrication of high-aspect-ratio silicon NP arrays with the conventional reactive ion etching technique", *Appl. Phys*. A **86**, pp. 193-196 (2007)

21. Web-source: http://www.oxford-instruments.com/products/etching-deposition-and-growth/plasma-etch-deposition/icp-etch

22. Wang, X. *et al*. High resolution 3D NanoImprint technology: Template fabrication, application in Fabry–Pérot-filter-array-based optical nanospectrometers, *Microelecronic Engineering* **110**, pp. 44-51 (2013)

23. Totzeck, M. *et al*. Semiconductor fabrication: Pushing deep ultraviolet lithography to its limits, *Nature Photonics* **1**, pp. 629-631 (2007)

Chapter 4

Microscopic investigations of the lubrication mechanism of Diamond-Like Carbon

4.1 Introduction

Diamond-like carbon is a well-known solid lubricant coating used in a wide range of industrial applications to reduce excessive wear and friction. During the last decades, DLC coatings have revolutionized many technologies. High hardness and wear resistance [1-3,10], high thermal resistivity [e.g. 4,5], a low friction coefficient [3] and excellent chemical inertness [9] are the common properties associated with DLC films. This material has strongly proven itself in modern bearings, machine tools, gears, artificial human joints [8], etcetera. Due to its chemical inertness, DLC is widely used in vapor- and oil-lubricated contacts [1-5].

In parallel with increasing interest in its application, many research efforts are put into a fundamental understanding of the mechanism by which friction is lowered by DLC coatings with various chemical compositions. In the literature one finds different scenarios for the formation of a lubrication layer [e.g. 12-17, 31, 14]. Among these are the partial graphitization (or rehybridization) of the DLC surface [21-23], the passivation of the surface by water molecules [32] and the removal of a surface oxide [14].

Most previously published friction experiments on DLC have been conducted with uneven distributions of the loading force, at high speeds and without detailed control over the contact geometry. This makes it difficult to directly observe the dynamics and development of a lubrication layer on the studied DLC surfaces. Therefore, the formation process of the lubrication layer on DLC remains subject of debate.

In the present study, we focus on friction and wear of micropatterned DLC surfaces under ambient conditions, i.e. at room temperature in air at various levels of the relative humidity and in the absence of additional lubricants. We directly observe the formation of a layer of wear particles and show that its presence correlates with a reduction in the friction coefficient. We provide various local measurements on these particles that strongly favor the graphitization scenario, mentioned above.

4.2 Experimental

The experiments described in this chapter are performed on Dylyn DLC coatings (a-C:H)). The DLC films were deposited by magnetron sputter deposition on disk-shaped SiSiC substrates with a diameter of $5\,cm$. The DLC films are hydrogenated, because they were deposited in H gas atmosphere. The resulting H content in the films is estimated to be about $30\,at.\%$. The thickness of the deposited DLC films is approximately $800\,nm$. The hardness of the DLC films was measured with a nanoindenter to be $35 \pm 2\,GPa$. In order to limit the region where mechanical contact is to occur, the SiSiC substrates were micropatterned to expose three cylindrical mesas by means of plasma etching, prior to the deposition of the DLC film. The three mesas are positioned symmetrically on a $4\,cm$ diameter circle, as shown in Fig. 4.1. Each of the mesas has a diameter of $350\,\mu m$ and a height of $50\,\mu m$.
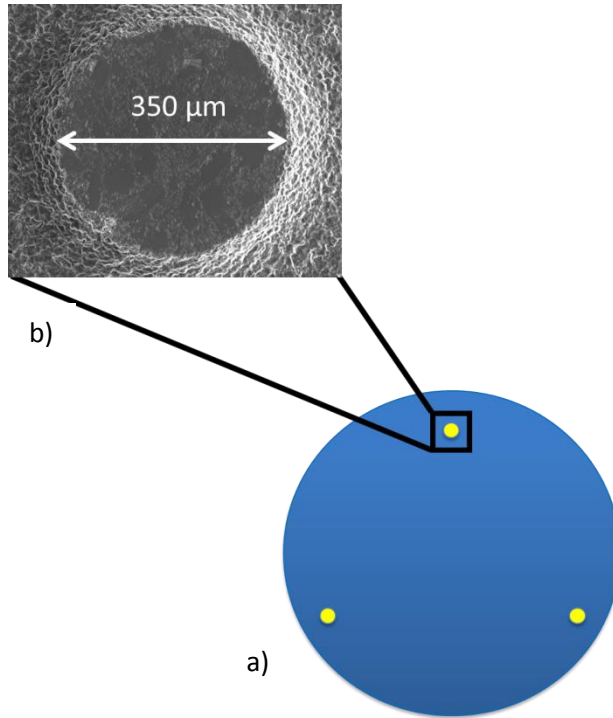
Figure 4.1. a) Principal schematic of the DLC-coated SiSiC substrate with the symmetrically positioned cylindrical mesas (yellow circles). b) SEM micrograph of one of the three mesas.

The topography of the SiSiC mesas prior to DLC deposition exhibits relatively large polished plateaus (domains) with an average roughness of $10 \div 15 \ nm$. After deposition of the DLC coating, the resulting surface roughness is nearly unchanged. A typical AFM height map of the plateaus shows long scratches and local pits, originating from the final, fine-grain polishing treatment of the substrate (Fig. 4.2).
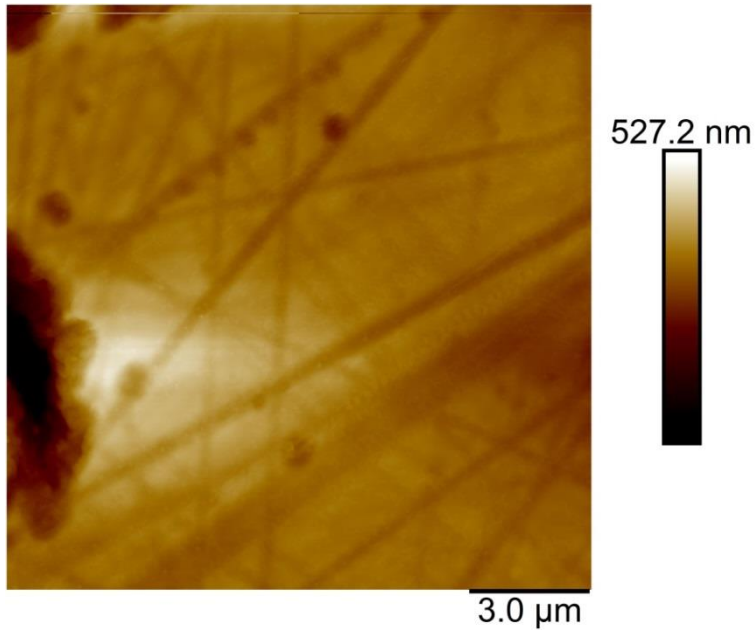
Figure 4.2. $15x15\ \mu m^2$ *AFM height image of the surface of a flat plateau on a DLC-coated mesa. The surface is composed of flat areas with scratches and pits, separated by deeper parts. An average roughness of the flat plateau is* $10 \div 15\ nm$. *Areas between the plateaus are lower than the plateaus.*

Figure 4.3 shows two optical micrographs of a DLC-coated mesa, taken with a Bruker Contour Elite 3D Optical microscope. The two micrographs represent an overview over one entire mesa and a local region of the mesa surface at higher magnification. Again, we recognize the flat plateaus and we see that they are distributed densely over the mesa and that they cover most of the surface. Consistent with the AFM image of Figure 4.2, the optical micrographs show that the regions between the plateaus are all lower than the plateaus themselves.
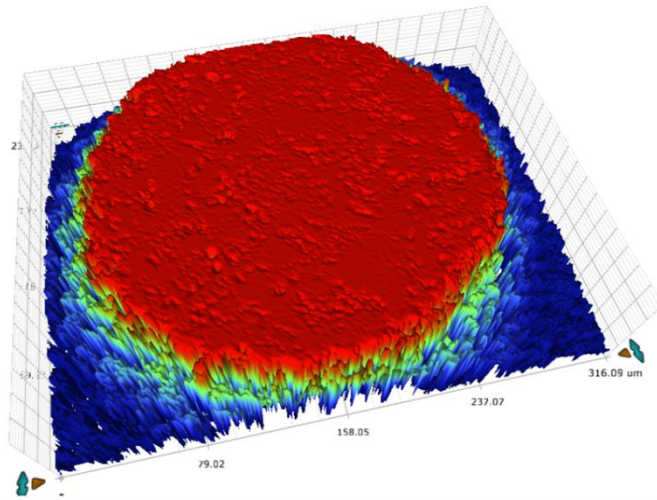
a)
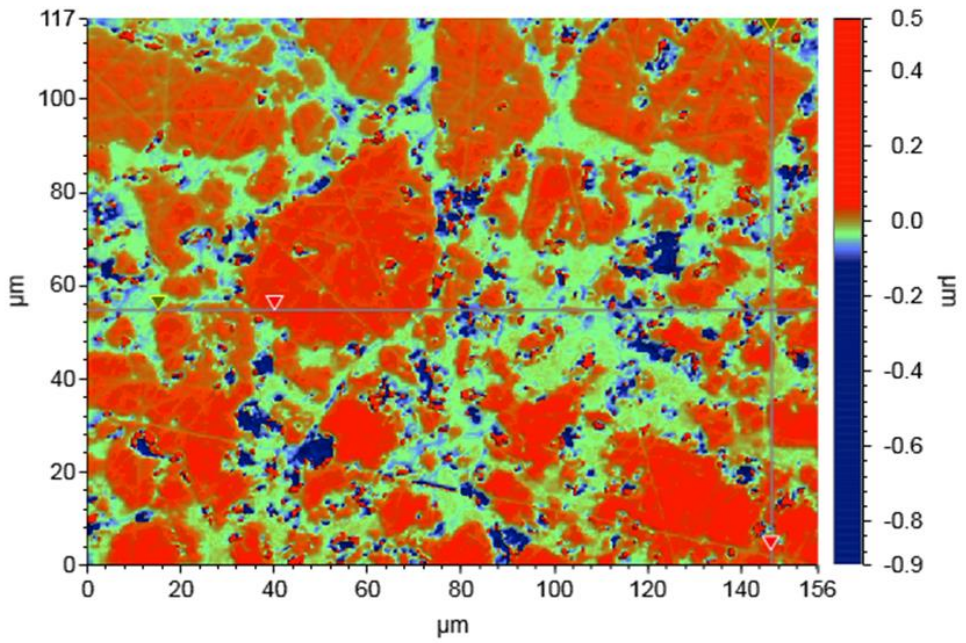
b)

Figure 4.3. 3D optical micrographs of a DLC-coated mesa. a) complete mesa; b) representative, local area of 156×117 µm² on the mesa.

As a counter-surface for the friction experiments we use 2 inch diameter Si(100) wafers with a thickness of $250\,\mu m$. Typically, these wafers are mildly warped. Using an interferometer, we measure the out-of-plane deformation to be 1 to $5\,\mu m$ across the wafer diameter. The weight of a wafer is approximately $12 \pm 0.15\,mN$. The precise value is measured for each separate wafer with a sensitive scale, prior to each friction experiment. Most experiments are conducted with untreated wafers supplied by Si-Mat Company [48], for which the surface is known to be covered by a native oxide, SiO_2, with a typical thickness of $2 \pm 0.5nm$. All friction experiments were conducted using a polished side of the Si wafers, which roughness was measured to be $0.9 \pm 0.2\,nm$ (Fig. 4.4). Some of the wafers are covered with a DLC coating, giving us the possibility to create two different tribological pairs, as will be discussed later.
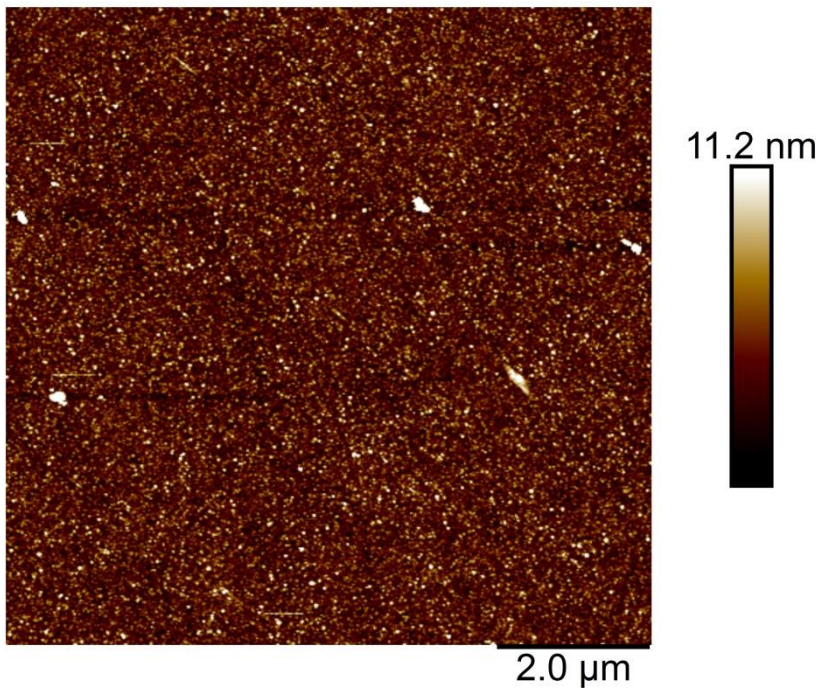

Figure 4.4. $9 \times 9\ \mu m^2$ AFM height image of a polished side of the Si wafer.

Static and dynamic friction forces are measured with a friction force microscope in the form of a Bruker Universal Mechanical Tester (UMT-1). The

microscope is equipped with a sensitive, low-noise, three-dimensional strain-gauge force sensor that has a resolution of $1\,\mu N$ for both components of the lateral force and for the normal force. The sensor can be operated in a force range from approximately $10\,\mu N$ to $12\,mN$. The maximum force value the microscope is able to measure is set by the mechanical strength of the sensor components. As a 'probe' we use a rectangular aluminum block attached to the sensor. The dimensions of this block are $5 \times 5\,mm^2$ parallel to the (horizontal) sliding interface and $15\,mm$ in height. A photograph of the measurement system and a schematic picture of the geometry are presented in Figs. 4.5 a and b. The aluminum block is used to push the silicon wafer back and forth along the micropatterned substrate, simultaneously measuring the lateral forces, exerted on the block.

In the UMT-1 setup, the three-mesa substrates are mounted on a positioning stage beneath the sensor. The stage can translate along the two lateral directions, X and Y, while the force sensor can translate along Z, all using built-in stepper motors with an accuracy of $100\,nm$. The stage can rotate (θ) with an accuracy of $10\,nrad$. A very important question is how to properly align the contacting surfaces with respect to each other. We achieve the best possible alignment without any mechanical adjustments by simply positioning the slider (i.e. the silicon wafer) onto the substrate (DLC-coated SiSiC) under the force of gravity. The silicon wafer freely rests on the DLC-coated mesas with a normal force dictated by its own weight ($12\,mN$). Friction forces are measured by using the aluminum block on the force sensor to apply tangential forces on the flat side (marker plane) of the wafer. In this way, no torque is exerted on the wafer, which therefore remains aligned and in proper contact with the substrate throughout the entire sliding experiment. The normal force can be increased by adding calibrated weights on top of the wafer.

Some experiments are conducted in reciprocating mode, using a sequence of displacements of the Si wafer back and forth along the sliding direction. This enabled us to observe run-in behavior of the DLC films without limitations on the total sliding distance. We solve this problem by means of gluing two square pieces of silicon wafer, each with dimensions of $0.5 \times 0.5\,cm^2$, on top of the unpolished side of the sliding Si wafer. They are positioned accurately with respect to the center of the wafer and aligned with respect to each other. Therefore, the aluminum block of the UMT-1 setup can be placed between them and sequentially moved back and forth to conduct the measurement of the lateral force. The

resulting value of the lateral force is found to be in good agreement (absolute difference up to 5%) with the value measured by pushing against the side of the wafer, as described above. The additional normal load due to the square blocks is $1\,mN$. Unfortunately, in some experiments we recognize that even a slight asymmetry in the gluing of the two auxiliary Si pieces with respect to the center of the sliding wafer results in differences between the values of the lateral forces measured in the forward and reverse sliding directions. On the other hand, differences of this type are fully systematic and remain unchanged during the sliding experiments. The measurement in Fig. 4.12 demonstrates such a slight asymmetry between the lateral force values for sliding in the two opposite directions.

With this experimental arrangement, a friction measurement with the UMT-1 setup is composed of a sequence of short, unidirectional sliding trajectories of typically $1\,mm$ sliding distance. At the end of each trajectory, the sliding direction is reversed. We plot the sequence of positive and negative lateral forces that are measured during a series of forward and reverse sliding trajectories into a single plot, from which we can see the full history of the friction force over the sequence.

Friction experiments are conducted at temperatures of $21 \div 25°C$. The atmosphere in the UMT-1 chamber can be controlled by passing a mixture of dry nitrogen gas and moist air through it. In this way, the relative humidity (RH) in the chamber can be varied between 1% and 90%. The RH was measured close to the substrate position with a hygrometer, Vaisala HM40 [55].

Additional topography and friction measurements on nano- and microscopic levels are performed with an Atomic Force Microscope (AFM) Dimension Icon (Bruker). Friction force measurements with this AFM are all carried out with Bruker silicon nitride V-shape probes DNP-10 with normal spring coefficients of 0.05 to 0.2 N/m.

We inspect the surfaces of the wafer and the mesas at various stages in our experiments with Scanning Electron Microscopy (SEM) and Energy Dispersive X-Ray Spectroscopy (EDX), using a FEI Verios. Micro-Raman Spectroscopy is performed on Renishaw Raman microscope, with a laser wavelength of $514\,nm$ and an exceptionally small laser spot size of $500\,nm$, enabling us to acquire local spectra on specific structural features.
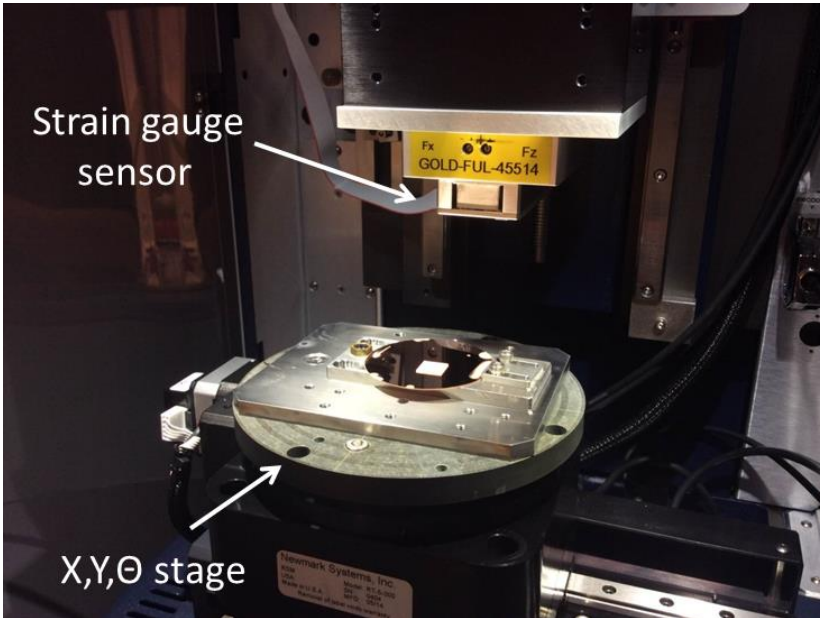
a)
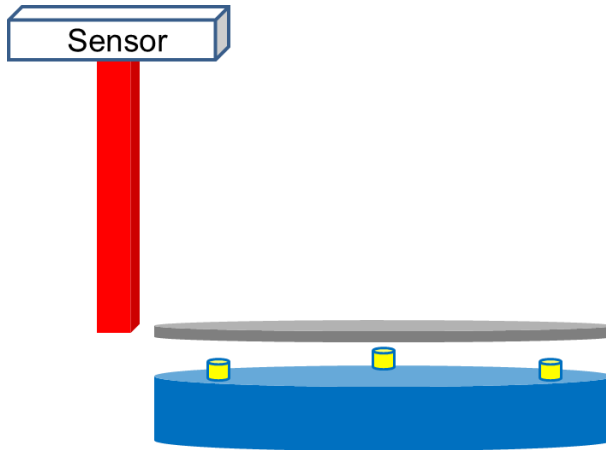
b)

Figure 4.5. a) Photograph of the Bruker Universal Mechanical Tester (UMT-1) used for most of the friction experiments in this chapter. Indicated are the translation-rotation stage on which the three-mesa substrate is mounted and the strain-gauge force sensor that is used to exert the lateral force on the sliding wafer. b) Schematics of the experimental setup, with the three mesas (yellow), the silicon wafer (grey) and the aluminum block (red) that is connected to the force sensor.

4.3 Results and discussion

The first set of experiments was conducted with pristine silicon wafers as the counter-surface. As the wafers are nearly flat, they provide a well-defined interface geometry with the DLC-coated mesas. This geometry is dictated by the detailed pattern of asperities on the three mesas and remains unchanged, irrespective of the sliding direction and speed and of changes from one silicon wafer to another.
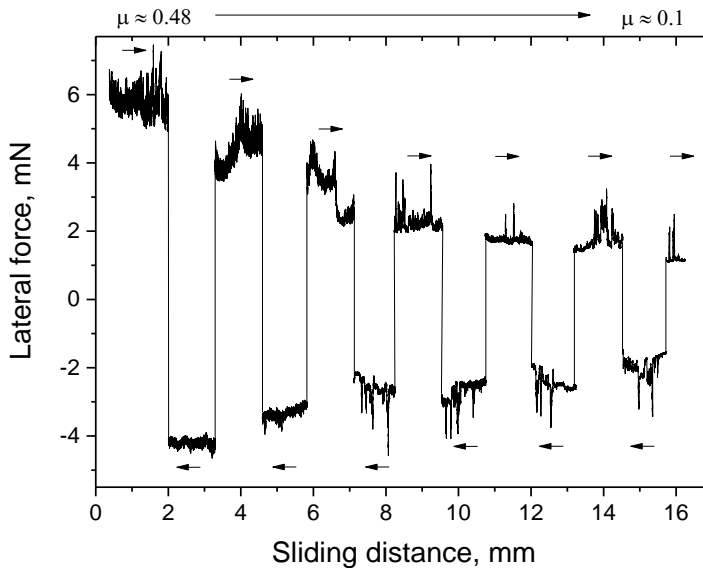
Figure 4.6. Initial reciprocating friction measurement with a silicon wafer on a 'fresh' DLC-coated three-mesa sample. The rapid reduction in lateral force illustrates the run-in process. Normal load 13 mN, velocity 10 μm/sec, relative humidity 45%. Black arrows point at the sliding direction.

Each friction experiment with a new DLC coating began with a so-called 'run-in' period, during which the friction forces started out high and gradually decreased to low and stable values. Figure 4.6 illustrates the run-in process for a new silicon wafer sliding for the first time on a substrate with freshly prepared DLC-coated mesas. After a total sliding distance of only 10 *mm*, the friction force is decreased by approximately a factor 5. This indicates that the contacting interface has undergone a dramatic change that causes excellent lubrication. We ascribe our

short run-in distance to our special geometry in which the sliding, flat silicon wafer makes contact continuously with the same asperities, which leads to their rapid modification.

Directly after the first friction measurements and total sliding distance of 15 mm, the surfaces of both the silicon wafer and the mesas were inspected with SEM and EDX in search for structural or compositional changes. The SEM images show that the mesas get decorated by third-body elements. Figure 4.7 shows a comparison of two similar regions of a DLC-covered mesa before and immediately after the run-in. Comparison of precisely the same locations prior to and after the first sliding experiment is rather difficult, because one should know beforehand at which exact location on the mesa the third-body particles will be formed first. In Fig. 4.7b one can see substantial numbers of flakes and particles distributed in depressions between the flat plateaus. The difference in contrast (i.e. in electron work function) between the SEM images in Figs. 4.7a and 4.7b indicates physical/chemical changes occurring in the top layer of the DLC during the initial sliding. We will return to this in the Results and Discussion section.

a)   b)
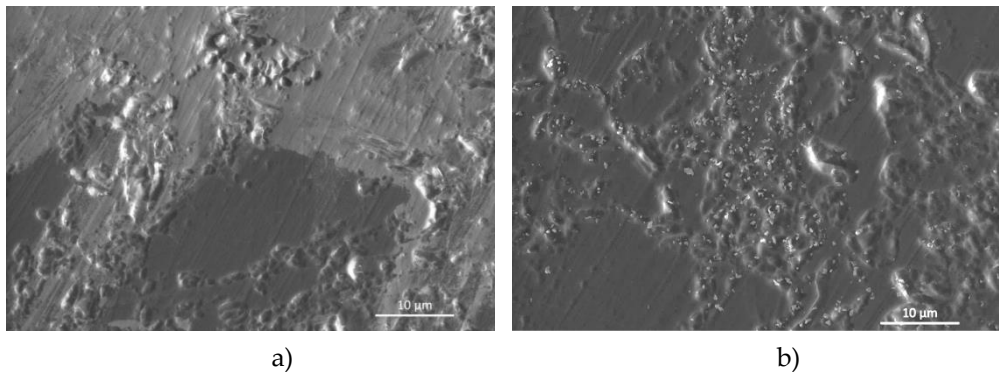
Figure 4.7. Comparison of SEM micrographs of nearly the same area of a DLC-coated mesa before (a) and after the run-in process (b) of Fig. 4.6. The arrow in panel (b) indicates one of the numerous third-body particles that decorate the mesa after the first sliding contact. Higher-resolution images of these particles are shown in Fig. 4.8.

Upon closer inspection with EDX it appears that not one but two types of new species can be identified. The first type, Fig. 4.8a, is formed by flake-like silicon particles. They form a wear product of the silicon wafer, due to its contact with the relatively sharp nano- and micro-asperities on the mesa surface. Figure

4.8b shows another location where debris has developed, the EDX spectrum showing mostly carbon and no silicon. These carbon-based flakes must be worn off from the DLC surface due to the high local stresses during the initial sliding. They are typically in the order of $0.5\,\mu m$ diameter and 10 to $25\,nm$ thick. Interestingly, some of these particles show a different contrast in the SEM images, which indicates a difference in electronic structure with respect both to the substrate and to the other particles. We will return to this observation later. According to our SEM analysis, both types of flakes can easily shear across the surface, changing their locations during the sliding of the silicon wafer on top. We conclude this, based on the absence of some of the particles in the SEM images from the DLC mesa after the sliding experiments. We find, however, that they are not likely to be transferred to the silicon surface, which shows that their adhesive interaction with the DLC surface is significantly stronger.
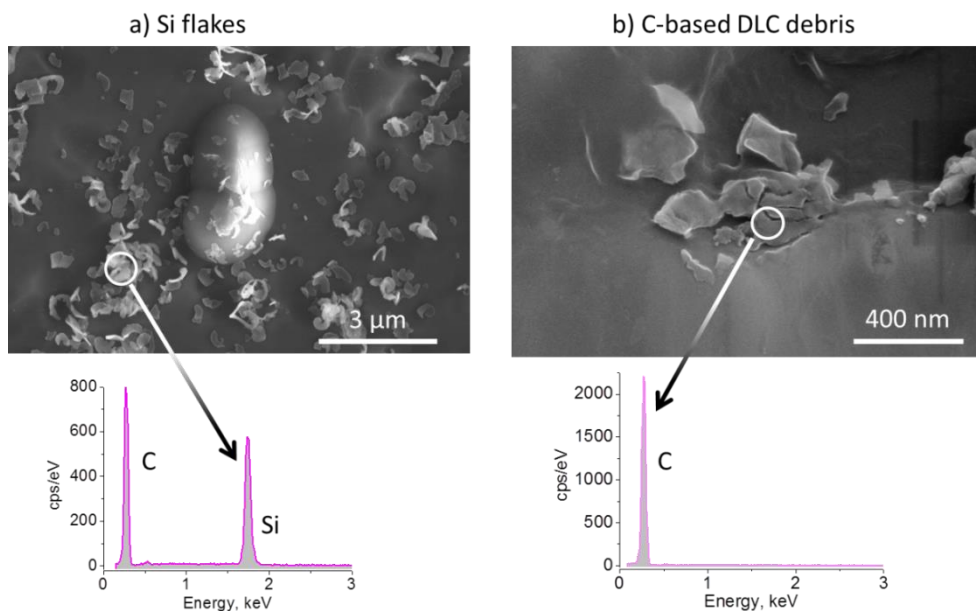
Figure 4.8. SEM images and EDX spectra on the DLC-coated mesas after the run-in process: a) silicon flakes, b) carbon-based flakes. EDX spectra are measured at the locations marked with the white circles.

In contrast with the carbon-based flakes, the silicon flakes are generated primarily within the first sliding cycles. Indeed, one can assume that during the run-in phase the silicon wafer makes direct mechanical contact only with a few microscale asperities on each of the three DLC-coated mesas. The resulting contact stresses may easily reach tens of GPa, thereby exceeding the fracture stress of bulk silicon is $10\ GPa$ in humid environment [44]). After the run-in process, contact stresses are lower and do not result in fracture of the silicon wafer anymore, even though they may remain significant – a point that will be of qualitative importance later in this chapter.

Hand in hand with the deposition of silicon flakes on the DLC-coated mesas, wear tracks are formed on the silicon wafer, in the areas where the wafer was in direct contact with the DLC mesas. Optical microscopy images (Fig. 4.9) show scratches on these locations. The total length of each wear track is equal to the sliding distance covered during the run-in phase. SEM images show two types of wear tracks, one type resulting from a continuous, smooth cutting through the silicon (Fig. 4.10a), while the other indicates a repeated chipping off (Fig. 4.11b),

reminiscent of stick-slip motion. Both types show the removal of silicon from the wafer, so that both should be expected to result in the supply of silicon flakes to the sliding interface.
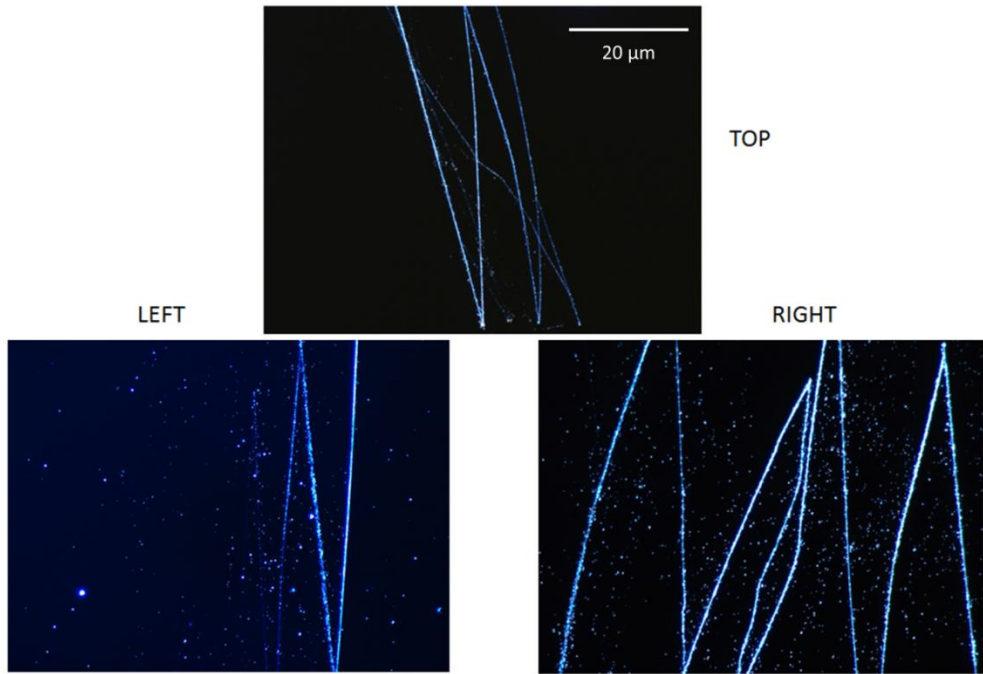
Figure 4.10. Optical micrographs (dark field) of the wear tracks formed on the sliding surface of the silicon wafer during the run-in process on the DLC-coated three-mesa surface. Note the high density of silicon particle debris along each wear track.
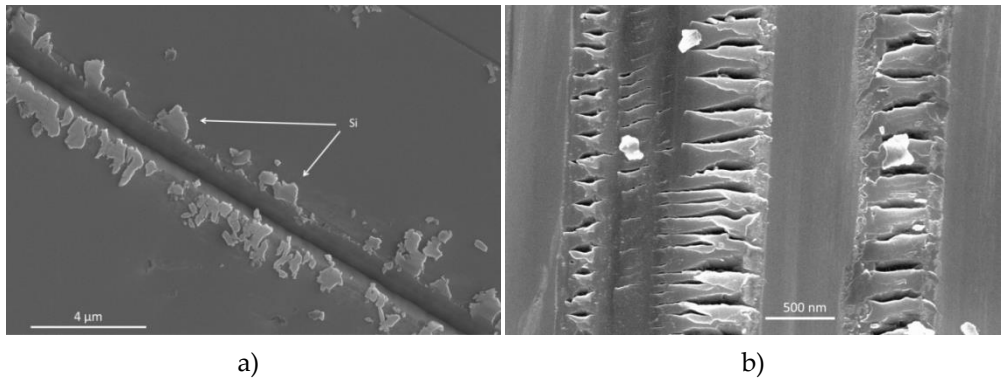
Figure 4.11. SEM micrographs of wear tracks on the silicon wafer: a) a small-scale region with a continuous cut through the silicon surface; b) a large-scale image showing the result of a 'stick-slip'-type sequence of chipping events.

Once the run-in is complete and the friction force is low, any subsequent sliding of the wafer does not lead to any further wear of the silicon wafer. When we replace the first silicon wafer, used for running in, by a fresh wafer, the friction force remains low (Fig. 4.12) and the new wafer is not scratched. Note, that there is a consistent absolute difference between the values of the lateral force measured during sliding from right to left and from left to right. This is presumably due to slight difference in position of the Si blocks placed on top of the wafer with respect to its center, as discussed above in Experimental. For this reason, here we show an average value of the friction coefficient of the corresponding reciprocating paths $< \mu >$.
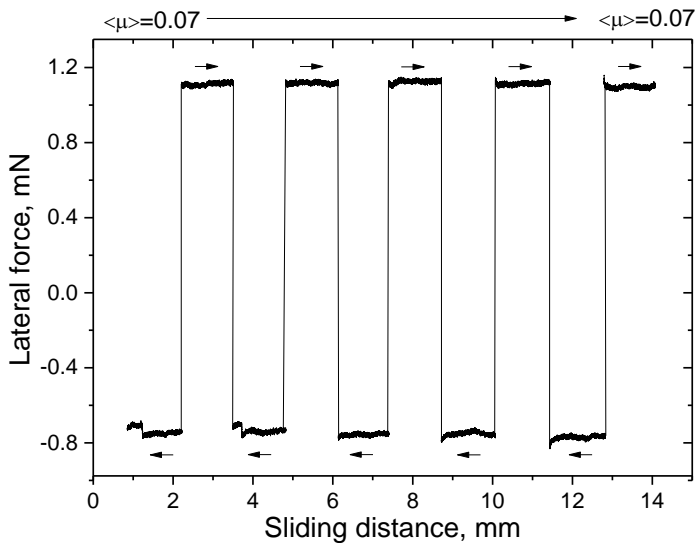
Figure 4.12. Reciprocating friction measurement performed with a fresh silicon wafer on a DLC-coated substrate, after the substrate had been run in with a separate silicon wafer, similar to the friction sequence displayed in Figure 2. Normal load $13\ mN$, velocity $10\ \mu m/sec$, relative humidity 45%. Black arrows point at the sliding direction.

During consistent inspection of the fixed locations on the DLC mesas which contain Si flakes we observed that Si flakes may move and disappear from their original position after sliding of the wafer. At the same time, we don't find them being transferred back to the Si wafer surface. We may conclude that the silicon flakes have significant mobility at the interface. This is surprising if we assume that

they exhibit similarly strong wetting by water as the (oxidized) surface of the silicon wafer [49]. In contact with the wafer under ambient conditions, the silicon flakes should then be pinned to the wafer through the formation of capillary water bridges. But as we find that they are relatively free to slide, whereas we have not observed the transfer of silicon flakes back from the DLC surface to the silicon wafer, we have to conclude that the silicon flakes, or at least their surfaces, are chemically modified. We will return to this point later in this chapter.

The dependence of the friction force on the applied normal load is measured to be close to linear for normal load values up to approximately $F_N = 40\ mN$. This can be recognized in Fig. 4.13, in which we plot the coefficient of friction (COF), defined as the ratio $\mu = F_F/F_N$ between the friction force and the normal load and where the friction force is equal to the average lateral force $F_F = \bar{F}_L$. Up to $F_N = 40\ mN$, the COF is more or less constant.

Figure 4.13. Dependence on normal load of the friction coefficient for a silicon wafer on a DLC-coated substrate. The red curve represents measurements during the loading phase, i.e. 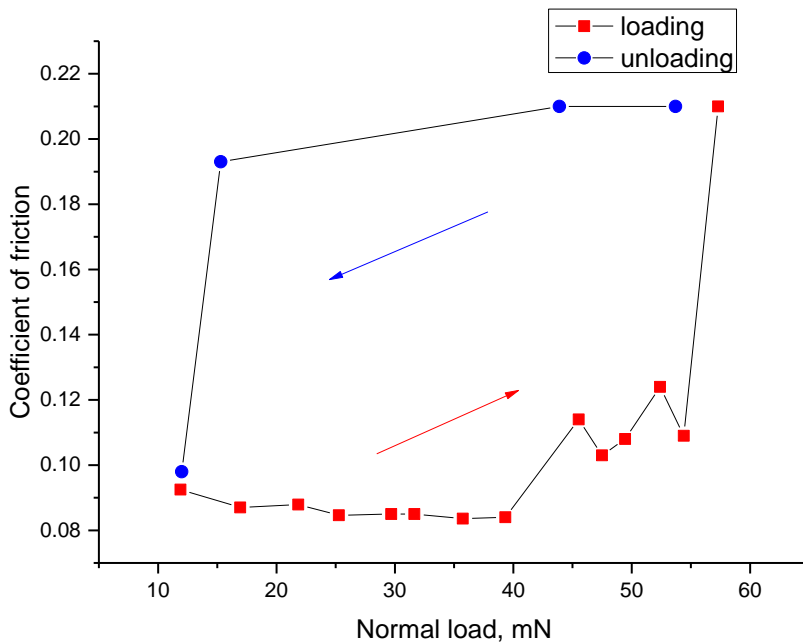while the normal load is gradually increased. The blue curve shows measurements during unloading. The weight of the silicon wafer was $12\ mN$. The

The high lateral mobility of the silicon particles was found only within a certain range of normal loads. When the normal load was gradually increased beyond 40 mN (red curve in Fig. 4.13), we observed a rapid increase of the friction coefficient. For $F_N \geq 55\ mN$, the friction force even reached the maximum value of 12 mN, at the limit of the operational range of the force sensor. In fact, the values of the friction coefficient in Fig. 4.13 higher than 0.2 are lower estimates. Along the blue curve, we gradually decreased the normal load. The wafer could slide again after we reduced the normal force to $F_N = 15\ mN$. We assume that the changes in friction coefficient are due to the pinning of the Si and DLC particles on the DLC film at high normal loads. When the load is reduced sufficiently, the particles, presumably, de-pin and regain their ability to shear across the surface. This phenomenon causes hysteresis in the loading-unloading cycle, when we load beyond a critical level. Along with this assumption, we cannot exclude another scenario which takes into account contact stresses on the surface of the silicon wafer. Let's assume that the real contact on each DLC mesa takes place only via small number of third-body particles (and asperities) with sub-micron size distribution. As discussed above, at a normal load of $F_N = 12\ mN$ after the run-in process, the Hertzian contact stresses could reach a level up to several GPa, which is roughly comparable with the ultimate strength of bulk silicon. Hence at a 5 times higher normal load (Fig. 4.13), one should already expect a gradual fracture of the silicon surface in places of real contact. As follows, in order to rejuvenate sliding motion and reach the original friction coefficient, one should decrease the normal load.

In order to demonstrate that silicon particles only help to bring down the COF by mechanical filling-in and shielding of the DLC surface, we conducted an experiment in which we partially removed them by cleaning the mesa structure after which we measured the friction force again. The cleaning was conducted in an ultrasonic bath with n-octane for 15 min at 20°C. n-Octane as a non-polar solvent increases the probability for the particles to come off the surface. In fact, using of a polar solvent (e.g. isopropanol) didn't result in removing of any particles. We assume the reason for this is an interaction of polarized solvent

molecules with the surface of the DLC film and the particles. Due to a strong dipole moment acting between them, the particles had in the particular case lower probability to come off. Interestingly, only silicon flakes were removed in this way, while C-based particles could not be removed from the mesa surface. Figure 4.14 represents SEM images of a local area on the DLC surface before and after cleaning of the DLC substrate following the proposed above procedure.
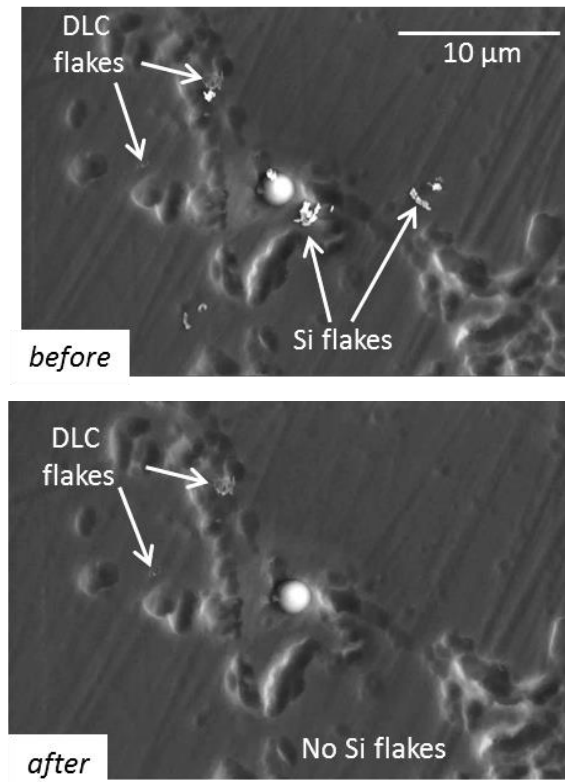
Figure 4.14. Example of the same local area on a DLC-coated mesa before (a) and after (b) ultrasonic cleaning with n-octane. Note that most of the silicon flakes created around an asperity are gone after cleaning, while the DLC flakes remain on their original positions.

In Fig. 4.15 we show a friction measurement with a fresh silicon wafer against a DLC-coated three-mesa substrate, directly after the cleaning procedure described above, in which the silicon flakes were removed. While the initial value of the COF is much lower than the starting value observed at the first run-in of the DLC coating (Fig. 4.6), the COF starts out higher than its value after that run-in, but prior to the removal of the silicon flakes. A new run-in episode is required to reduce the COF again. Note that in this process the 'noise' on the measured lateral force is high initially and that it is reduced nearly to zero during the run-in phase. After this re-run-in measurement, SEM images showed new silicon flakes at locations next to asperities and in relatively flat areas, where such flakes had been absent after the sonication. We see that the presence of the silicon flakes correlates with a modest reduction in the COF and with the suppression of the fluctuations in the lateral force.
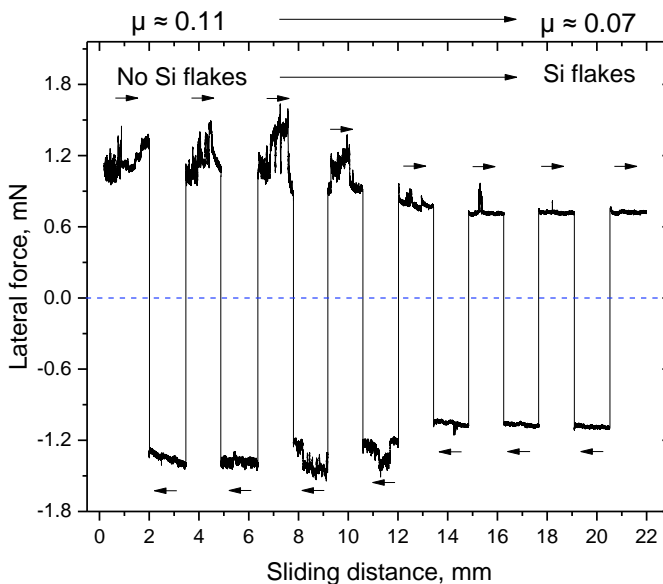
Figure 4.15. Friction measurements between a fresh silicon wafer and a DLC-coated three-mesa substrate, immediately after 'cleaning' the substrate in an ultrasonic bath with n-octane. SEM-images show that initially no flakes were present. At the end of the test a small number of new silicon flakes were observed. Normal load 13 mN, velocity 10 μm/sec and relative humidity 45%. Black arrows point at the sliding direction.

In order to completely exclude the influence of the silicon flakes on the lubrication process, in the next set of experiments we used as a counter-surface a silicon wafer coated with DLC, i.e. with the same type hydrogenated coating as the three mesas over which it was forced to slide. The thickness of the DLC coating on the silicon wafer amounted to $800 \pm 10 \ nm$. AFM topography measurements on the DLC-surface show that it has a local roughness of $1.1 \pm 0.2 \ nm$, which is similar to the roughness of the underlying silicon surface (Fig. 4.16). Therefore, the geometrical simplicity is conserved of a nominally flat counter-surface sliding over the rough surface landscape of the three mesas.
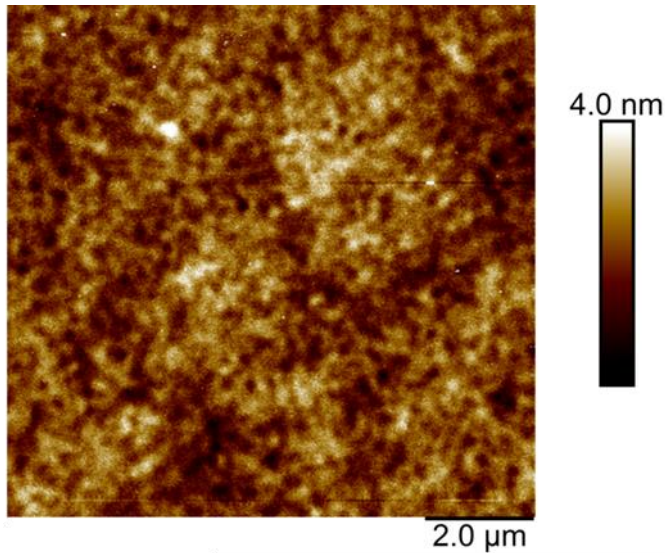
Figure 4.16. AFM height measurement on the DLC-coated silicon wafer. The root-mean-square (rms) roughness equals $1.1 \pm 0.2 \ nm$, which is similar to that of the silicon wafer.

Figure 4.17 presents a friction measurement with the DLC-coated silicon wafer against the DLC-coated mesas. During a rapid run-in process, the COF decreases during the first millimeters of sliding, reaching an average final value of 0.09 ± 0.01 and remains almost unchanged even at longer sliding distances ($> 10 \ mm$).
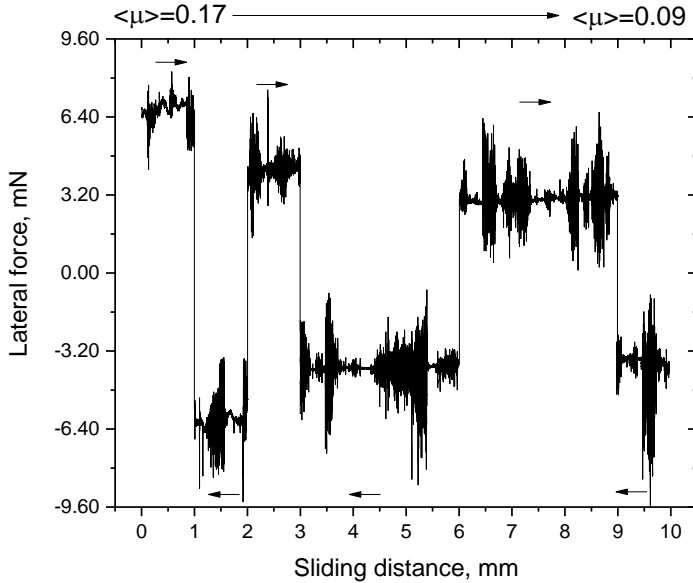
Figure 4.17. Friction coefficient during the run-in process of a DLC-coated silicon wafer against a DLC-coated three-mesa substrate. Normal load 35 mN, velocity 10 μm/sec and relative humidity 45%. Black arrows point at the sliding direction.

In the experiments with an uncoated silicon wafer sliding over the DLC-coated mesas, carbon-based particles were generated in the form of submicron flakes. In the present case, with DLC-coated surfaces sliding over each other, we first observe the formation of rather large particles, with diameters up to several micrometers (Fig. 4.18), which we ascribe to the high interfacial hardness. They originated mostly from the substrate and only minor wear loss was observed on the DLC-coated silicon wafer. Only after sufficiently long sliding distances, these particles decreased in size, probably due to the milling effect between the contacting regions. Presumably, the milling and shear sliding of the loos particles causes the noise in the lateral force signal, observed in this experiment. The final average size of most particles does not exceed the interface roughness of approximately 10 to 50 nm, dominated by the roughness of the mesas. Though minor amount of the particle still have the size larger that the interface roughness, therefore the noise remains present even at longer sliding distances (> 10 mm).
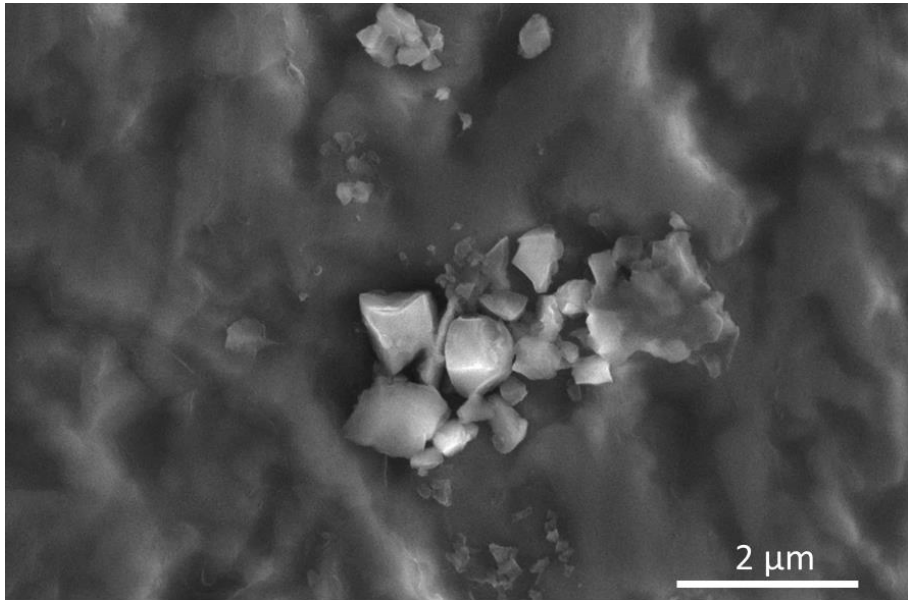
Figure 4.18. SEM micrograph of particle debris formed during the run-in period (after the first 3 mm of sliding in Fig. 4.10) at the interface between two DLC-coated surfaces.

Similar to the silicon-against-DLC experiment, the carbon-based particles formed in the DLC-against-DLC experiment could not be removed by means of ultrasonic cleaning in n-octane, following the method described above. As long as these carbon-based flakes are present on the DLC mesa surface (and also on the sliding surface of the DLC-coated silicon wafer) and the majority of protruding asperities are removed, the DLC surface is in its 'self-lubrication' regime. The low friction coefficient is conserved if the counter-surface is replaced with a different one. For example, if after the run-in process, the DLC-coated silicon wafer is replaced with a new, uncoated silicon wafer, the COF remains nearly unchanged and no further run-in behavior is observed (Fig. 4.19). Also, no scratches are formed on the silicon and no material is transferred from the silicon wafer to the DLC-coated mesas.
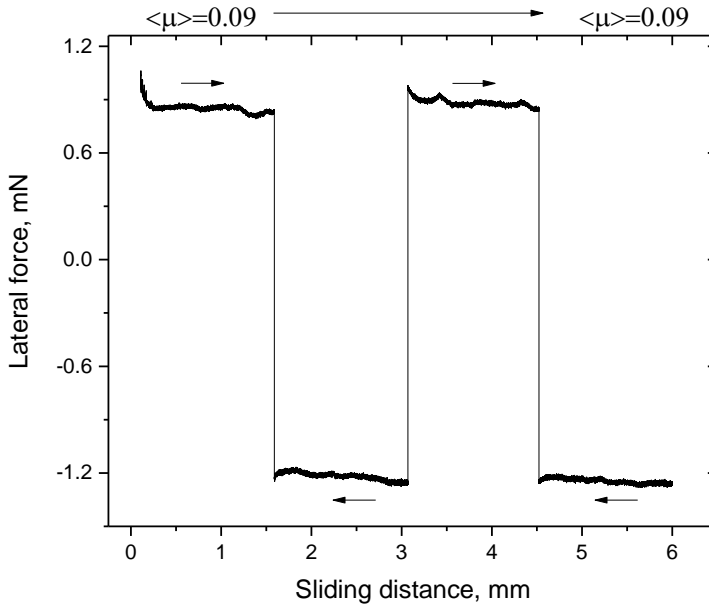
Figure 4.19. Reciprocating friction measurement with a fresh, uncoated silicon wafer sliding over a DLC-coated three-mesa substrate, after this substrate had been run in against a DLC-coated silicon wafer. Normal load 13 mN. Reciprocating speed 10 µm/sec. Relative humidity 45%. Black arrows point at the sliding direction.

Firstly, observed mobility of the Si flakes might tempt to idea that their surface got wrapped with a thin layer of carbon material transferred from the DLC surface during their initial shear. Similar scenarios of lubrication due to formation of onion-like structures on diamond particles between graphene and DLC surface were suggested earlier [18,19]. A micropillar geometry gives us an opportunity to look at individual particles in the transfer layer. Therefore we put an effort to characterize individual silicon and C-based flakes with micro-Raman spectroscopy, to find out whether above mentioned scenario could be applicable in the particular case. The measurements were performed on the silicon particles didn't reveal any structural changes: unfortunately, due to a strong background signal from DLC no significant correlation of graphitic structure present on the silicon particles was found, though a Raman laser spot was as small as 500 nm in diameter. A typical Raman spectrum on the silicon particle on DLC surface is presented on Fig. 4.20.
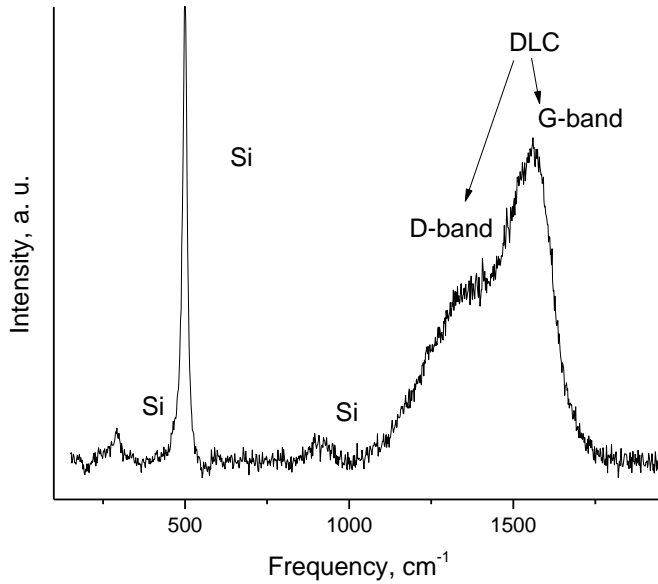
Figure 4.20. A typical Raman spectrum measured on a single silicon flake laying on the DLC surface. A part of the spectrum from $\sim 1000\ cm^{-1}$ to $\sim 1750\ cm^{-1}$ is due to the background signal from DLC.

Secondly, our observations indicate that the surface of the carbon-based particles that are formed during the run-in phase, has undergone a dramatic structural or compositional change. This is consistent with many previous studies [e.g. 13, 21-23]. The most popular scenario is that the density of carbon atoms involved in sp² bonding configurations would be increased at the surface of the DLC particles that are sheared off from the DLC coating. This increase in sp² signature would correspond to a local surface conversion from the original, hard diamond-like carbon phase, with sp³ bonding character, into a graphitic carbon network. Such a conversion is possible under sufficiently high local pressures and shear stresses. Many spectroscopic studies demonstrate agglomeration of converted carbon based particles along the wear tracks on the studied samples [e.g. 22, 50]. For the hydrogenated DLC, this process should also be accompanied with some hydrogen release from the structure and a resulting lattice relaxation. Indeed, the friction between diamond surfaces has been measured to be extreme [51]. In contrast, the friction between graphite surfaces can be vanishingly low [35]. The

combination of high stiffness within each graphite sheet and the weak Van der Waals bonding between the sheets, makes it relatively easy to shear graphite or graphene sheets over each other, particularly when they are azimuthally misaligned [35]. We have to realize that the proposed diamond-to-graphite conversion should be expected to take place only very locally, where direct mechanical contact generates sufficiently high pressures. The lubricating carbon-based particles could be decorated by graphitic carbon only over a small fraction of their surface. This makes it very difficult to prove experimentally that such a structural transformation is indeed taking place and that it is indeed responsible for the strong reduction in measured friction forces.

In order to investigate the possible structural transformation of the carbon-based particles, we performed micro-Raman spectroscopy. Special in these measurements was the use of a relatively small laser beam spot, enabling us to acquire spectra completely on a single particle or, for comparison, on the DLC areas between the particles. In order to ensure that the Raman spectrum for the particles was obtained exclusively on particles, we selected particles for this analysis with lateral dimensions larger than $800\ nm$. In Fig. 4.21, we compare a spectra in the frequency range between 900 and $1800\ cm^{-1}$ on a pristine DLC area on one of the mesas with a spectrum on a single carbon-based particle. The characteristic bands for DLC are around $1360\ cm^{-1}$ ('defect' or D-band) and $1550\ cm^{-1}$ ('graphite' or G-band) and overlap. These bands originate mainly from sp^2-bonded carbon clusters. Their intensity ratio I_D/I_G, their widths and precise peak positions are all sensitive to details of the bonding configuration and thus to possible structural changes, e.g. from sp^3 to sp^2. We used a standard Gaussian peak fitting method, which is described in detail in e.g. [24-28, 39], in order to process the acquired Raman spectra and analyze the D and G bands independently, in terms of their intensities, positions and full widths at half maximum (FWHM). A combination of these parameters serves as a measure for the relative amount of sp^2-bonding [27, 29, 30, 39]. Comparing Figs. 21b (particle) and 21a (DLC), we observe the following:

1)   a significant increase of the I_D/I_G ratio on the particle with respect to the pristine DLC, from 0.56 to 0.91. Note that this is primarily due to a significant increase of I_D, while I_G remains almost constant;

2)　　　　　a shift of the G band position towards higher frequency, from 1553 to 1560 cm^{-1};

3)　　　　　no shift of the D peak;

4)　　　　　a narrowing of the FWHM of both the D and the G band.
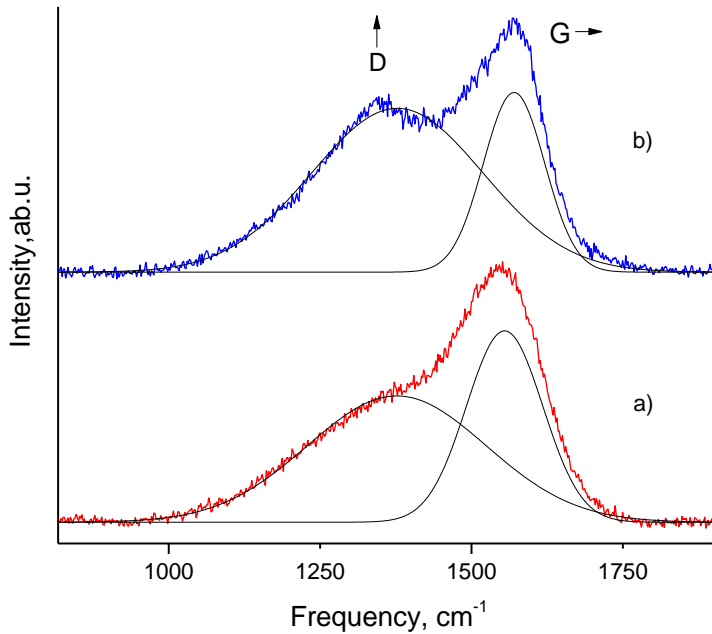
Figure 4.21. Comparison of the Raman spectra of the pristine DLC surface (a) and on top of a wear particle of the DLC (b). The black inner lines illustrate the Gaussian decomposition into D- and G-bands. The spectra are offset vertically for clarity.

We note, that the penetration depth at 514 nm wavelength of the laser can be as large as 700 nm [53]. Therefore, in all measured spectra only a part of the signal corresponds to light interaction with the surface, while the rest is due to interaction of the excitation laser light with the bulk material. The Raman spectra suggest that the investigated particles contain a relatively high number of sp^2-bonded carbon atoms in comparison with the DLC film. The particles originate from the asperities that had undergone the highest mechanical stresses due to the uneven distribution of normal load during the run-in phase. In turn this induces local atomic stresses in

the DLC, followed by transformation of metastable sp^3-bonded clusters into to more stable sp^2. In the presence of adsorbed water, the dangling bonds on the sp^2-clusters should be passivated, similar to the situation for graphite [54]. Without the dangling bonds, the sp^2-clusters can act as an efficient lubricant. Carpick *et al.* have recently shown that in addition to some rehybridization from sp^3 to disordered sp^2-bonding in non-hydrogenated amorphous carbon and ultra-nanocrystalline carbon, an essential ingredient in the solid-lubrication mechanism of amorphous carbon is the passivation of active sites (dangling bonds) with OH and H, formed due to dissociation of adsorbed water [15]. They have concluded this, based on near-edge x-ray adsorption fine structure (NEXAFS) spectroscopy measurements on the wear tracks. In our case of hydrogenated DLC, both processes play a positive role in lubrication of the solid interface. On the one hand, the increased number of sp^2-bonded carbon clusters reorganizes the particle surface and also results in rupture of C-H bonds and increasing density of carbon dangling bonds, thus increasing the surface energy. C-H bonds are known to break mechanically by the high shear stresses that develop locally during sliding [52]. On the other hand, newly created active sites on the particles get immediately passivated with water from the environment, bringing down the friction coefficient [47]. The rest of the substrate remains enriched with H, which locally passivates all dangling bonds and prevents water from adsorbing [32-34]. Also, the Raman spectrum measured on the DLC surface next to the particles does not show any sign of increasing amount of sp^2 clusters. Therefore, we conclude that the lubrication is mainly due to hybridization and/or passivation mechanisms on the wear particles, rather than a transformation of the entire DLC substrate. We defer the discussion of the dependence of friction on the relative humidity to the next Chapter, where we present experimental data.

The change in electronic structure, associated with the increase in the proportion of sp^2 bonded surface atoms on the studied particles, should be expected to cause a change of contrast of the particles in the SEM observations, as mentioned above. The reason for this is that the electronic changes should be accompanied by changes in the work function and, hence, in the secondary electron emission coefficient. A change in contrast between sp^2 and sp^3 clusters has been reported before in Transmission Electron Microscopy observations [46].

One important observation from this work is that even in our special geometry, in which the roughness is fully concentrated on one of the two contacting surfaces and the asperities on that surface seem more or less fixed in location, all major transformations of the DLC film are very local and the final contact geometry is strongly dominated by the third bodies that are formed during the initial, run-in phase. In this extremely heterogeneous geometry, the commonly used term 'wear track' is not appropriate [6, 28]. We inspected the local variations in frictional behavior on the mesa surface with AFM. Figures 4.22 a and b present maps of the friction and height of the same local region on the DLC film. The combination of these images shows that some of the highest locations exhibit relatively low friction levels, compared to the lower regions that did not experience sliding contact with the counter surface. The latter means that due to the relatively high local contact pressure, the highest regions have undergone physical or chemical changes that cause the lowering of friction on them. Ahn et al [40] studied phase images with AFM [42, 43] on DLC wear tracks. They revealed a significant inhomogeneity of the wear track across the sliding direction and reported a lower elastic modulus on the highest asperities. The latter was associated by them with a transition of the diamond-like structure to a graphite-like structure.

a)   b)

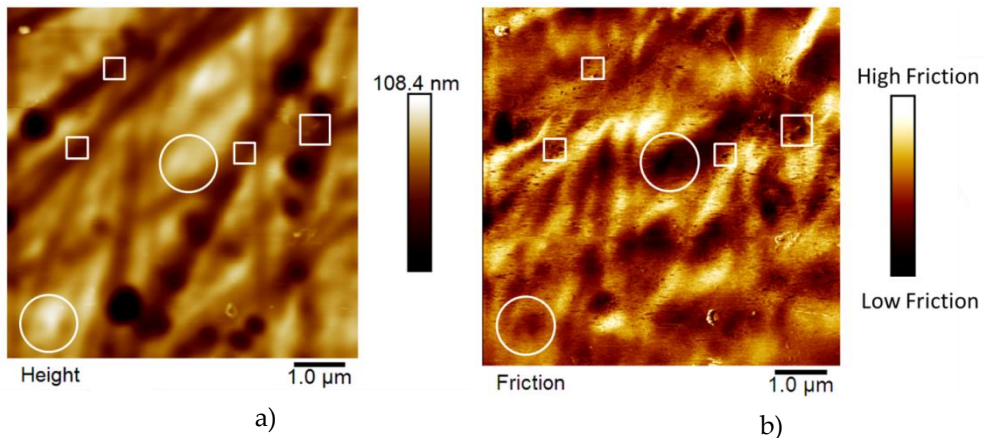*Figure 4.22. AFM measurements on a DLC-coated mesa after run-in. a) Friction force (dark colors correspond to low friction); b) Height map of the same area. White circles point at asperities on (a), which show low lateral force on (b); white squares indicate the corresponding locations and lateral force measured at the nanoscale particles. Scan size $10 \times 10~\mu m^2$, line frequency 0,5 Hz. Scan direction from left to right.*

Together with the highest asperities, also the nanoscale particles exhibit a low friction coefficient. This is illustrated by the dark spots in Fig. 4.22a, marked with the white circles. One can see that some of these particles have ended up in the valleys, while others reside in higher regions on the surface. Like the highest asperities, the higher ones are probable to form part of the true contact area and assist in the lubrication process. We assume that, in full analogy with the larger carbon-based particles, investigated in Fig. 4.21, the highest asperities and these nanoscale particles are partially graphitized. Unfortunately, the spot size in our micro-Raman spectroscopy measurements was too large to directly confirm this. The scenario suggested by our observations resembles that of the formation of so-called nanoscrolls, which are thought to have extremely lubricious properties. Berman et al [19] have recently shown that graphene patches can wrap around nanodiamonds. This might significantly lower the sliding friction on DLC, again via the effect of structural lubricity, or superlubricity between graphite surfaces, shown in e.g. [35-37]. Interestingly, some of the low-friction spots if Fig. 4.22a do not correlate with protrusions in Fig. 4.22b. We assume that these are wear sites, where nano-particles have originated under the influence of high shear stresses. Either during the shearing-off process or during subsequent sliding in contact with the opposing surface, these sites may have changed their carbon network structure.

4.4 Summary

Micropatterning of the studied DLC substrates is an essential instrument that helps directly to control an apparent area of contact between the sliding surfaces. As a result, we can observe origin, step-by-step formation and development of third-body elements during the sliding friction on the fixed areas of contact. Our observations suggest that high local stresses lead to the formation of DLC microparticles with increased numbers of sp^2-bonded clusters, which in turn serve as a lubricant. In turn, the microparticles seem later to decompose into nanoparticles, which demonstrate the low friction coefficient too. Adding here the lubrication due to surface transformation at the highest asperities on the DLC, all together it results in lowering of the sliding friction coefficient regardless of the choice of counter sample. We have also shown a correlation between presence and absence of the particle debris from the counter, which take part in the contacting

interface. We suspect that the surface of e.g. Si flakes got wrapped with a thin layer of carbon material transferred from the DLC surface during their initial shear. The last could explain their mobility at the sliding interface. More research is needed to be done on the level of single nano- and microparticles of DLC and counter material in order to relate their surface properties to the low friction coefficient at the macroscopic level they deliver together.

4.5 Bibliography

1. Aksenov, I.I. & Strel'nitskij, V.E. Wear resistance of diamond-like carbon coatings. *Surface and Coatings Technology* **47**, pp. 252-256 (1991)

2. Savvides, N. & Bell, T.J. Hardness and elastic modulus of diamond and diamond-like carbon films. *Thin Solid Films* **228**, pp. 289-292 (1993)

3. Erdemir, A. & Donnet, C. Tribology of diamond-like carbon films: recent progress and future prospects, J. Phys. D: Appl. Phys. **39**, pp. 311-327 (2006)

4. Banerij, A. *et al*. High temperature tribological behavior of W containing diamond-like carbon (DLC) coating against titanium alloys, *Surf. And Coat. Technology* **241**, pp. 93-104 (2014)

5. Yang, B. *et al*. The high temperature tribological properties of Si-DLC films. *Surf. and Interf. Analysis* **13**, pp. 1601-1605 (2012)

6. Erdemir, A. *et al*. Friction and wear performance of diamond like carbon films grown in various source gas plasmas, *Surf. Coat. Technol*. **120-121**, pp. 589-593 (1999)

7. Grill, A.: Diamond-like carbon: state of the art, *Diamond and Related Materials* **8**, pp. 428-434 (1999)

8. Ronkainen *et al*. Friction and wear properties in dry, water- and oil-lubricated DLC against alumina and DLC against steel contacts. *Wear* **222**, pp. 120-128 (1998)

9. Lettington, A. Applications of diamond-like carbon thin films. *Thin Film Diamond* (Elsevier) 1998

10. Wei, Q. *et al*. Mechanical properties of diamond-like carbon composite thin films prepared by pulsed laser deposition. *Composites Part B: Engineering* **30,** 675–684 (1999).

11. Donnet, C. *et* al. The role of hydrogen on the friction mechanism of DLC films. *Tribology Letters* **9**, pp. 137-142 (2000)

12. Eryilmaz, O. L. & Erdemir, A. On the hydrogen lubrication mechanism(s) of DLC films: An imaging TOF-SIMS study. *Surf Coatings Technology* **203**, pp. 750-755 (2008)

13. Hu, L., *et al*. Transformation of sp3 to sp2 sites of diamond like carbon coatings during friction in vacuum and under water vapour environment. *Thin Solid Films* **290**, pp. 126-130 (1996)

14. Marino, M. *et al.* Understanding Run-In Behavior of Diamond-Like Carbon Friction and Preventing Diamond-Like Carbon Wear in Humid Air. *Langmuir* **27**, pp. 12702-12708 (2011).

15. Konicek *et al.* Influence of surface passivation on the friction and wear behavior of ultrananocrystalline diamond and tetrahedral amorphous carbon thin films. *Phys Rev B* **85**, 155448 (2012).

16. Erdemir, A. Genesis of superlow friction and wear in diamondlike carbon films. *Tribology International* **37**, pp. 1005-1012 (2004)

17. Al-Azizi, A. Surface chemistry and Superlubricity of DLC. A Dissertation in Chemical engineering (2016)

18. Hone, J. & Carpick, R. Slippery when dry. *Science* **348**, pp. 1087-1088 (2015)

19. Berman, D. *et al*. Friction. Macroscale superlubricity enabled by graphene nanoscroll formation. *Science* **348**, 1118-22 (2015)

20. Rabinowicz, E. Practical uses of the surface energy criterion Raboniwicz. *Wear* 1964

21. Sutton, D.C. *et al*. The friction of diamond-like carbon coatings in a water environment. *Friction* **1**, pp. 210-221 (2013)

22. Liu, Y. *et al*. An investigation of the relationship between graphitization and frictional behavior of DLC coatings. *Surface and Coatings Technology* **86**, pp. 564-568 (1996)

23. Tai, F.C. *et al*. Multipeak fitting analysis of Raman spectra on DLCH film. *Journal of Raman Spectroscopy* **40**, pp. 1055-1059 (2009)

24. Sadezky, A. Raman microspectroscopy of soot and related carbonaceous materials: Spectral analysis and structural information. *Carbon* **43**, pp. 1731-1742 (2005)

25. Kahn, M. *et al.* Structural and mechanical properties of diamond-like carbon films deposited by an anode layer source. *Thin Solid Films* **517**, pp. 6502-6507 (2009)

26. Casiraghi, C. Raman spectroscopy of hydrogenated amorphous carbons. *Phyicals Review B* **72**, 085401 (2005)

27.   Ferrari, A.C. & Robertson, J. Resonant Raman spectroscopy of disordered, amorphous, and diamondlike carbon. *Phys Rev B* **64**, 075414 (2001)

28.   Kim, D.-W. & Kim, K.-W. Effects of sliding velocity and ambient temperature on the friction and wear of a boundary-lubricated, multi-layered DLC coating. *Wear* **315**, pp. 95-102 (2014)

29.   Scharf, T.W. & Singer, I.L. Quantification of the Thickness of Carbon Transfer Films Using Raman Tribometry. *Tribology Letters* **14**, pp. 137-145 (2003)

30.   Erdemir, A. & Eryilmaz, O. Achieving superlubricity in DLC films by controlling bulk, surface, and tribochemistry. *Friction* **2**, pp. 140-155 (2014)

31.   Rose, F. *et al.* Complete characterization by Raman spectroscopy of the structural properties of thin hydrogenated diamond-like carbon films exposed to rapid thermal annealing. *Journal of Applied Physics* **116**, 123516 (2014)

32.   Romero, P. *et al*. Surface passivation and boundary lubrication of self-mated tetrahedral amorphous carbon asperities under extreme tribological conditions. *Friction* **2**, pp. 123-208 (2014)

33.   Kim, S. *et al.* Effects of Humidity on the Friction Coefficient of Diamond-Like Carbon (DLC) Coating. *Journal of Korean Physical Society* **54**, pp. 2212-2218 (2009)

34.   Brennan, J. *et al*. Adsorption of Water in Activated Carbons: Effects of Pore Blocking and Connectivity. *Langmuir* **18**, pp. 5438-5447 (2002)

35.   Dienwiebel, M. *et al.* Superlubricity of graphite. *Physical Review Letters* **92**, 126101 (2004)

36.   Cihan, E. *et al*. Structural lubricity under ambient conditions. *Nature Communications* **7**, 12055 (2016)

37.   Feng, X. *et al*. Superlubric Sliding of Graphene Nanoflakes on Graphene. *ACS Nano* **7**, pp. 1718-1724 (2013)

38.   Irmer, G. & Dorner-Risel, A. Micro-Raman studies on DLC. *Advanced Engineering Materials* **7**, pp. 694-705 (2005)

39.   Hong, S.-H. & Winter, J. Micro-Raman spectroscopy on a-C:H nanoparticles. *Journal of Applied Physics* **98**, 124304 (2005)

40.   Ahn, H.-S. *et al.* Application of phase contrast imaging atomic force microscopy to tribofilms on DLC coatings. *Wear* **249**, pp. 617-625 (2001)

41. Hansma, H. *et al.* Properties of biomolecules measured from atomic force microscope images: a review. *Journal of structural biology* **119**, pp. 99-108 (1997)

42. Butt, H.-J. *et al*. Force measurements with the atomic force microscope: technique, interpretation and applications. *Surface Science Reports* **59**, pp. 1-152 (2005)

43. Haugstad, G. & Jones, R. Mechanisms of dynamic force microscopy on polyvinyl alcohol: region-specific non-contact and intermittent contact regimes. *Ultramicroscopy* **76**, pp. 77-86 (1999)

44. Cook, R.F. Strength and sharp contact fracture of silicon. *Journal of Materail Science* **41**, pp. 841-872 (2006)

45. Gustavsson, F. Formation of tribologically beneficial layer on counter surface with smart chemical design of DLC coating in fuel contact. *Tribology - Materials, Surfaces & Interfaces* **6** (2013)

46. Gayathri, S. *et* al. Impact of laser power density on tribological properties of Pulsed Laser Deposited DLC films. *AIP Advances* **3**, 122113 (2013)

47. Zhao, F. Structural, mechanical and tribological characterizations of a-C:H:Si films prepared by a hybrid PECVD and sputtering technique. *Journal of Applied* Physics **42**, 165407 (2009)

48. Si-mat.com/silicon-wafers.html Visited on 05 April 2017

49. Williams, R. & Goodman, A.M. Wetting of thin layers of Si_2O by water. *Applied Physics Letters* **25**, 531 (1974)

50. Ni, W. *et al*. Tribological behavior of diamond-like-carbon (DLC) coatings against aluminum alloys at elevated temperatures. *Surface & Coatings Technology* **201**, pp. 277-283 (2006)

51. Enachescu, M. *et al.* Atomic Force Microscopy Study of a Ideally Hard Contact: The Diamond(111)/Tungsten Carbide Interface. *Physical Review Letters* **88**, pp. 1877-1879 (1998)

52. Li, H. *et al*. Humidity dependence on the friction and wear behavior of diamond-like carbon film in air and nitrogen environments. *Diamond & Related Materials* **15**, pp. 1585-1592 (2006)

53. Song, J. *et al.* Penetration depth at various Raman excitation wavelengths and stress model for Raman spectrum in biaxially-strained Si. *Science China Physics, Mechanics and Astronomy* **56**, pp. 2065-2070 (2013)

54.   Kumar, N. *et* al. Super-low to high friction of turbostratic graphite under various atmospheric test conditions. *Tribology International* **44**, pp. 1969-1978 (2011)

55.   https://www.vaisala.com/ Visited on 09 April 2017

Chapter 5

Dynamic and static tribological properties of micropatterned DLC under different humidities

5.1 Introduction

Sliding friction occurs in a large number of technological processes and in everyday life [7]. Developing a deep understanding of its mechanisms is important in our search for ways to control or minimize friction and wear between sliding surfaces. In this Chapter we focus on sliding friction when one of the two surfaces has a hydrogenated DLC coating. In order to define the precise regions where the DLC coating makes mechanical contact, we micropatterned our DLC-coated samples with cylindrical mesas, similar to the ones discussed in Chapter 4. In Chapter 5, we concentrate on the dependence of friction on two parameters, namely the sliding velocity and the humidity of the air.

Sliding friction is usually considered to be independent of velocity. Charles Coulomb (1736-1806) postulated this in his law of dry friction, stating that "when two solid bodies are in contact, the force required to produce sliding between them is proportional to the normal force acting in the plane of contacts" [37]. In mathematical terms,

$$F_f = \mu_d F_N,$$

(5.1)

where F_f is friction force, F_N is the normal load and μ_d is the coefficient of sliding, or dynamic friction. Indeed, in this so-called Amontons-Coulomb law [77], F_f does not depend on sliding velocity. However, over the past decades, careful studies demonstrated that friction does depend on sliding velocity and that this law oversimplifies the interaction between the sliding objects [31, 32, 38, 39]. Both on the nano- and on the macroscale, certain materials exhibit a decrease of the coefficient of friction with increasing velocity [6,34,35]. Other materials, on the other hand, show an increase [31-34], while there are also materials for which the friction coefficient varies non-monotonically with velocity [32,35,40]. A near velocity-independence was demonstrated for an AFM tip sliding over amorphous carbon, diamond and HOPG surfaces [41]. The differences in behavior derive from different material properties, in particular from differences in the structure and composition of the surfaces and their interaction with the environment. Effects that play a role are for example the aging of contacts [46,42,44], plastic and elastic shear of asperities [43,45,47], hydrodynamic effects such as the viscous behavior of

adsorbed water necks and lubrication layers [14,23,40,48], and tribochemical effects [e.g. 35]. It has also been shown that even at room temperature, capillary condensation of adsorbed water between e.g. a metal tip and a graphite surface can lead to the formation of ice, which significantly increases the friction force between them at low velocities [24, 25].

Friction phenomena on DLC are also complex. First of all, they should be always described as a three-body contact problem. A third-body is not only a layer of particle debris and other wear products created during sliding between the contacting surfaces, but it can also be adsorbed vapor [1, 63]. Depending on the surface and interfacial energies, capillary bridges can be created between surfaces that are either in contact or close to contact [3-6, 22]. Viscous shear of capillaries can dramatically alter the friction and wear properties both on the nano- [6, 13, 14, 23] and on the macroscale [8-12]. Depending on hydrophilicity of the surfaces and their roughness, the friction force can display either increasing or decreasing behavior as a function of e.g. sliding speed and relative humidity [16-21]. However, at present there is still much controversy on the general effects of velocity and relative humidity on friction properties of DLC coatings.

In this study, we consider how particle debris formed during the run-in period plays a major role in the lubrication of the interface between a sliding object and the DLC surface. In this context, we also take into account the influence of capillary forces acting between them [2, 15]. Tribochemical reactions on the DLC might affect the friction coefficient differently under different atmospheric conditions [11, 14, 26-28]. Here, we discuss experiments on the sliding-velocity-dependence and the aging of contacts at different levels of relative humidity on micropatterned samples with a-C:H DLC coatings.

5.2 Experimental

The experimental details were thoroughly discussed already in Chapter 4. In summary, Dylyn a-C:H DLC coatings were applied by means of magnetron sputter deposition on pre-polished SiSiC substrates. On the coated surfaces, we measured a contact angle for water of 85°, so our particular DLC coating should be considered partially hydrophobic.

Our friction measurements were performed with a Bruker Universal Mechanical Tester (UMT), described in detail in Chapter 4. The role of the counter-surface was played by a 2-inch diameter silicon wafer, $250\ \mu m$ thick. The weight of each wafer of approximately $12\ mN$ served as the normal force in the sliding experiments. The contact angle of water with the wafer, covered with its native oxide SiO₂, was measured to be 36° (strongly hydrophilic). The wafers were used directly from the supplier [76], where they had been pre-packed under cleanroom conditions, so that no further cleaning was needed, prior to the experiments.

In our experiments, the relative humidity (RH) was measured close to the substrate position with a hygrometer, Vaisala HM40 [78]. The RH value could be varied between 1.5 and 90% (at room temperature, $22°C$) by means of a flow of a controlled mixture of dry nitrogen and humid air through the microscope chamber.

5.3   Experimental results

Figure 5.1 shows the result of the measurement of the dependence of the coefficient of friction on sliding velocity. Prior to the test, the DLC-coated substrate was 'run-in' against a silicon wafer, until the COF had settled at a low value of 0.08 (described in detail in Chapter 4). The measurements were performed under three different levels of RH: 1.7% (dry), 35% ('regular') and 88% (humid). The sliding velocity of the silicon wafer with respect to the DLC-coated substrate was gradually varied over a wide range, from $200\ nm/sec$ to $1\ mm/sec$ ($1\ \mu m/sec \div 2\ mm/sec$ in the case of $RH = 1.7\%$). The maximum driving velocity of $2\ mm/sec$ of the UMT was set by its limited stroke length. The minimum driving velocity was limited by the minimal step of the rotary drive, and was equal to $100\ nm/sec$. For each set of measurements over a range of velocities at the given RH a new silicon

wafer was used. For each combination of humidity and velocity, three measurements were performed along the same stroke direction and the average value of COF was calculated. Thus, a typical error margin for each data point is about 2% of its average value. The COF-values determined at dry conditions ($RH = 1.7\%$) show a nearly logarithmic dependence on velocity over the full velocity range. At higher RH levels, the low-velocity data points deviate from the logarithmic behavior (marked with ovals in Fig. 2.1). For $RH = 35\%$, a minor deviation is observed in the range of $200\ nm/sec$ to $5\ \mu m/sec$, while the COF is almost constant at $RH = 88\%$ between $200\ nm/sec$ and $20\ \mu m/sec$. A logarithmic increase of the friction coefficient with the sliding velocity is in qualitative agreement with friction studies between partially hydrophobic surfaces and the hydrophilic native oxide of silicon [6, 33].
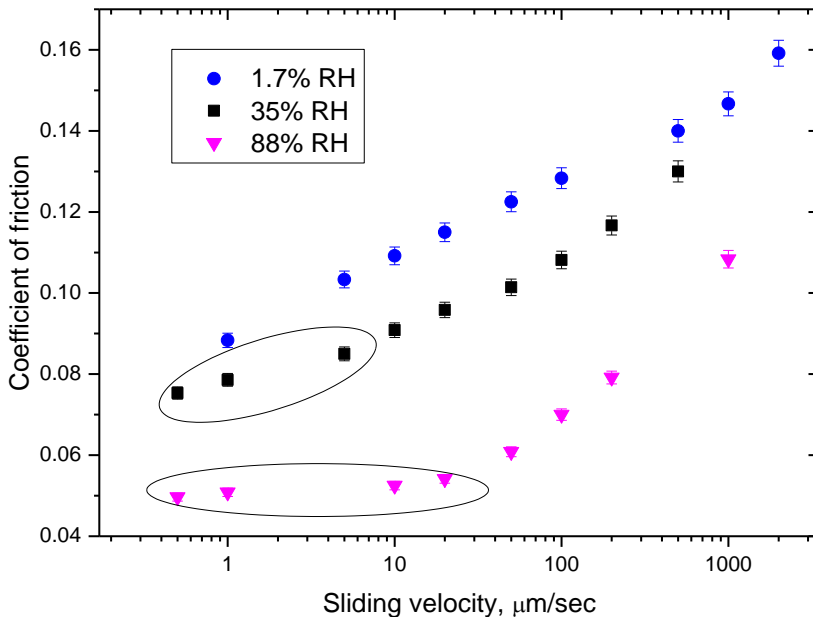
Figure 5.1. Dynamic coefficient of friction as a function of sliding velocity between silicon wafers and a DLC-coated SiSiC substrate. Measurements were carried out at three different humidity levels, RH = 1.7%, 35% and 88%. The normal load of 12 mN was fixed by the weight of the wafers.

As Figure 2.1 shows, the frictional behavior of the DLC/SiO$_2$ interface appears to be rather sensitive to the RH level. To explore this in more detail, we carried out a series of measurements at certain constant velocities as a function of RH. Figure 5.2 shows the dynamic COF versus RH at 1 µm/sec, 10 µm/sec and 100 µm/sec. For each velocity, a series of measurements was performed while we gradually made RH increase from 2% to 90% and then made it reduce back to 35%. Each data point in Figure 5.2 represents the average value of three consecutive measurements at the same combination of velocity and RH level. No hysteresis was observed between the measured values of the friction coefficient upon the gradual increase or decrease of RH. The corresponding curves are plotted on a logarithmic RH-scale in order to emphasize the 'abruptness' of the reduction in COF at higher RH-values for all three velocities. This occurs around $RH = 55\%$, independent of the velocity. For each velocity, the COF is high and almost constant at RH levels below this value.
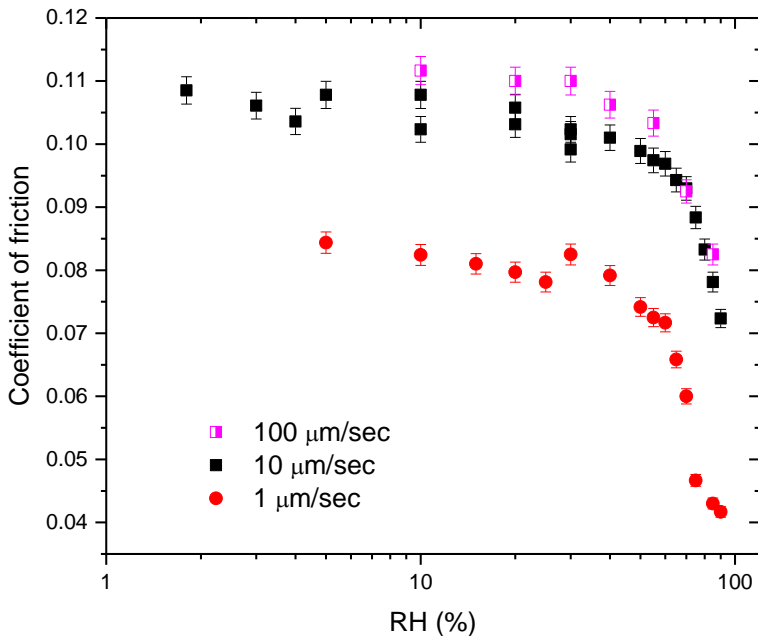
Figure 5.2. Dependence of the dynamic COF between silicon wafers and a DLC-coated SiSiC substrate on the relative humidity RH at three different sliding velocities.

Another sensitive quantity that we can determine in our experiments is the static friction coefficient μ_s, which is defined as the ratio between the minimum tangential force $F_s = \mu_s F_N$ one needs to apply in order to initiate the relative sliding of two objects and the normal force F_N between them. Usually $\mu_s > \mu_d$ (Fig. 5.3). For various materials μ_s increases quasi-logarithmically with the 'age' of the static contact τ prior to sliding $\mu_s(\tau) \approx \mu_s^0 + \beta_s \ln(\tau)$, where β_s is a coefficient specific for contacting materials and temperature, and μ_s^0 is the static threshhold base value [43].
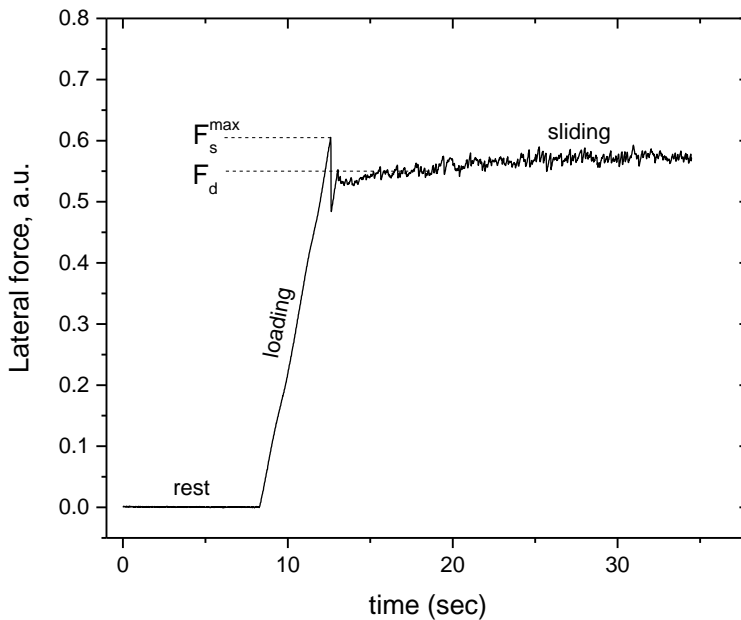
Figure 5.3. An example of the lateral force between two solid surfaces, in this case a Si wafer sliding over a DLC surface (Chapter 4), as a function of time at the beginning of a sliding experiment. After an initial period, during which no lateral force is exerted on the contact (rest), a lateral force is accumulated (loading). When this exceeds the static threshold level $F_s^{max} = \mu_s F_n$, sliding starts, after which the lateral force reduces to the dynamic value of $F_d = \mu_d F_n$. Note, that in the example shown here, the system goes through one additional stick-slip cycle before truly steady sliding sets in.

Figure 5.4 represents the dependence of the static coefficient of friction μ_s on contact aging time, i.e. the time spent by the silicon wafer in rest on the micropatterned DLC substrate, prior to sliding. These measurements of the static

COF were carried out at three different RH levels, 0.66%, 35% and 90%. During the dwell time, the pusher of the UMT always remained engaged with the silicon wafer (arrested contact), while the lateral force was measured to decrease slowly in time due to relaxation at the interface, before reaching a certain constant equilibrium value [e.g. 47]. After this dwell time, the pusher was put into motion at a velocity of 20 $\mu m/sec$, which made the lateral force increase at a rate of 1.5 mN/sec to the static lateral force maximum F_s^{max}. At this point the silicon wafer would be set into motion, which would make the lateral force reduce to the dynamic friction force level F_d. For each μ_s value in Fig. 5.4, we used the average of three measurements of F_s^{max}.

Over the explored range of aging times $1 \leq \tau \leq 500\ s$, in Figure 5.4, the data at the lower two RH-values show a weak logarithmic dependence of the static COF. Whereas μ_s decreases under dry conditions, for $RH = 0.66\%$ (the fit is for $\mu_s = 0.11 - 2.91 \times 10^{-4} ln(\tau)$, with τ expressed in seconds), it increases at $RH = 35\%$ (the fit is for $\mu_s = 0.10 + 7.76 \times 10^{-4} ln(\tau)$). Under very humid conditions (RH = 90%), μ_s is found to increase logarithmically with the aging time only above approximately 20 sec (marked as II in Fig. 5.4). For shorter aging times (below 20 sec, marked as I), we find only a very modest slope of the logarithmic increase of μ_s.
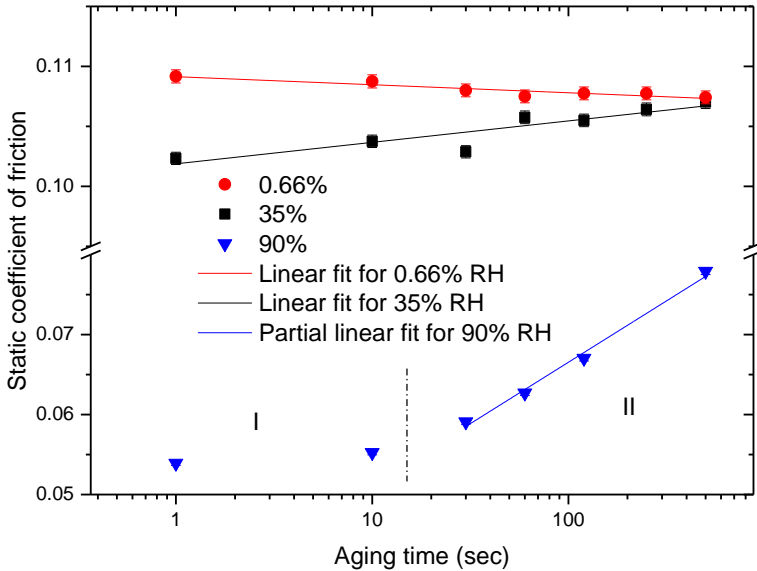
Figure 5.4. Dependence of static friction coefficient on contact aging time τ at three different values of RH, for silicon wafers on DLC-coated SiSiC substrates. The normal force of $12\ mN$ was set by the weight of the wafers. The static force maximum was measured at a rate of lateral force increase of $1.5\ mN/s$.

5.4 Discussion

Opposite to our observations, many other studies have found an increase in friction of a-C:H DLC with increasing humidity [e.g. 18, 52, 58, 59, 75]. Only a modest number of papers report a decrease, similar to our findings for hydrogenated DLC films [81, 64, 57]. Most studies agree that under dry conditions a-C:H films remain largely inert [27]. The presence of hydrogen leads to extremely weak adhesion [29, 30] in interfaces that involve hydrogenated DLC films, so that extremely low friction coefficients can be achieved [82]. Hydrogen added to the DLC film can saturate the dangling σ-bonds of carbon atoms [18]. Similarly, it can suppress the number of C=C double bonds (particularly π-π* interactions). However, when the DLC-lubricated contacts are exposed to high humidity levels, in many cases the friction properties exhibit significant changes. Often, for $RH > 40\%$, the friction coefficient and the wear rate are found to rapidly grow. Most of these observations can be associated with tribochemical oxidation of DLC

films during the friction process at elevated humidity. Based on X-ray photoelectron spectroscopy analysis (XPS), Li et al. [58] proposed a model to explain the transformation of initially chemically inert hydrogenated DLC into an oxygen-containing surface. They suggest that the increased adsorption rate of water molecules on the DLC surface at high humidities increases the probability of water chemisorption at the surface sites were C-H bonds are mechanically broken by the high shear stresses that develop locally during sliding. As a consequence, C-OH and C-O groups may be formed. Further breaking of C-H bonds will provide the electrons required to form C=O on the DLC surface, which leads to the accumulation of a thin oxide layer on the contacting elements. In turn, this leads to a rapid increase of the friction coefficient. On top of this, water can adsorb on the oxide surface, introducing strong dipole interactions that increase the adhesive forces between the sliding surfaces [28].

In our study, the DLC coatings show the highest dynamic (sliding) friction coefficient $\mu_d = 0.11$ at high velocities under dry conditions ($RH = 1\%$) and reach the lowest value $\mu_d = 0.04$ at low velocities under humid conditions ($RH = 90\%$). A significant lowering of the friction coefficient is observed at $RH = 55\% \pm 4\%$ (Fig. 5.2). In our study, the measurements carried out at different RH values and at different velocities were completely reversible, i.e. the accompanying changes in the COF were instantaneous and free of hysteresis. This strongly suggests that in our case the interaction of the coating with water vapor has a purely *physical* adsorption character, rather than involving water-induced chemical changes in the coating that would be necessarily accompanied with an intrinsic timescale and a hysteretic tendency. Even though the chemical composition of our hydrogenated DLC coatings is very similar to that of DLC coatings for which friction measurements have been reported before in the literature [17, 18, 27, 57], our observations show systematic differences. These must find their origin in other differences in our experimental setting, in particular in our special flat-disk-on-rough-mesas contact geometry, and in our combination of modest sliding velocities and a relatively low normal load. By contrast, most of experiments in this field are conducted with balls and pins sliding over DLC-coated substrates under conditions that are relevant for the automotive industry: high normal loads and high velocities. Also the typical sliding distances in most experiments are relatively large. Hence the surface of the sliding ball or pin may be in contact at each stage of

the sliding process not only with parts of the transfer layer [21 and 83], but also with fresh parts of the DLC surface, which could make the interface sensitive to the chemical, e.g. oxidation state of the DLC surface.

We used micropatterned DLC substrates in combination with flat silicon wafers as the counter-surface. Similar to other studies, we find a clear correlation between the presence of third-body C-based particles on the DLC film, and the reduction of the dynamic friction coefficients [e.g. 60]. As we demonstrated with our Raman spectroscopy measurements (Chapter 4), these particles (and some asperities) have a short-range disordered microstructure, similar to that of disordered graphite. Our flat-on-rough-mesa interface geometry guarantees that the highest protrusions on the DLC-surface, which are either asperities on the DLC-coating itself or high-lying third-body particles, remain in continuous direct mechanical contact with the flat silicon counter-surface, more or less independently of the sliding velocity and the humidity. This is very different from the more common rough-on-rough situation, in which each local contact has a typical 'lifetime' that is determined by the ratio between its size and the sliding velocity. In our situation, the contacts are 'fixed' and their lifetime is practically infinite! Obviously, this may have distinct implications for the dependence of the friction force on velocity and on humidity.

First, at the beginning of sliding, the decomposed loose particles reduce friction due to weak van der Waals interaction, thus low adhesion, between their hydrogen terminated surfaces. Here we assume that a water film is adsorbed on the hydrophilic native silicon oxide surface and that this water film reduces friction by keeping the surfaces out of direct mechanical contact. As sliding proceeds, more and more C-H bonds on the particles rupture. This happens under the high contact pressure, the high shear stresses and the generation of thermal energy during sliding. This leads to the thermally activated release of H atoms and, hence, the rapid decrease of the total hydrogen content in each particle and its (partial) graphitization [57, 63]. As a result, the particles and other sp^2-modified areas will develop micro-ordered low-energy surfaces [62]. Whereas these surfaces can be extremely slippery, the dangling bonds (free σ-bonds) at the edges of the newly created sp^2 clusters can engage in new bonds that lead to pinning of the clusters and pinning of the water that is sliding over them. When the humidity is not too low, the dangling bonds are re-passivated with H-atoms and OH-groups,

originating from water molecules that dissociate at the reactive edges [79, 80]. At high enough humidity, water will form an adsorbed layer that separates the contacting surfaces and thus acts as a lubricant [49, 61]. A similar water lubrication action is associated with non-hydrogenated DLC [51, 64]. We also cannot exclude the possible oxidation of the DLC film at higher humidity, as was reported in [58]. On the other hand, if an oxide layer was formed on the DLC surface, this should result in a new run-in phase of the DLC, thus increase of the friction coefficient [17]. Our observations do not provide strong arguments in favor of the formation of an oxide layer on our DLC layers, because the friction coefficients measured in this study were completely reversible with respect to changes in RH.

In addition to the lubrication of sp^2 clusters, water can also play other roles. Firstly, pristine hydrogenated DLC has partially hydrophobic properties and its friction behavior is almost independent of RH [13]. At the same time, the first monolayer of water molecules that are strongly bonded to the silicon counter-surface are not likely to be pressed out of the contact [23, 33, 34]. Instead, the water film will be sheared across the DLC surface during sliding, again keeping the surfaces out of direct mechanical contact. Secondly, the graphitization of particles and the contacting asperities on the DLC coating leads to the existence of hydrophilic 'islands'. Therefore, we expect these crucial regions on the DLC side to engage in capillary effects. The viscoelasticity of the confined water in the capillary bridges between these regions and the silicon surface may affect both the dynamic and the static friction behavior [6, 13, 32, 33]. We can only conclude that, depending on the history of the sliding contact and the conditions under which a sliding experiment is conducted, each individual experiment may display its own combination of lubricating and pinning properties of water. An artist impression that captures some of this complexity of the interface between a rough DLC substrate and an oxide-covered, smooth silicon wafer, in the presence of wear particles and in a humid atmosphere, is presented in Fig. 5.5.
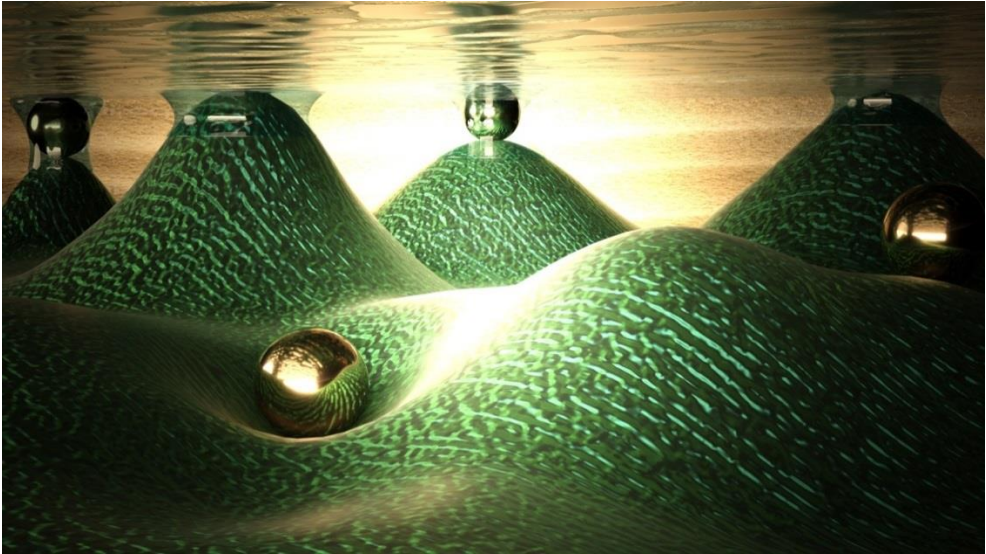
Figure 5.5. Artist impression of the interface between a rough DLC coating (bottom surface) and a smooth, oxide-covered silicon wafer (top surface) in a humid atmosphere. For simplicity, the third-body particles that have been formed during the run-in phase of the contact, are presented as spherical objects. We distinguish two types of contacts, namely direct contacts between the DLC and the wafer and contacts via one of the particles. Both types are decorated by capillary water bridges.

In Fig. 5.2 we showed how the dynamic friction coefficient μ_d varies with humidity at three fixed velocities. For example, at a velocity of $1 \, \mu m/sec$, μ_d has values as low as 0.05 at $RH = 80\%$ and as high as 0.09 at $RH = 1.7\%$. The corresponding friction force curves (Fig. 5.6), also show a qualitative difference in the sliding behavior. We observe that at the lower humidity the friction exhibits much stronger variations than at higher humidities. At higher RH, a modest, stick-slip-like periodicity is visible. Also the initial sliding behavior differs. The curves for low- and medium-RH in Fig. 5.6 start almost at the same lateral force of $0.95 \, mN$. This is mainly due to the minor difference between the static coefficient of friction at low-RH and medium-RH (Fig. 5.2). Moreover, the waiting time prior to the actual pushing and measurement in the both cases was longer than $300 \, sec$. Such waiting time is necessary for stabilization of RH in the test chamber. It is only after sliding over a distance in the order of $10 \, \mu m$, that the humidity-dependent differences are fully established.

In an attempt to explain the curves in Fig. 5.6, we first concentrate on the low-RH data. The noise on the lateral force at $RH = 1.7\%$ suggests that the contact geometry is not completely stationary. This could mean that the third bodies are translated over the DLC surface under the influence of the shear forces that they experience [33, 42 and 47]. It is not surprising that this situation leads to stronger energy dissipation, hence higher friction levels [32]. The absence of this effect at somewhat higher RH-levels could be due to the presence of capillary bridges that connect these particles to the DLC substrate, in spite of the fact that neither the substrate nor the particles are fully hydrophilic. As we have already seen in Fig. 2.2, almost independently of the sliding velocity, water starts to significantly lubricate the surface at an RH-level around 55%. This is in good agreement with the known adsorption kinetics of water on graphitic materials [49, 50 and 84]. The buildup of water between the DLC (third bodies and asperities) and the silicon would then explain the dramatic lowering of the friction between $RH = 35\%$ and 80%.
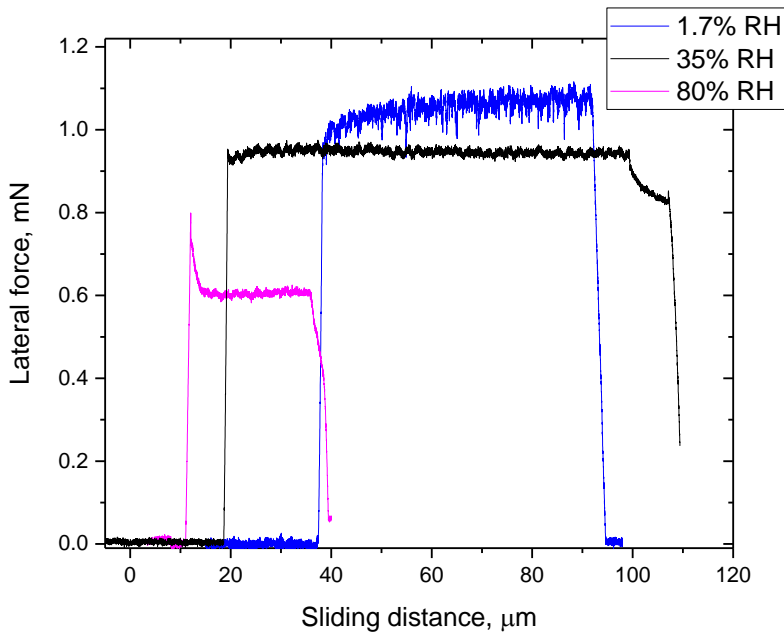
Figure 5.6. Lateral forces measured between a DLC-coated SiSiC substrate and a silicon wafer in three sliding traces at a fixed velocity of 1 μm/sec *at RH-values of* 1.7%, 35% *and* 80%. *The normal load was* 12 mN *in all three cases. The horizontal axis indicates the lateral position of the push bar; the precise starting point of the actual sliding motion of the silicon wafer was different for every curve.*

We now revisit the measured dynamic (Fig. 5.1) and static (Fig 5.4) friction coefficients in an attempt to make a direct comparison between the two. A natural way in which the two are often related is via the average lifetime of microcontacts, which equals the ratio between the average diameter of microcontacts and the sliding velocity [47]. For those phenomena that are a function of contact time, such as capillary condensation over existing contacts and near-contacts or elastic and plastic creep, this average contact lifetime then plays a similar role as the waiting time does for static friction. With respect to the microcontact lifetimes, the situation in our experiments seems fundamentally different. The lifetime of our microcontacts is extremely long as a direct consequence of the geometry of our experiments, in which one of the two contacting bodies, the silicon wafer, is nearly perfectly flat. However, when the third bodies on the DLC side can move, as we

have argued for the low-RH data in Fig. 5.6, the arrangement of microcontacts is no longer stationary and a new type of lifetime is introduced.

In our experiments, the details of the measurement technique introduce a direct link between static and dynamic friction measurements. The driver motor that is used in our UMT to generate the sliding motion is a linear stepper motor. On the microscale, its motion is not continuous but is composed of periodic translations, the minimum step size being $100\,nm$, separated by stationary intervals. Therefore, we can interpret our dynamic friction measurements as measurements of the static friction force after a short waiting time. This allows us to combine the data in the two graphs of Figs. 5.1 and 5.4 into a single one, in which we can express the control parameter either in terms of the effective sliding velocity or the effective waiting time. The result of this combination is shown in Fig. 5.7.
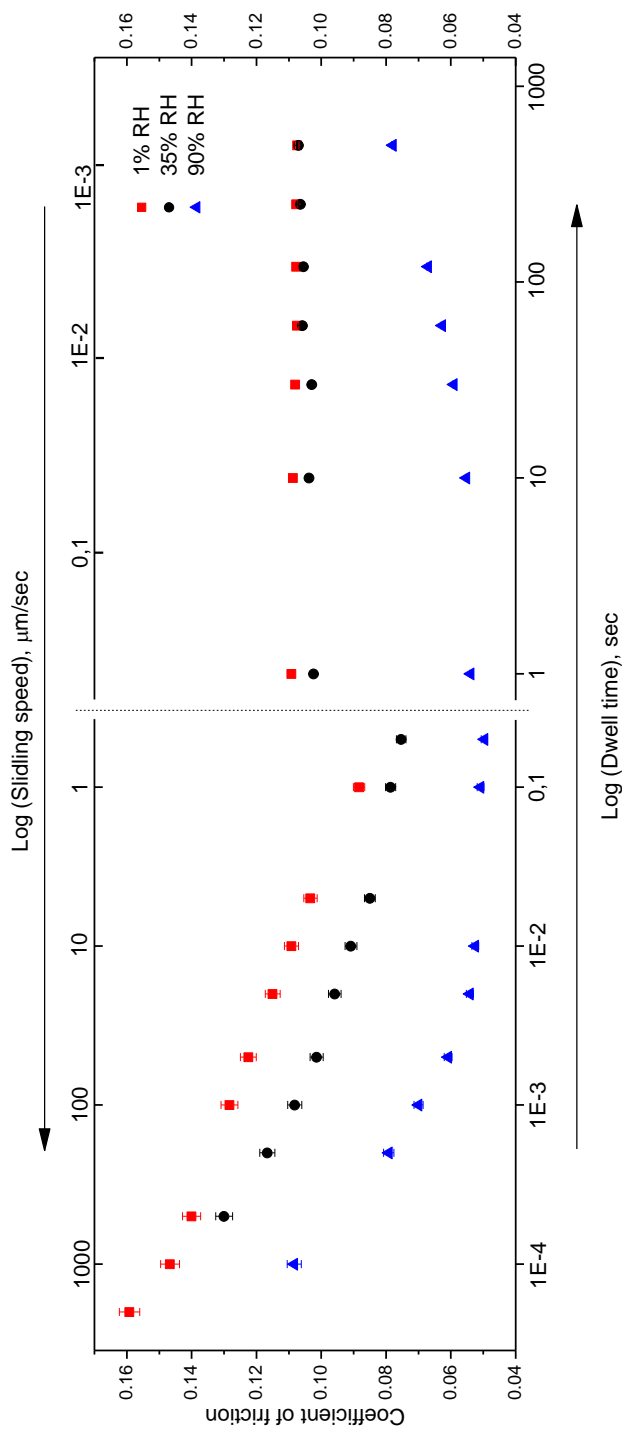
Figure 5.7. Combined representation of measured coefficients of friction, expressed as a function of sliding velocity and waiting time, based on the μ_d-data from Fig. 5.1 and the μ_s-data from Fig. 5.4. The vertical dashed line points where the data from Fig. 5.1 and Fig. 5.4 merge.

Figure 5.7 shows that at all three RH levels, the friction force decreases with increasing waiting time (or decreasing sliding velocity) up to a transition point around a waiting time of $1\ sec$. For the lower two humidities of $RH = 1\%$ and 35%, μ_d remains nearly constant for all waiting times longer than $1\ sec$. For the higher humidity of 90%, we find that longer waiting times lead to increasing μ_d values. As already discussed in relation to the friction curves in Fig. 5.6, we interpret the low- and medium-RH data in terms of the sliding-induced translation of third bodies over the DLC substrate. In this interpretation, capillary condensation serves to attach the third bodies to the DLC, which progressively fails at shorter waiting times and lower humidities [6, 55, 65-67]. The factor 35 between the lower two RH-values corresponds with the roughly equally large ratio between the timescales of the friction data in Fig. 5.7 for 1% and 35% humidity, completely in support of this scenario. A similar scaling can only account for part of the difference between the 90% data and those at the lower two humidities of 35% and 1%. What this scenario also fails to explain is the marked increase of friction at $RH = 90\%$ for longer waiting times.

In wet environments, such as $RH = 90\%$, water menisci nucleate from water vapor between the DLC substrate, with its asperities and nanoscale third-body particles, and the silicon wafer (Fig. 5.5). This nucleation process should occur on a very short time. The typical timescale for the condensation of one layer of water molecules at room temperature and at a humidity of $RH = 65\%$ is an estimate of $25\ \mu s$ [6]. Therefore, we should expect that only a limited number of DLC-silicon contacts is decorated with a condensate, when the waiting time is short [68]. The geometry and size of each fully established capillary neck is dictated by the Kelvin relation [70]. When the waiting time is increased, the number of capillary bridges and, hence, the total water-decorated area will increase. A detailed discussion of the kinetics of the formation of capillary bridges can be found in e.g. [55, 68]. Liquid bridges introduce significant adhesion and thereby reduce the mobility of the third-body particles between the sliding surfaces in humid air. When the sliding velocity is increased, the capillary bridges will be increasingly sheared and even fully developed bridges may not remain intact. The shearing of the capillary bridges may be accompanied by the repeated breaking or melting of crystallized water layers inside the capillaries, as ice is known to form at low sliding speeds, even at room temperature [24]. When a capillary bridge is destroyed, a new one

cannot be formed immediately to replace it, because of the nucleation barrier that is involved in the start of a new capillary bridge [6, 71]. Around a certain critical sliding velocity v_c, the effective size of the sheared capillaries is optimally reduced by the sliding motion for them to minimize the viscous contribution to the friction force, while maintaining the beneficial effect of the water in binding the third-body particles to the DLC. This results in a plateau of low friction around $v_c = 1\ \mu m/sec$ at $RH = 90\%$ and a narrow minimum at the same velocity for $RH = 35\%$ and $RH = 1\%$, as shown at Fig. 5.7.

Finally, we note that the friction at the nanoscale contacts could be affected by thermal activation, similar to what has been reported for the low-friction sliding of FFM tips over surfaces [56, 72,74], and what was one of our motivations for manufacturing the nanopillar structures of Chapter 3. At sufficiently low velocities, thermal fluctuations can assist the tip in overcoming the energy barriers that separates it from the neighboring energy minima in its interaction with the surface over which it is sliding. This phenomenon is called thermolubricity. At higher sliding velocities, less time is available for this role of thermal fluctuations, which renders this effect less successful and makes the friction force an increasing function of velocity. All experiments in this chapter were performed at room temperature. More experiments are currently underway to explore the influence of temperature on friction properties of the investigated DLC-silicon interface. We expect that elevated temperatures can strongly influence the friction coefficient not only through thermolubricity, but possibly also via thermally activated water desorption from the contact areas [14] and thermally activated rupture of contacts due to their spontaneous unbinding [53].

5.5 Conclusions

We have shown that the friction properties of hydrogenated DLC coatings in dry and humid environments are surprisingly different from common tribological behavior of this type of coatings. We ascribe this difference largely to the unusual geometry of our experiment; in our measurements, most microcontacts do not leave the actual sliding interface, which is due to the combination of the micropatterned DLC substrate and the flat, silicon counter-surface. This geometry accelerates the run-in process and assists the DLC-induced lubrication. In the first

part of this chapter, we have shown that the run-in leads to two types of modification of the DLC surface, namely the accumulation of carbon-based third bodies and a bonding reconfiguration of these wear particles and of the asperities of the DLC; both exhibit a change from sp^3 to sp^2 bonding character, i.e. from diamond-like to graphite-like. Here we have further shown that water adsorbed from a mildly humid environment can play a lubricating role for the graphitized DLC clusters at low sliding velocities, which we associate with capillary condensation of water between them and their DLC substrate. At high humidities, friction is lowered even further, suggesting a hydrodynamic contribution, i.e. water acting directly as a lubricant, for example due to the formation of capillary bridges between the oxidized silicon surface and the surfaces of the graphitized DLC particles and DLC asperities.

5.6 Bibliography

1.   Auroux, A. Calorimetry and thermal methods in catalysis. *Springer-Verlag*, Berlin (2013)

2.   Dörmann, M. & Schmid, H.-J. Simulation of Capillary Bridges between Particles. *Procedia Engineering* **102**, pp. 14-23 (2015)

3.   van Honschoten, T. *et al*. The profile of a capillary liquid bridge between solid surfaces. *American Journal of Physics* **78**, pp. 277-286 (2010)

4.   Landau, L.D. and Lifschitz, E.M. Fluid Mechanics, 2nd ed. Butterworth Heineman, Oxford (1971)

5.   Petkov, P. & Radoev, B. Statics and dynamics of capillary bridges. *Colloids and Surfaces A: Physicochemical and Engineering Aspects* **460**, pp. 18-27 (2014)

6.   Riedo, E., Lévy, F. & Brune, H. Kinetics of Capillary Condensation in Nanoscopic Sliding Friction. *Physical Review Letters* **88**, 185505 (2002)

7.   Persson, B. & Spencer, N. Sliding Friction: Physical Principles and Applications. *Physics Today* **52**, pp. 66-68 (1999)

8.   Lancaster, J.K. A review of the influence of environmental humidity and water on friction, lubrication and wear. *Tribology International* **23**, pp. 371-389 (1990)

9.   Klaffke, D. On the repeatability of friction and wear results and on the influence of humidity in oscillating sliding tests of steel-steel pairings. *Wear* **189**, pp. 117-121 (1995)

10.   Ronkainen, H. *et al*. Friction and wear properties in dry, water- and oil-lubricated DLC against alumina and DLC against steel contacts. *Wear* **222**, pp. 120-128 (1998)

11.   Eriksson, A. *et al*. A study of the influence of humidity on the friction and squeal generation of automotive brake pads. *Journal of Automobile Engineering* **215**, pp. 329-342 (2001)

12.   Lee, W. *et al*. The influence of humidity on the sliding friction of brake friction material. *Wear* **302**, pp. 1397-1403 (2013)

13.   Lee, M., Kim, B., Kim, J. & Jhe, W. Noncontact friction via capillary shear interaction at nanoscale. *Nature Communications* **6**, 7359 (2015)

14. Greiner, C., Felts, J., Dai, Z., King, W. & Carpick, R. Controlling nanoscale friction through the competition between capillary adsorption and thermally activated sliding. *ACS Nano* **6**, pp. 4305-4313 (2012)

15. Chau, A., Rignier, S., Delchambre, A. & Lambert, P. Three-dimensional model for capillary nanobridges and capillary forces. *Modelling and Simulation in Materials Science and Engineering* **15**, pp. 305-317 (2007)

16. Kim, S. *et al.* Effects of Humidity on the Friction Coefficient of Diamond-Like Carbon (DLC) Coating. *Journal of Korean Physical Society* **54**, pp. 2212-2218 (2009)

17. Marino, M. *et al.* Understanding Run-In Behavior of Diamond-Like Carbon Friction and Preventing Diamond-Like Carbon Wear in Humid Air. *Langmuir* **27**, pp. 12702-12708 (2011)

18. Erdemir, A. & Donnet, C. Tribology of diamond-like carbon films: recent progress and future prospects. *J Phys D Appl Phys* **39**, pp. 311-327 (2006)

19. Arcifa, A., Rossi, A., Espinosa-Marzal, R. & Spencer, N. Influence of Environmental Humidity on the Wear and Friction of a Silica/Silicon Tribopair Lubricated with a Hydrophilic Ionic Liquid. *ACS Applied Materials & Interfaces* **8**, pp. 2961-2973 (2016)

20. Rhee, T. H., Shin, M. W. & Jang. Effects of humidity and substrate hydrophilicity on nanoscale friction. *Tribology International* **94**, pp. 234-239 (2016)

21. Sirghi, L. Effect of capillary-condensed water on the dynamic friction force at nanoasperity contacts. *Applied Physics Letters* **82**, 3755 (2003)

22. Fogden, A. & White, L.R. Contact elasticity in the precense of capillary condensation. *Jounal of Colloidal and Interface Science* **138**, pp. 414-430 (1990)

23. Gee, M., McGuiggan, P., Israelachvili, J. & Homola, A. Liquid to solidlike transitions of molecularly thin films under shear. *The Journal of Chemical Physics* **93**, 1895 (1990)

24. Jinesh, K.B. & Frenken, J.W.M. Experimental Evidence for Ice Formation at Room Temperature. *Physical Review Letters* **101**, 036101 (2008)

25. Jinesh, K.B. & Frenken, J.W.M. Capillary Condensation in Atomic Scale Friction: How Water Acts like a Glue. *Physical Review Letters* **96**, 166103 (2006)

26. Grill, A. Diamond-like carbon: state of the art. *Diamond and Related Materials* **8**, pp. 428-434 (1999)

27. Erdemir, A. The role of hydrogen in tribological properties of diamond-like carbon films. *Surf Coatings Technology* **146**, pp. 292-297 (2001)

28. Andersson, J. *et al*. Friction of diamond-like carbon films in different atmospheres. *Wear* **254**, pp. 1070-1075 (2003)

29. McFarlane, J.S. & Tabor, D. Relation between friction and adhesion. *Proceedings of The Royal Society A*, pp. 244-235 (1950)

30. Yoshizawa, H., Chen, Y. & Israelachvili, J. Fundamental mechanisms of interfacial friction. 1. Relation between adhesion and friction. *The Journal of Physical Chemistry* **97**, pp. 4128-4140 (1993)

31. Cross, R. Increase in friction force with sliding speed. *American Journal of Physics* **73**, 812 (2005)

32. Braun, O. & Peyrard, M. Dependence of kinetic friction on velocity: Master equation approach. *Physical Review E* **83**, 046129 (2011)

33. Liu, H., Ahmed, I.-U. & Scherge, M. Microtribological properties of silicon and silicon coated with diamond like carbon, octadecyltrichlorosilane and stearic acid cadmium salt films: A comparative study. *Thin Solid Films* **381**, pp. 135-142 (2001)

34. Opitz, A. *et al*. Nanofriction mechanisms derived from the dependence of friction on load and sliding velocity from air to UHV on hydrophilic silicon. *arXiv* (2005) doi:10.1007/s11249-005-8550-1

35. Chen, J., Ratera, I., Park, J. & Salmeron, M. Velocity Dependence of Friction and Hydrogen Bonding Effects. *Physical Review Letters* **96**, 236102 (2006)

36. Schirmeisen, A. *et al*. Temperature dependence of point contact friction on silicon. *Applied Physics Letters* **88**, 123108 (2006)

37. Landes, F.P. Introduction to Friction. Springer (2016)

38. Bo, L.C. & Pavelescu, D. The friction-speed relation and its influence on the critical velocity of stick-slip motion. *Wear* **82**, pp. 277-289 (1982)

39. Antoniou, S.S. *et al*.The friction-speed relation from stick-slip data. *Wear* **36**, pp. 235-254 (1976)

40. Persson, B.N.J. Theory of friction: Stress domains, relaxation, and creep. *Physical Review B Condensed Matter* **51**, 13568 (1995)

41. Zwörner, H. *et al*. The velocity dependence of frictional forces in point-contact friction. *Appl Phys Mater Sci Process* **66** (1998)

42. Braun, O.M. & Röder, J. Transition from Stick-Slip to Smooth Sliding: An Earthquakelike Model. *Physical Review Letters* **88**, 096102 (2002)

43. Bureau, L. *et al*. Low-velocity friction between macroscopic solids. C.R. Academy of Science Paris **2**, pp. 699-707 (2001)

44. Rozman, M.G. *et al*. Atomic Scale Friction and Different Phases of Motion of Embedded Molecular Systems. *The Journal of Physical Chemisctry B*, pp. 7924-7930 (1998)

45. Baumberger, T. *et al*. Physical analysis of the state- and rate-dependent friction law. II. Dynamic friction. *Phys Rev B* **60**, pp. 3928-3939 (1999)

46. Filippov, A.E., Klafter, J. & Urbakh, M. Friction through Dynamical Formation and Rupture of Molecular Bonds. *Physical Review Letters* **92**, 135503 (2004)

47. Baumberger, T. & Caroli, C. Solid friction from stick slip down to pinning and aging. *Advances in Physics* **55**, , pp. 279-348 (2008)

48. Briscoe, W. *et al*. Boundary lubrication under water. *Nature* **444,** pp. 191–194 (2006)

49. Kumar, D. *et al*. Super low to high friction of turbostratic graphite under various atmospheric test conditions. *Tribology International* **44**, pp. 1969-1978 (2011)

50. Bhowmick, S., Banerji, A. & Alpas, A. Role of humidity in reducing sliding friction of multilayered graphene. *Carbon* **87**, pp. 374-373 (2015)

51. Konca, C. *et al*. Effect of test atmosphere on the tribological behaviour of the non-hydrogenated diamond-like carbon coatings against 319 aluminum alloy and tungsten carbide. *Surface and Coatings Technology* **200**, pp. 1783-1791 (2005)

52. Ni, W. *et al*. Tribological behavior of diamond-like-carbon (DLC) coatings against aluminum alloys at elevated temperatures. *Surf Coatings Technology* **201**, pp. 3229-3234 (2006)

53. Barel, I. & Urbakh, M. Multibond Dynamics of Nanoscale Friction: The Role of Temperature. *Physical Review Letters* **104**, 066104 (2010)

54. Kalin, M. & Vizintin, J. A comparison of the tribological behaviour of steel/steel, steel/DLC and DLC/DLC contacts when lubricated with mineral and biogradable oils. *Wear* **261**, pp. 22-31(2006)

55. Bocquet L. *et al*. Moisture-induced ageing in granular media and the kinetics of capillary condensation. *Nature* **396**, pp. 735-737 (1998)

56. Gnecco E. *et al.* Velocity Dependence of Atomic Friction. *Physical Review Letters* **84**, pp. 1172-1175 (2000)

57. Sharma, N. *et al*. Velocity dependence of coefficient of friction of diamond like carbon coatings. *Solid State Physics* **1447**, pp. 651-652 (2012)

58. Li, H. *et al.* Humidity dependence on the friction and wear behavior of diamond-like carbon film in air and nitrogen environments. *Diamond and Related Materials* **15**, pp. 1585-1592 (2006)

59. Donnet, C. Recent progress on the tribology of doped diamond-like and carbon alloy coatings: a review. *Surface and Coatings Technology* **100**, pp. 180-186 (1998)

60. Shimizu, T., Kakegawa, T. & Yang, M. Micro-texturing of DLC Thin Film Coatings and its Tribological Performance Under Dry Sliding Friction for Microforming Operation. *Procedia Engineering* **81**, pp. 1884-1889 (2014)

61. Savage, R.H. & Schaefer, D. Vapor Lubrication of Graphite Sliding Contacts. *Journal of Applied Physics* **27**, 136 (1956)

62. Jiang, J., Zhang, S. & Arnell, R. D. The effect of relative humidity on wear of a diamond-like carbon coating. *Surface and Coatings Technology* **167**, pp. 221-225 (2003)

63. Hauert, R. An overview on the tribological behavior of diamond-like carbon in technical and medical applications. *Tribology International* **37**, pp. 991-1003 (2004)

64. Voevodin, A.A. *et al*. Mechanical and tribological properties of diamond-like carbon coatings prepared by pulsed laser deposition. *Surface and Coatings Technology* **76**, pp. 534-539 (1995)

65. Torun, B. *et al*. Study of water adsorption and capillary bridge formation for SiO_2 nanoparticle layers by means of a combined in situ FT-IR reflection spectroscopy and QCM-D set-up. *Physical Chemistry Chemical Physics* **16**, pp. 7377-7384 (2014)

66. Greiner, C., Felts, J., Dai, Z., King, W. & Carpick, R. Local Nanoscale Heating Modulates Single-Asperity Friction. *Nano Letters* **10**, 4640-5 (2010)

67. Sirghi, L. Transport Mechanisms in Capillary Condensation of Water at a Single-Asperity Nanoscopic Contact. *Langmuir* **28**, pp. 2558-2566 (2012)

68. Restagno, F. *et al*. Thermally activated dynamics of capillary condensation. *Journal of Physics: Condensed Matter* **12**, pp. 419-424 (2000)

69. Iwamatsu, M. & Horii, K. Capillary Condensation and Adhesion of Two Wetter Surfaces. *Journal of Colloid and Interface Science* **182**, pp. 400-406 (1996)

70. Reiss, H. & Koper, G.J.M The Kelvin Relation: Stability, Fluctuation, and Factors Involved in Measurement. *Journal Physical Chemistry* **99**, pp. 7837-7844 (1995)

71. Greiner, C., Felts, J., Dai, Z., King, W. & Carpick, R. Temperature Dependence of Nanoscale Friction Investigated with Thermal AFM Probes. *MRS Proceedings* **1226** (2009)

72. Krylov, S. & Frenken, J.W.M. Thermal contact delocalization in atomic scale friction: a multitude of friction regimes. *New Journal of Physics* **9**, 398 (2007)

73. Schwarz, U. & Hölscher, H. Exploring and Explaining Friction with the Prandtl–Tomlinson Model. *ACS Nano* **10**, pp. 38-41 (2016)

74. Zhao, X. *et al*. Transition from Thermal to Athermal Friction under Cryogenic Conditions. *Physical Review Letters* **102**, 186102 (2009)

75. Heimberg, J. Superlow friction behavior of diamond-like carbon coatings: Time and speed effects. *Applied Physics Letters* **78**, 2449 (2001)

76. Si-mat.com/silicon-wafers.html Visited on 05 April 2017

77. Popova, E. & Popov, V.L. The research works of Coulomb and Amontons and generalized laws of friction. *Friction* **3**, pp. 183-190 (2015)

78. https://www.vaisala.com/ Visited on 09 April 2017

79. De Barros Bouchet, M.-I. *et al*. Friction of diamond in the presence of water vapor and hydrogen gas. Coupling gas-phase lubrication and first-principles studies. *Journal of Physical Chemistry C*, **116**, pp. 6966-6972 (2012)

80. Levita, G., Restuccia, P. & Righi, M.C. Graphene and MoS_2 interacting with water: A comparison by ab initio calculations. *Carbon* **107**, pp. 878-884 (2016)

81.   Kim, S. *et al.* Effects of Humidity on the Friction Coefficient of Diamond-Like Carbon (DLC) Coating. *Journal of Korean Physical Society* **54**, pp. 2212-2218 (2009)

82.   Erdemir, A. & Eryilmaz, O. Achieving superlubricity in DLC films by controlling bulk, surface, and tribochemistry. *Friction* **2**, pp. 140-155 (2014)

83.   Scharf, T.W. & Singer, I.L. Quantification of the Thickness of Carbon Transfer Films Using Raman Tribometry. *Tribology Letters* **14**,pp. 137-145 (2003)

84.   Brennan, J. *et al*. Adsorption of Water in Activated Carbons: Effects of Pore Blocking and Connectivity. *Langmuir* **18**, pp. 5438-5447 (2002)

Chapter 6

Towards superlubricity of graphene on the macroscopic scale

6.1 Introduction

In 2004 Novoselov, Geim and co-workers showed in their experimental work the first two-dimensional (2D) atomic crystal – graphene – a honeycomb sheet of carbon [1, 2]. Even though the first pioneering theoretical work on graphene dates back as far as the mid-forties of the last century [3], the discovery by Novoselov *et al.* of a method to prepare graphene with minimal electronic interaction with its support has opened a new era of research. Since then the number of graphene-related scientific publications began to grow almost exponentially [4], demonstrating new properties and enabling new technologies with this special, two-dimensional material. Graphene is the lightest, thinnest and strongest material known to date [5]; also it shows record performance in terms of heat and electrical conductivity [6-11]. From a chemical point of view, defect-free graphene is unique too, being impermeable to all gases, including helium [12, 13], while at the same time being easily functionalized with various chemical species [14]. Therefore, the past decade has also witnessed significant effort into technology-oriented research, exploring new graphene applications – from new types of transistors [15, 16] to applications in solar cells [17] and in biomedical devices [18].

As graphene forms a natural constituent of graphite and graphite is commonly used as a solid lubricant, the frictional properties of graphene have attracted attention too [19, 47-52]. For instance, nanoscale friction force microscopy measurements on graphene supported by copper foils [20, 21] or by silicon oxide [22, 47] demonstrated a significant lowering of the friction forces on the graphene-covered patches with respect to graphene-free parts of these substrates. By virtue of recent developments in graphene growth techniques [23, 24], it is now becoming possible to study the impact of the presence of a graphene monolayer beyond the atomic scale, for example for single contacts in the micrometer regime and for macroscopic ensembles of large numbers of contacts. In one of the early works in this area, Kim *et al.* showed superior friction and adhesion properties of single-monolayer graphene films grown by chemical vapor deposition (CVD) on Cu and Ni substrates [28]. Later, Berman *et al.* demonstrated that graphene helps significantly to minimize wear and friction at the macroscale between a steel ball and graphene-covered solid substrates in various gas atmospheres [25, 26]; Mao *et*

al. measured a 10-fold reduction of the friction coefficients for Ag-based electrical contacts in the presence of graphene [27]. In later work, Berman *et al.* achieved extremely low friction, which they ascribed to macroscale 'superlubricity' enabled by the formation of so-called graphene nanoscrolls at the interface between a DLC coated substrate and a graphene coated counter surface [29]. They have demonstrated a sustained reduction of the friction coefficient to 0.004, which may be very promising for future lubrication technology.

Unfortunately, the term 'superlubricity' is used in the friction community with more than a single meaning. Whereas it often simply indicates extremely good lubrication, for example in the case of the nanoscrolls of ref. [29], the term 'superlubricity' was coined by Hirano *et al.* [30-33] to indicate a friction regime when 'two contacting surfaces can slide with no resistance', as the result of a mismatch between their lattices, for example when they are twisted out of registry. A perhaps more meaningful term to cover this narrower definition is 'structural lubricity'. In this chapter (as well as in the rest of this PhD thesis) we will use both terms, but always in the narrower context of a lattice mismatch. Hirano *et al.* demonstrated that the friction between two cleaved mica surfaces exhibits a modest variation between commensurate and incommensurate orientations of the two mica lattices. Later, electron microscopy observations on MoS_2-lubricated contacts suggested that a similar mechanism may be at play between the differently oriented MoS_2 flakes in such contacts [34]. Further evidence for structural lubricity on the nanometer scale has been acquired for e.g. graphene [46] and for graphite flakes [35]. In the latter case, Dienwiebel *et al*. demonstrated directly how friction becomes ultra-low when a graphite-graphite interface is rotated out of registry. The friction force is only high when the lattices can lock in, which occurs every 60° of rotation, corresponding to the rotation symmetry of the graphite lattice [83] Since superlubricity is intimately related to the crystalline structure of the contacting materials, one may expect that it would be sensitive to the crystalline quality of the materials, for example to the density of lattice defects. If this is indeed the case, this is important for practical applications, for which the contact sizes are usually much larger than the nanocontacts of the early demonstration experiments. So far, the largest contacts for which structural lubricity has been demonstrated are graphite-graphite contacts with areas of a few hundred μm^2 [36, 37].

A promising candidate material that might be effective as a low-friction coating, by preserving the effect of structural lubricity even on the macroscopic scale, is graphene. One of the great advantages of a graphene coating could be that it smoothly decorates the natural irregularities of the substrate on which the graphene is either grown or to which it is transferred. Imperfections in the substrate, such as atomic steps, grain boundaries and point defects are covered such that we may hope their effect on friction to be minimized. A graphene coating would further avoid direct atomic contact between the substrates and thus prevent the formation of chemical bonds that would otherwise lead to high friction and wear. Nowadays, graphene is produced over areas that are large enough to be used as a macroscopic-scale coating, albeit that the structural quality of this graphene is still far from perfect. Nevertheless, graphene may be regarded as one of the most promising candidate materials to achieve superlubricity at the truly macroscopic scale.

In this chapter, we discuss the results of our experiments towards superlubricity on the macroscopic scale with commercial CVD-grown graphene on polycrystalline Cu substrates. Also, we conducted some basic, 'Leonardo-da-Vinci style' [38] experiments to study lubrication properties of monolayer graphene on cm^2–scale sliding contacts. Finally, we discuss the oxidation behavior of graphene-coated substrates under ambient conditions and the local effect of that oxidation on the friction properties.

6.2 Experimental

For our experiments, we used high-quality, single-monolayer graphene samples that were commercially produced by Applied Nanolayers (ANL) BV [39]. In ANL's production process, graphene is grown by CVD on polycrystalline copper films. These films are formed by sputter deposition of copper on sapphire (111) wafers (diameter $51\ mm$, thickness $750\ \mu m$). The copper grains in the film showed a strong preference for the (111) surface orientation. We used these graphene samples both as the stationary, lower body in our sliding experiments and as the upper body, the slider. For these experiments, the sliders had to be smaller in size than the lower bodies; we prepared them by dicing graphene-coated wafers into squares with dimensions of $1 \times 1\ cm^2$ and a mass of $m = 0.16\ g$. Dicing was performed under cleanroom conditions in order to avoid dust contamination. Prior to dicing, the wafers were spin-coated with S1805 photoresist [40], in order to protect them against small-particle debris that originates from the dicing itself. The photoresist was spin-coated at $4000\ RPM$, and baked out at $130°C$ for $60\ sec$ in air. The wafers were diced with a rotary dicing machine using a precision diamond blade VT-07 [41] at $20000\ RPM$. Afterwards, the photoresist was washed off from the diced samples in N-methyl-2-pyrolidone at $80°C$ during 5 minutes. Finally, the samples were quickly rinsed in demi-water and dried with N_2 gas. The graphene quality was monitored before and after this complete dicing operation with optical microscopy and Raman spectroscopy. These control measurements did not reveal any measurable increase in defect density in the graphene, no transferred contamination and no signs of damage. Therefore, we assume that the graphene quality remained close to that of the original graphene coating. It is also important to indicate that all friction experiments were conducted shortly after (several days) the samples were coated with graphene and prepared in the cleanroom. Some samples that were exposed to air for longer times (up to a few months) became oxidized and this effect will be discussed separately.

For comparison, we have performed friction experiments not only with graphene-coated substrates but also with uncoated copper films. These were prepared and diced following precisely the same protocol as the graphene-coated samples.

Similar to the experiments with DLC coatings, reported in Chapters 4 and 5, the macroscopic friction measurements of this Chapter were performed with the Bruker UMT-1 Universal Mechanical Tester. For details of this instrument, see Chapter 4. In our experiments, the lower of the two contacting bodies was mounted directly on the substrate table of the microscope, while the smaller counter-sample was positioned on top of it under its own weight of $1.56\ mN$. The normal force could be increased beyond this level by placing an additional weight on top. Lateral (friction) forces were measured while pushing from one of the sides against the counter-sample at a fixed driving speed of $5\ \mu m/sec$. In another type of measurements, we imposed a continuous in-plane rotation of the counter-sample with respect to the lower body at a speed of $0.01\ deg/sec$. To this end, we rotated the stage with the lower body mounted in its center. The square counter-sample was placed in the middle of the substrate. The pusher block of the UMT was placed against one of the sides of the counter-sample, keeping the counter-sample from rotating with the substrate and measuring the force (torque) that was required for that.

In addition to measurements on the macroscale, we have also conducted friction measurements on the nanoscale. These were done with a Bruker AFM Icon, using V-shaped Si_3N_4 probes (DNP-10). The relative humidity could be controlled by flushing the AFM chamber with nitrogen vapor from a liquid nitrogen reservoir. The height of the tip was measured to be $h = 4.0 \pm 0.5\ \mu m$, the length of the beams of the cantilever $L = 210 \pm 2\ \mu m$ and the angle between them $\theta = 60° \pm 0.5°$. The normal spring constant k_N for each cantilever was obtained from a measurement of its natural frequency (for the method see [61]). The lateral spring constant k_L of was calculated based on the measured value of k_N and the geometry of the cantilever [55, 62]:

$$k_L = \frac{2}{[6cos^2\theta+3(1+v)sin^2\theta]} \left(\frac{L}{h}\right)^2 k_N. \qquad (6.1)$$

Here, v is the Poisson ratio (for SiN, $v = 0.27$). Typical values of k_N and k_L for the employed cantilevers are in the range of $0.05 - 0.2\ N/m$ and $35 - 120\ N/m$, respectively. We followed the lateral and normal force calibration procedure of refs. [55, 60]. The normal force was determined on the basis of the measured

voltage response of the photo-diode V_N during normal bending of the cantilever in contact with the substrate. Force-distance curves were recorded in order to determine the normal sensitivity S_N. The resulting force value is then given by:

$$F_N = k_N S_N V_N. \tag{6.2}$$

To calculate the lateral force, we used a relation between the lateral S_L and normal sensitivity S_N. According to [61] the two are related by:

$$S_L = \frac{3}{2} k_L \frac{h}{L} S_N. \tag{6.3}$$

Thus the lateral force can be found

$$F_L = k_L S_L V_L, \tag{6.4}$$

where V_L is the relative change in voltage signal from the photo-diode due to lateral bending of the cantilever.

We have also conducted micro-Raman spectroscopy experiments. These were conducted with a laser wavelength of 514 nm and a spot size of ~1 μm. SEM inspection was performed with a FEI Verios scanning electron microscope.

6.3 Experimental results

Figure 1 represents typical results of the SEM and Raman inspection of a freshly coated graphene sample. Because of highly homogeneous character of the graphene film, the SEM image shows hardly any contrast and the only clearly visible structures are related to grain boundaries (GB) in the underlying copper film (Fig. 6.1a). In turn, the Raman spectrum (Fig. 6.1b) provides information on the defects in the graphene layer itself (D-band around 1360 cm^{-1}), the in-plane vibrations of the sp²-bonded carbon atoms (G-band at 1595 cm^{-1}), and the stacking order in the case of multilayer graphene (2D-band around 2730 cm^{-1}). The symmetric and sharp 2D-peak indicates that this is a graphene monolayer [42, 43]. The peak intensity ratio of $I_{2D}/I_G > 1$ also indicates the presence of only monolayer

graphene, albeit that this ratio strongly depends on the laser excitation energy and is sensitive to the details of the binding between the graphene layer and the substrate [44]. It was demonstrated that in the green laser range (an excitation energy of $2.2 \div 2.4\ eV$) the intensity of the Raman resonance profile becomes stronger than at higher energies (above $2.8\ eV$). This effect is related to the photoluminescence band of the Cu substrate. In our experiments, we employed a laser wavelength of $514\ nm$, which corresponds to the excitation energy of $2.41\ eV$. The acquired spectrum is in a good agreement with the literature [42-44]. The spectrum in Fig. 6.1b is shown after the subtraction of the background from the luminescence from the copper substrate.

a)   b)
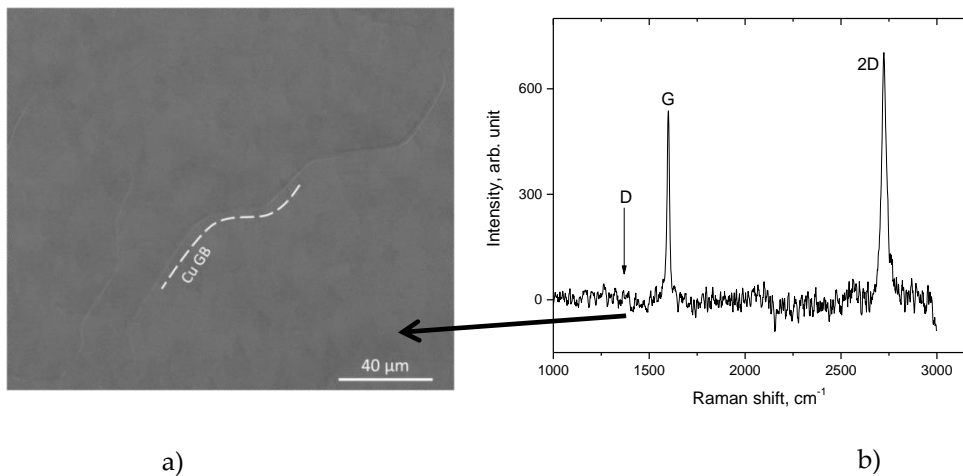
Figure 6.1. SEM image (a) and Raman spectrum (b) of CVD grown graphene on top of a polycrystalline Cu film. The dashed line in (a) highlights part of a grain boundary in the copper film. The absence of a D peak in (b) indicates the negligible density of structural defects in the graphene lattice; the ratio between the heights of the G and 2D peaks and their positions correspond to those for monolayer graphene.

Figure 6.2 shows friction measurements for two different interfaces, namely the interface between two copper surfaces and the interface between two samples coated with monolayer graphene. These measurements were performed in ambient, in a relative humidity of 45%. Note, that the formation of an oxide film at the surface of copper proceeds immediately after its exposure to ambient air and after 1 hour of exposure the typical thickness of the Cu_2O already amounts to $2.5 \pm 0.2\ nm$ [45]. It has also been demonstrated that the thickness of the copper

native oxide finally stabilizes after 66 days of exposure and reaches a thickness of $5.2 \pm 0.5\ nm$. Therefore, we refer to the copper-on-copper results as Cu₂O on Cu₂O. The effect of the graphene coatings is dramatic. They reduce the friction coefficient by more than a factor 3 ($\mu_d = 0.14$) with respect to the uncoated samples ($\mu_d = 0.43$).
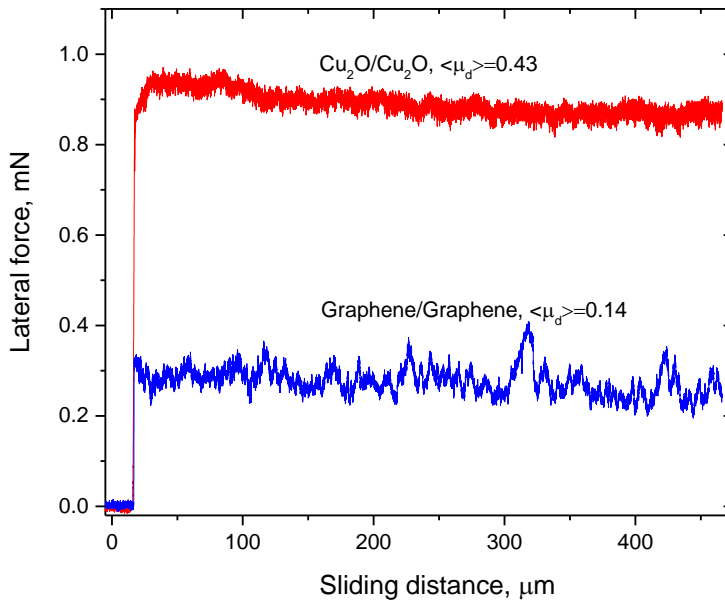

Figure 6.2. Comparison of the friction forces between two samples coated with monolayer graphene (blue curve) and two oxidized copper samples without graphene (red curve). Sliding speed = 5 µm/sec, $F_N = 2\ mN$, and RH = 45%.

Figure 6.3 represents the initial stages of the same sliding experiments as those in Fig. 6.2, showing the transition from the static situation, with the slider at rest, to steady sliding motion for the graphene/graphene and native oxide Cu₂O/Cu₂O friction pairs. While the transition to steady sliding requires the overcoming of a static friction barrier for the Cu₂O/Cu₂O case, the graphene/graphene pair seems to exhibit no difference between the static (μ_s) and dynamic (μ_d) coefficients of friction. Both measurements were done after the sliding surfaces spent 2 min in rest.
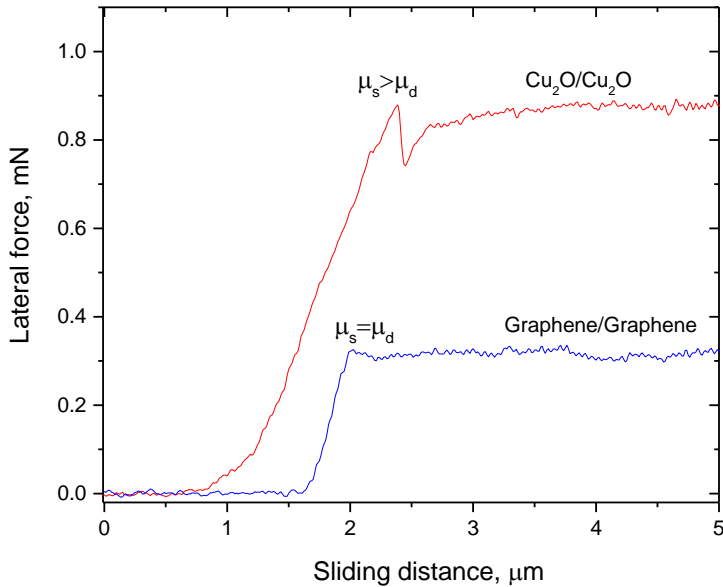
Figure 6.3. Transition from static friction to steady sliding (same data as Figure 6.2, on expanded horizontal scale) for two samples coated with monolayer graphene (blue curve) and two oxidized copper samples without graphene (red curve). Sliding speed = 5 µm/sec, $F_N = 2\ mN$, and RH = 45%.

An example of a measurement of the frictional torque during the relative rotation of two graphene-coated samples is shown in Fig. 6.4. The substrate was sequentially rotated over 120° in the clockwise and counterclockwise directions. The mean value of the frictional torque is in full agreement with the force measured in the linear sliding geometry of Figs. 6.2 and 6.3, indicating that also in the rotation measurements, the graphene coatings reduce friction. Naively, one might have expected that, following the scenario of structural lubricity [33-36], the friction signal should display a characteristic variation with rotation with a period of 60°, between a low level for most angles and a pronounced maximum for the angels at which the two contacting graphene lattices would align and lock in. The friction data in Fig. 6.4 do not show such a periodic signature. We have used a standard rotational rheometer (Anton Paar DSR301) to perform additional experiments in search of rotational symmetry in the friction between the lattices of macroscopic graphene coatings [82]. The results from these rheometer experiments

were similar to those in Fig. 6.4; again we find no evidence in the forces for the periodic alignment of the graphene lattices. We will put forward an explanation for the absence of a periodic variation in the friction forces in the Discussion section.
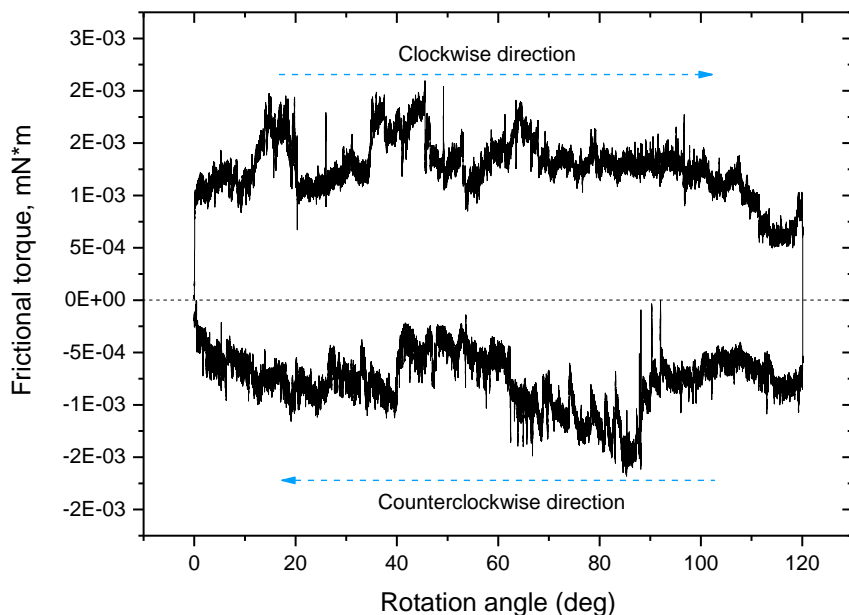
Not only the copper surfaces responded to the atmosphere, but we found that also the surface topography of our graphene samples slowly evolved under ambient conditions. A comparison of AFM-images on a graphene-covered sample before and after 2 months in air is presented in Figs. 6.5a and b. Figure 6.5c shows an optical micrograph of the same sample after 2 months in air. The AFM image in Fig. 6.5a is characteristic for high-quality graphene on relatively flat and smooth copper. A modest overall height variation is visible and individual steps of the copper substrate can just be distinguished. Figure 6.5b shows the same area with the same features. In addition, a fine network of protruding lines and islands is visible. The image of Fig. 6.5c shows a similar network, where the optical contrast

has changed. We associate these slow changes with oxidation of the copper substrate. Structurally perfect graphene is impenetrable for oxygen, and structural defects in the graphene, such as the graphene grain boundaries (GGBs) form the only locations where oxygen can pass and reach the copper. This gives rise to a slow, diffusion-limited oxidation that sets in at the GGB and spreads out sideways to oxidize the copper under the graphene. The optical image also contains a grain boundary in the copper film that shows up with a different contrast than the oxide-decorated GGBs. Note, that the orientation of the GGBs is independent of the orientation of the Cu steps and they even cross Cu GBs (Fig. 6.5c). The black dots in the optical micrograph (Fig. 6.5c) are regions of bulk copper oxide that have grown in height above the sample surface and are not dressed with graphene anymore. This is concluded from Raman measurements conducted at these locations. Presumably, they are formed at places along the GGB with the highest defect density, which enables a relatively high oxidation rate [54].

a)

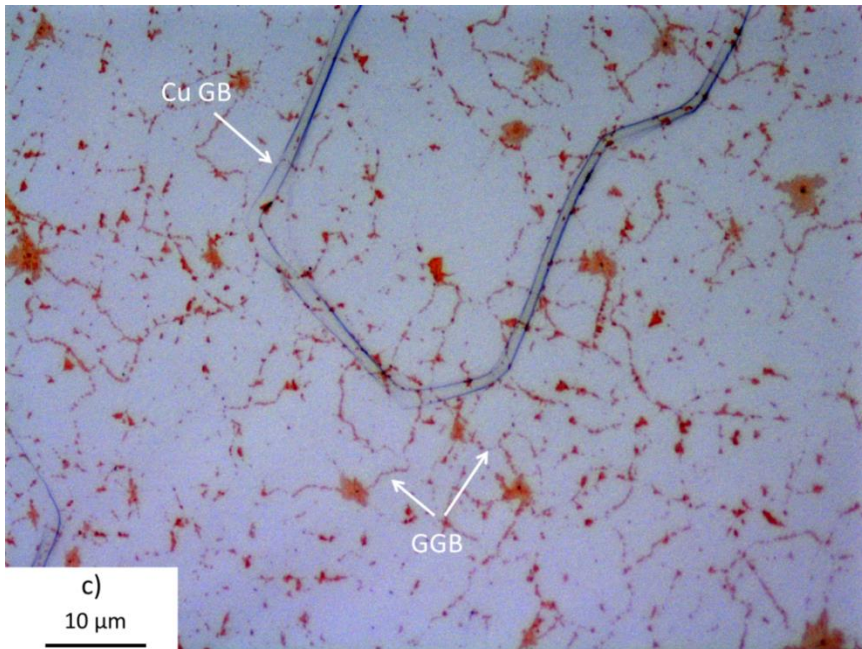10.0 μm

b)

Cu oxide
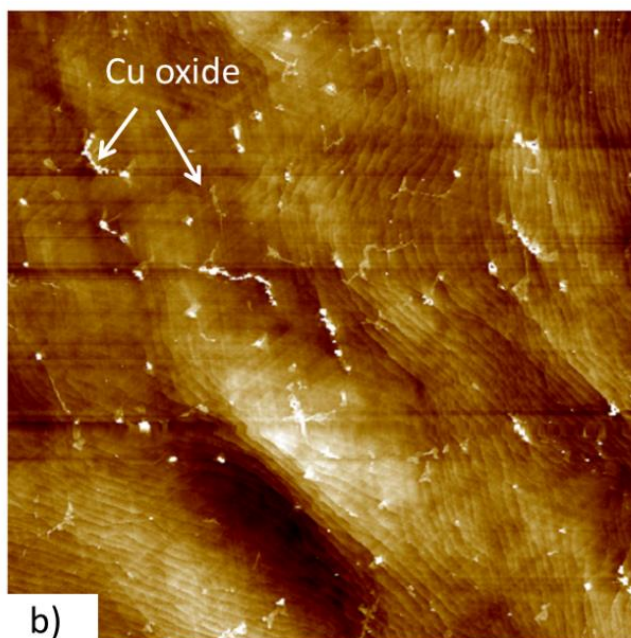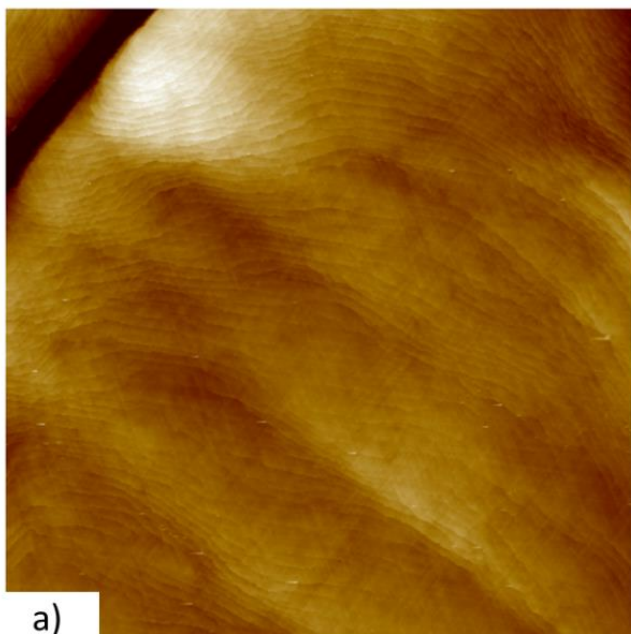
27.4 nm

10.0 μm

Figure 6.5. AFM and optical images of a graphene-covered copper surface. (a) AFM image shortly after coating with graphene (a few days exposed to air). (b) AFM image of nearly the same surface region after 2 months of exposure to air. Note the decoration of the network of GGBs with oxidized copper underneath. (c) Optical micrograph after 2 months of exposure to air, showing the network of oxide-decorated GGBs. The image also shows a Cu GB. Note, that the orientations of the GGBs do not seem to be affected by the orientation of the Cu GB.

In order to further characterize the slow oxidation, we acquired Raman spectra on the oxidized areas of the copper substrate close to a GGB and compared them with spectra taken on the unoxidized areas (at a distance from the GGBs). An example of such a comparison is presented in Fig. 6.6. The two spectra in Fig. 6.6 were taken with a rather low laser power of $8 \, \mu W$, which corresponds to 0.1% of the laser's nominal power. This was necessary to avoid heat damage produced by the laser to the copper oxide, but it resulted in a weakening of the signal to noise ratio in both spectra (Fig. 6.6).

In the regions where the copper oxidation is visible, we find that both the G- and the 2D-band are 'redshifted' with respect to the bands for 'regular' graphene on bare, unoxidized copper. The average position of the G-band shifted from $1592 \, cm^{-1}$ to $1585 \, cm^{-1}$, and that of the 2D-band from approximately $2727 \, cm^{-1}$ to $2680 \, cm^{-1}$. In spite of these changes, we could not detect the D-band that would be

associated with defects in this graphene on top of the oxidized copper. The intensity ratio of the 2D- and G-bands on the oxidized copper was $I_{2D}/I_G = 2.3$, which is much higher than the ratio of $I_{2D}/I_G \approx 1$ for unoxidized areas. Some arguments for the increased peak intensity ratio follow in Discussion section. Previously, a similar redshift of the characteristic Raman bands was reported for graphene-coated copper samples, which were oxidized on purpose with ultraviolet radiation (UV) in oxygen atmosphere [54, 58]. In turn, the redshift of the characteristic bands is known to indicate tensile strain in the graphene. In our case, there is a natural reason for such strain, in view of the increased volume below the graphene due to the oxidation of the copper [58]. The redshifts in Fig. 6.6 correspond to approximately 0.5 to 1.5% of tensile strain [57].

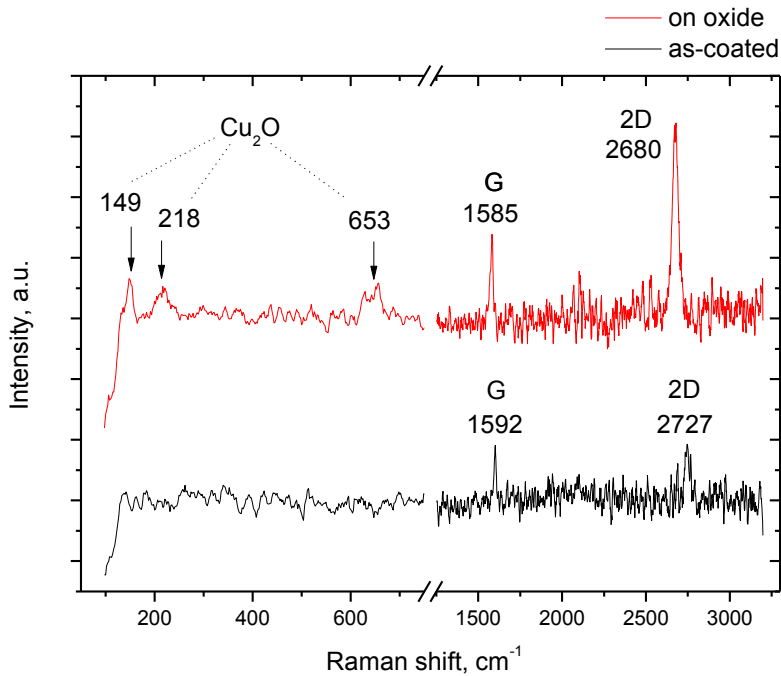*Figure 6.6. Raman spectra of graphene on copper (black line) and graphene on a region with oxidized copper (red color), taken with a laser excitation wavelength of $514\,nm$. Note the 'redshift' of the G- and D-bands on the oxidized substrate. Also, there are three extra peaks at 149, 218, and 653 cm^{-1}, associated with Raman scattering on copper oxide (Cu_2O). The spectra are vertically shifted for clarity.*

Figure 6.7 represents an example of a $2x2\ \mu m^2$ region of the locally oxidized sample, inspected with both AFM and FFM. In the center of Fig. 6.7a there is a copper oxide island with an average height of $2.5\ nm$ (Fig. 6.7b). On the left and right of it, the white arrows point at a GGB that runs across the oxide island. The GGBs typically observed on the studied samples show up as a protruding line with a height in the range of 0.3 to $1.5\ nm$. This elevation along the GGBs can be presumably due to (i) elastic strain and mechanical deformation as a result of the lattice mismatch induced by the two different grains [53, 59] or (ii) growth of the copper oxide under the GGB. In the example of Fig. 6.7, the GGB is measured to be $0.6\ nm$ in height (Fig. 6.7c). The GGB is difficult to distinguish on the island itself, because of the relatively high roughness. Figures 6.7d and e present the FFM scans taken in the forward (left-to-right) and reverse (right-to-left) directions, respectively. Interestingly, the FFM measurements indicate that the friction force is lower on the graphene areas below which the copper is oxidized. Both friction signals indicate a relative increase of the lateral force everywhere along the GGB, which we ascribe to the protruding height of the GGB, and possibly also to local oxidation of the graphene – something that Raman spectroscopy would not be sensitive to at this scale, due to relatively large laser spot size.
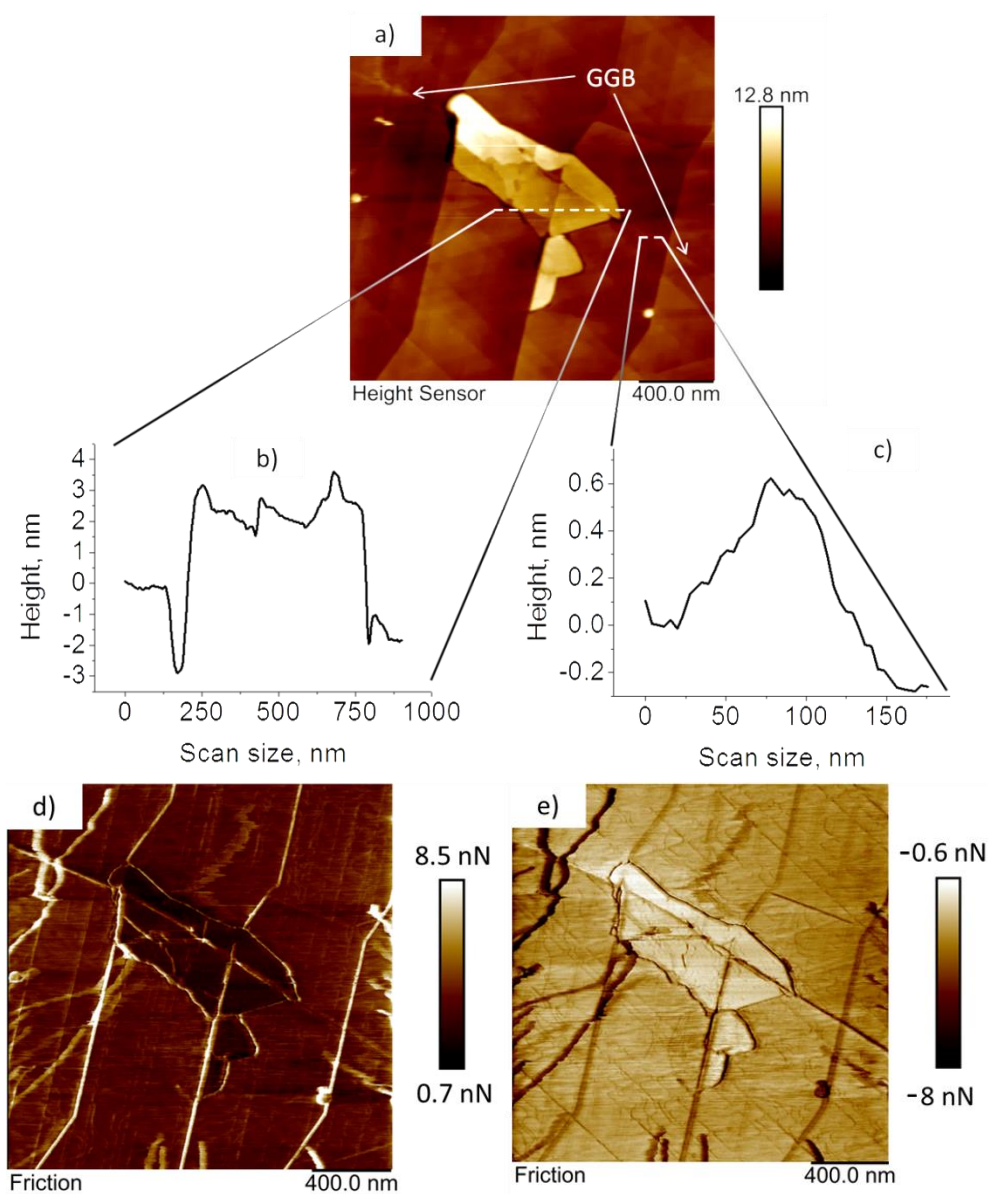
Figure 6.7. AFM and FFM scans of a region on a graphene-covered sample that contains an oxidized area of copper. The GGB that has served as the starting point for this oxidation can be recognized. a) AFM image; b) height profile across the oxide island; c) height profile across the GGB; d,e) lateral force maps of the same area measured in trace and retrace directions respectively. Scan area is $2x2\ \mu m^2$, normal force $F_N = 20\ nN$, scan speed is $1\ \mu m/sec$, $RH\ =\ 45\%$.

The dependence of the lateral force on the normal force for graphene on copper and graphene on copper oxide is presented in Figure 6.8 for another copper oxide island than the one in Fig. 6.7. The scan area was fixed to $1.5x0.5\ \mu m^2$, with the oxide region in the center. The measurement was conducted in ambient in the range of normal forces from $F_N = 23.7$ to $33.0\ nN$, with a cantilever with normal and lateral spring coefficients of $0.09\ N/m$ and $38\ N/m$, respectively. The lateral force values were calculated based on averaged data taken along the white dashed line that was chosen randomly in the scan image (Fig. 6.8). It is clear from the two curves in Fig. 6.8, that their slopes are very different. These slopes correspond to the two friction coefficients that we determined by linear regression to the measured data (Fig. 6.8e). The friction coefficient obtained in this way on graphene/copper oxide areas is $\mu = 0.034 \pm 0.02$, while it is $\mu = 0.093 \pm 0.02$ on the graphene/copper areas. Again, a local maximum in the lateral force was observed across the GGB (Fig. 6.8c,d).
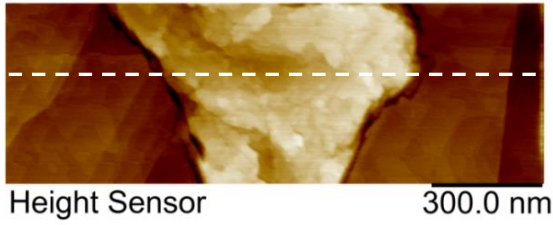
a)
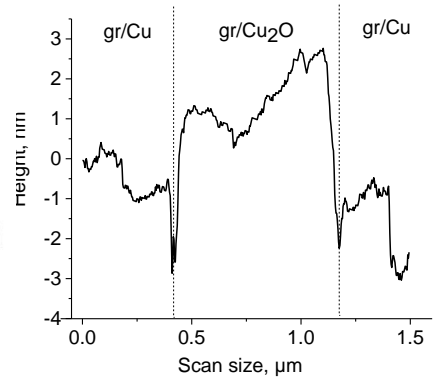
b)
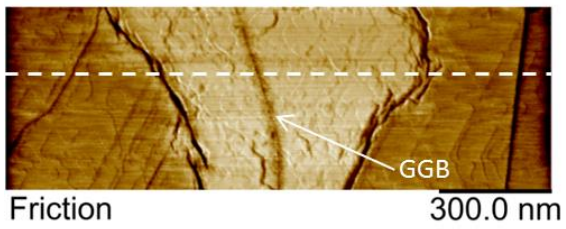
c)
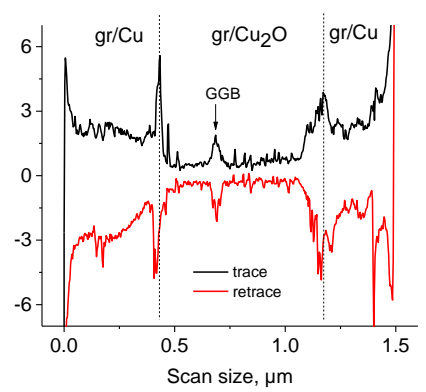
d)
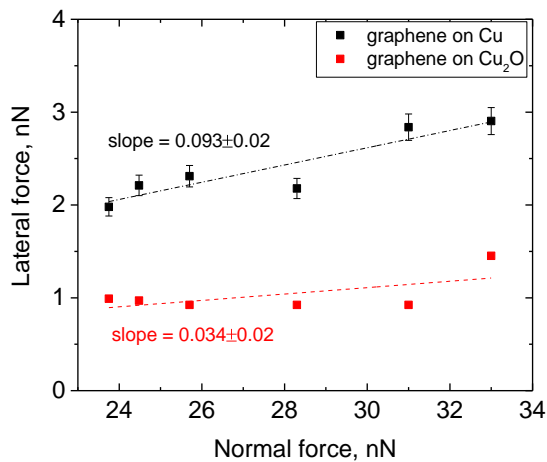
e)
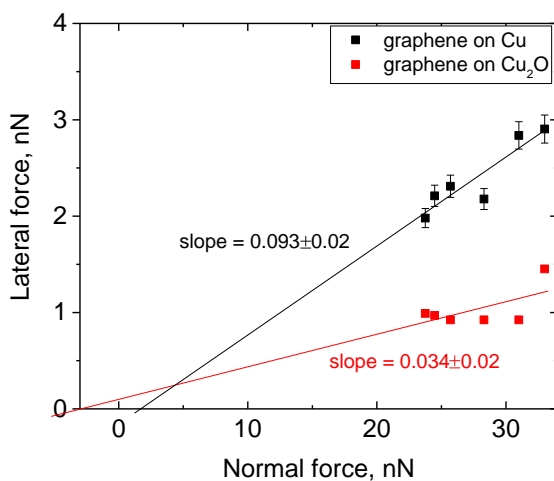
f)

Figure 6.8. Quantitative comparison of friction properties of graphene on copper (gr/Cu) and graphene on copper oxide (gr/Cu₂O). a) AFM image of a 1.5x0.5 μm², region of graphene-coated copper, with a copper oxide island in the center; b) height profile across the copper oxide island taken along the dashed line in a); c) lateral force image of the same area taken in the retrace (right to left direction) at $F_N = 23.7$ nN; d) lateral force profile taken from trace and re-trace scans along the dashed line in a); e) dependence of the (absolute value of the) lateral force on the normal force for graphene/copper and graphene/copper oxide, measured along the same dashed line in a) for normal forces in the range of $F_N = 23.7 \div 33.0$ nN; f) extrapolation of the linear data fit from e) to the point of origin (0,0).

144

6.4 Discussion

6.4.1 Graphene as the thinnest lubricant

We have demonstrated the suppression of the dynamic (sliding) friction coefficient by approximately a factor 3 and also the significant reduction of the static friction coefficient by applying only a single monolayer of graphene on both contacting surfaces. We have used flat graphene samples that were obtained by direct graphene growth on copper substrates and that did not undergo any subsequent transfer to another substrate. This means that in our experiments the contact between the sliding copper surfaces was fully determined by graphene/graphene interaction. High quality and complete coverage by graphene form key elements in our explanation of the observed frictional behavior. We interpret our observations as evidence that most, if not all, of the copper asperities in our contacts were "shielded" by the graphene and thus protected from direct formation of metal-metal bonds. Therefore, the interaction between the sliding surfaces was changed from chemical to purely physical [63]. As perfect graphene has an intrinsically low surface free energy, it results in a significant lowering of the interfacial adhesion and a correspondingly strong lowering of the shear strength of the interface. This is illustrated by recent density functional theory (DFT) calculations, which show that even partial coverage of iron surfaces with graphene ribbons may reduce the adhesion between them by almost a factor 6 [63]. This is confirmed by the experimental observations in ref. [25] for steel surfaces decorated with graphene flakes. Next to the reduced adhesion, also structural lubricity, i.e. the lubricating effect of the mismatch between randomly oriented graphene or graphite lattices [35], should be expected to contribute greatly to the reduction of the friction force. Another effect that graphene may introduce, is that the elastic behavior of the graphene coating may reduce the plastic penetration depths of the asperities on the copper surfaces, thus enhancing the load capacity of the graphene-decorated copper-copper interface [64]. The final element to add is that the graphene-covered copper surfaces should be expected to suppress the increase in the friction coefficient that is typical for bare copper surfaces in humid environments. Graphene should reduce the tendency for capillary condensation of water between the contacting surfaces, since it is less hydrophilic than copper

oxide. In addition, it was demonstrated that adding graphene to a Cu surface may increase the mobility of water droplets due to depinning of water contact lines, in contrast to hydrophilic copper oxide surface [61]. Together, these effects should reduce the effect that capillary water bridges have on the confined areas of contact between graphene/copper samples. All of these elements contribute to our expectation that a graphene-coating reduces the friction between copper surfaces. More systematic experiments are needed in order to investigate how strong each of these effects is.

Not only the dynamic friction force is reduced by the graphene, also the static peak that usually accompanies the onset of sliding is strongly affected; within the noise level of our measurement, it is absent completely when the graphene coating is present. Also this is no surprise. Normally, capillary water bridges and structural and geometrical pinning effects between the contacting asperities add significantly to the static friction threshold [67]. All these effects are strongly suppressed by the presence of the graphene coating.

An important question is, how long these unique lubrication properties of the ultrathin graphene coating should be expected to last. Like any other material, graphene exhibits a certain wear rate, which determines its lifetime as a lubricant [72]. The beneficial role of the graphene should hold at least as long as it remains present and the high structural quality of the graphene is maintained on those parts of the surfaces that are in mechanical contact. Local damage of the graphene layer under load should lead to the accumulation of carbon dangling bonds. These should result in higher interfacial adhesion due to both the direct cross-linking between damaged graphene layers and the bridging via water molecules and hydrocarbon groups that can bind easily to these dangling bonds [19, 65-66]. In particular, Berman *et al*. [66] demonstrated significant reduction of the graphene wear rate by means of passivation of the dangling bonds with hydrogen atoms from the hydrogen gas atmosphere, which could make graphene extra effective for lubrication in realistic applications. In our study, we have examined the wear of graphene by means of Raman spectroscopy. For this, we have conducted sliding experiments only over relatively short distances of typically several millimeters. In the Raman spectra after sliding, no significant increase of the D-band intensity was detected. Even though this result is highly encouraging, we can regard it as no

more than a preliminary result, until we have conducted a more systematic Raman study over larger areas of the studied substrates and after more extensive sliding.

It may come as a surprise that graphene is so effective on copper substrates, in view of the weak, Van-der-Waals type bonding that characterizes the interaction between the graphene and the copper. Graphene makes chemical bonds only to metals as Co, Ni, Pd and Fe [63, 68-71] that have incompletely filled d bands. Graphene binds to a Cu substrate purely by physisorption, because the d band of Cu is fully occupied. Therefore, the adhesion energy of graphene on copper is much lower (up to a factor 6, compared to Ni and Fe) [63, 69]. As a result, one might anticipate significant distortions of the graphene on copper under the combination of normal and shear forces, which would make the graphene much more vulnerable to wear on this substrate. Nevertheless, the millinewton range of normal loads and the millimeter range of travel distances used in our experiments has not resulted in any directly observable wear. We also did not measure any significant reduction in the lubricating effect of the graphene. An increase in the friction coefficient would have been a sign of the local detachment or modification of the graphene in the actual contact regions.

6.4.2 Towards superlubricity at the macroscale

The superlubric behavior that was demonstrated for graphitic materials at the nano- and microscale [35, 36] has served as the motivation to use CVD-grown graphene in order to extend this effect even further, to the macroscopic scale. One of the questions in this experiment is whether or not the structural quality of the graphene could be sufficiently high to use it for this purpose. The experiments in this Chapter clearly demonstrate a significant reduction of the static and dynamic friction coefficients between two surfaces resulting from the presence of single-monolayer graphene on both contacting surfaces. An important question is to what extent this friction reduction derives directly from superlubricity, i.e. from the friction-lowering effect introduced by the mismatch between the contacting graphene lattices. In the previous section, we have provided several other reasons for friction to be low in the presence of a graphene coating. In the experiment of Fig. 6.4, we have tried to obtain direct evidence of the lattice-mismatch scenario of structural lubricity by making use of the strong orientational alignment of the

specific graphene samples that we have used, which was within $\pm 1°$. Naïvely, one might expect this to lead to a measurable angular dependence of the friction coefficient, with sharp maxima every 60°, separated by a low friction level for all other angles. There is a simple explanation for the absence of such a signature in Fig. 6.4.

We first point out that the data in Fig. 6.4 show a significant variation in the friction force and that the difference between the average friction coefficients measured in clockwise ($\mu = 0.15$) and counter-clockwise directions ($\mu = 0.25$) suggests the presence of a certain, third-body contact element. This could be an edge effect of the counter sample, introduced by its dicing from the original wafer. Lateral forces and instabilities introduced by such an effect might obscure the increase in friction introduced by a commensurate orientation of the graphene lattices. Another complicating element is the possible presence of water condensates between the contacting surfaces, even though our measurements were conducted in a relatively dry environment (RH = 2%). In addition to these practical difficulties, we find that there is a more intrinsic difficulty in measuring a macroscopic lattice alignment effect.

We first observe that, even in the high-quality CVD-grown graphene that we have employed, the graphene domains still display a range of orientations of $\pm 1°$ with respect to the average orientation angle. This angular range is probably already large enough to 'destroy' the alignment effect, that would lead to a maximum in the friction coefficient, every 60°. As argued in ref. [81], the minimum rotation angle at which this 'destruction' occurs is inversely proportional to the diameter of the contact between the two surfaces. The size that is relevant here is the minimum of three characteristic dimensions, namely (i) the effective diameter of the entire structure, which is in the order of $1\,cm$, (ii) the diameter of the graphene domains, which is typically between 1 and 50 μm, and (iii) the diameter of each microscopic region of 'real', physical contact between the two bodies, which is typically $1\,\mu m$. Obviously, the latter, i.e. $1\,\mu m$, is the more appropriate choice. Even though this seems to be a relatively small diameter, it still corresponds to some 4.000 unit cells of the graphene structure. Hence, the width of the friction peak for each individual microcontact is expected to be as narrow as $0.25\,mrad$ or 0.014° [81].

While this angular width of the alignment effect of a single microcontact should be still within reach of the experimental accuracy of the employed rheometer, we should also take into account the fact that over the full, $1 \times 1\ cm^2$ area, simultaneous contact is made over a large ensemble of such microcontacts. The individual microcontacts are typically sufficiently far apart from each other to be associated with different grains and, hence, to differ in their local graphene orientations by the characteristic $\pm1°$ width of the orientational distribution. This convolutes the narrow $0.014°$ peak of a single contact with the full $\pm1°$ angular width of the domain orientation distribution, which should broaden the measured friction peak to a width of $2°$ and reduce its height by an equivalent factor 140. Probably, this combination has made the remaining alignment effect too small to show up in Fig. 6.4.

We conclude this section by stressing that the difficulty to observe lattice alignment in the friction forces does not render the structural lubricity effect insignificantly small. On the contrary, in this scenario, structural lubricity is so dominant and leads to such narrow friction peaks, that even when the contacting surfaces are optimally aligned, the $\pm1°$ angular distribution of their graphene orientations is already wide enough to make most of their microcontacts fully superlubric.

6.4.3 Effect of substrate oxidation on nanoscale friction of graphene

Prolonged exposure to ambient conditions was observed to lead to oxidation of the copper substrate under the graphene. This oxidation was found to proceed via structural defects in the graphene, in particular along the graphene grain boundaries (GGBs). Due to the impermeability of well-ordered graphene [12], the rest of the copper film was not oxidized. AFM measurements (Fig. 6.7, 6.8) conducted on the graphene samples after 2 months of exposure to air, indicated a local increase of the height of the oxidized regions by 1 to 4 nm. The Raman spectra showed that the oxide areas were still covered with low-defect-density graphene.

On top of the threefold reduction in friction that a single graphene monolayer introduced on copper, we find that friction is reduced on average nearly by an additional factor 3 when the copper substrate below the graphene is oxidized. Since copper oxide is a semiconductor, it may introduce electrostatic

forces at the contact interface, in contrast to metals, for which conduction will remove such electrostatic effects. However, it was shown earlier that compensation of the contact potential between the tip and the graphene on a SiC substrate did not result in changes in the friction force [73, 74]. In order to fully exclude electrostatic effects in our case, we should repeat our measurements systematically, with different tips and applied bias voltages.

The observed redshifts of the G- and 2D-bands in the Raman spectra were interpreted as a signature of 0.5 to 1.5% tensile strain in the graphene lattice, due to the increased volume of the substrate (copper oxide) under the graphene [54, 57, 58]. The increase of the I_{2D}/I_G ratio (Fig. 6.6), results from a relatively strong increase of Raman intensity from graphene in the presence of copper oxide, which is simply due to difference in light/matter coupling of the graphene on metal and dielectric surfaces [58]. Unoxidized copper substrate causes strong cancelation of the electric field component of the laser radiation due to its metallic nature. In contrast to that, this cancelation is significantly reduced on the semiconductor copper oxide film, which significantly increases the light coupling with the graphene layer on the oxide. Presumably, the 2D-band of graphene is more sensitive to this effect and its intensity increases more than that of the G-band.

It was suggested earlier that graphene, due to its elastic properties, may slightly lift up from the substrate and snap into contact with the tip due to tip-graphene adhesion, the so-called 'puckering effect' [20, 74, 75]. This effect results in a higher lateral force between the tip and graphene monolayer, because one should now invest extra energy in order to push the bulging graphene fold in the scan direction. This scenario has been used to explain the observed friction contrast between bilayer and single layer graphene [73], because of the higher adhesion of the tip with the latter, and thus the stronger puckering effect [e.g. 75]. Systematic AFM studies for different layered materials showed that this puckering is a universal phenomenon for weakly adhering or freely suspended materials. In turn, it is suppressed for strongly adhering substrates [74]. A reduction of the puckering effect on the copper oxide with respect to unoxidized copper may explain the observed further lowering of the friction force in our experiments. Figure 6.9 provides an artist impression of the puckering effect, superimposed on the topographic landscape that was measured by AFM in Fig. 6.8. The upper picture, with the tip making contact with graphene on the bare copper substrate, shows a

stronger puckering than the lower one, for the tip contacting graphene on the copper oxide island. We recognize several mechanisms that could explain this reduced puckering and, hence, reduced friction on copper oxide.

Due to the tensile strain in the graphene lattice on top of the copper oxide, the wrinkles, created in contact with the tip, should become less pronounced or even disappear. Thus, less energy would be required to move them in the lateral direction, in contrast to unstrained graphene on bare copper.

The next effect directly influences the strength of the puckering effect and involves the adhesion between the graphene and its substrate. The adhesion between graphene and bare copper is extremely modest, which makes it easy to develop a significant puckering effect. In earlier studies [77-79] it was demonstrated that a monolayer graphene exhibits strong adhesion to Al_2O_3 and Si_2O, the adhesion energies being almost equally high as that of graphene on Fe [63]. We expect that the adhesion of graphene on copper oxide can be even stronger, since the adhesion force is known to grow with increasing dielectric constant of the substrate and the value for copper oxide is much higher than that of silicon oxide; $\varepsilon_{Cu_2O} = 18.1$ versus $\varepsilon_{Si_2O} = 3.5$ [77]. Generally, the nanoscale friction of graphene is rather sensitive to the level of adhesion to the substrate, and it becomes significantly lower upon increase of adhesion [80].

Another reason for reduced puckering on the oxide is that a higher substrate roughness may reduce adhesion between the tip and the graphene and thereby suppress the puckering effect between them [76]. The average nanoscale roughness on the graphene on the copper oxide was almost 2 times as large as that on graphene on bare copper; we measured root mean square height variations of $0.7\ nm$ versus $0.4\ nm$, respectively.

Based on the experiments presented in this chapter, we cannot distinguish between these contributions to the reduction of the friction on graphene on copper oxide. For this purpose, additional experiments would be required. For example, comparing friction on transferred graphene on (oxidized) copper with measurements on the strained graphene on the aged, and partly oxidized samples, one should be able to isolate the effect of the tensile strain of the graphene. A comparison of the friction on oxides or oxide regions with different roughness should make it possible to determine the influence of the roughness directly.

Knowing these two contributions, one should be able to estimate the importance of the adhesion effect for this case.
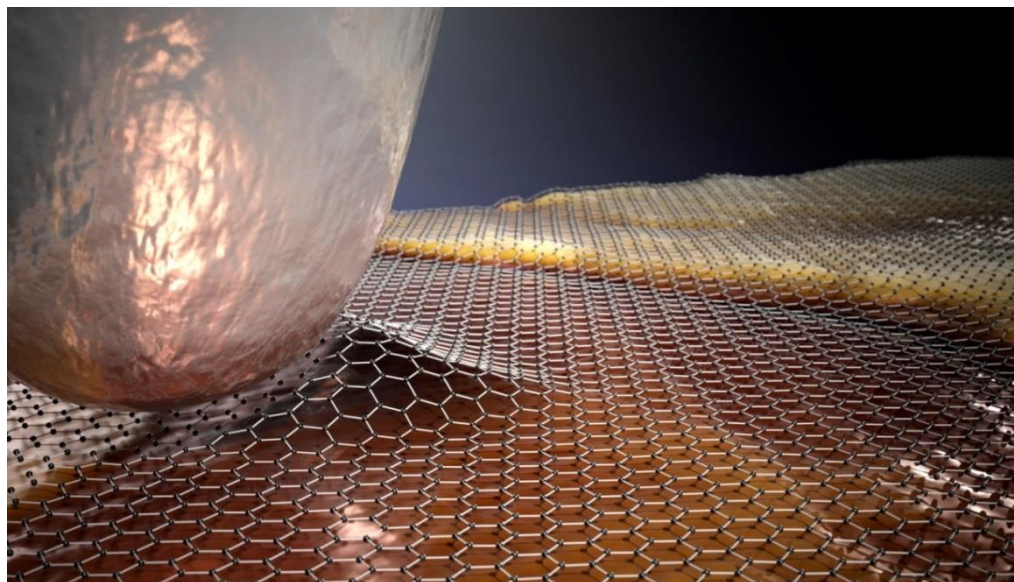
a)
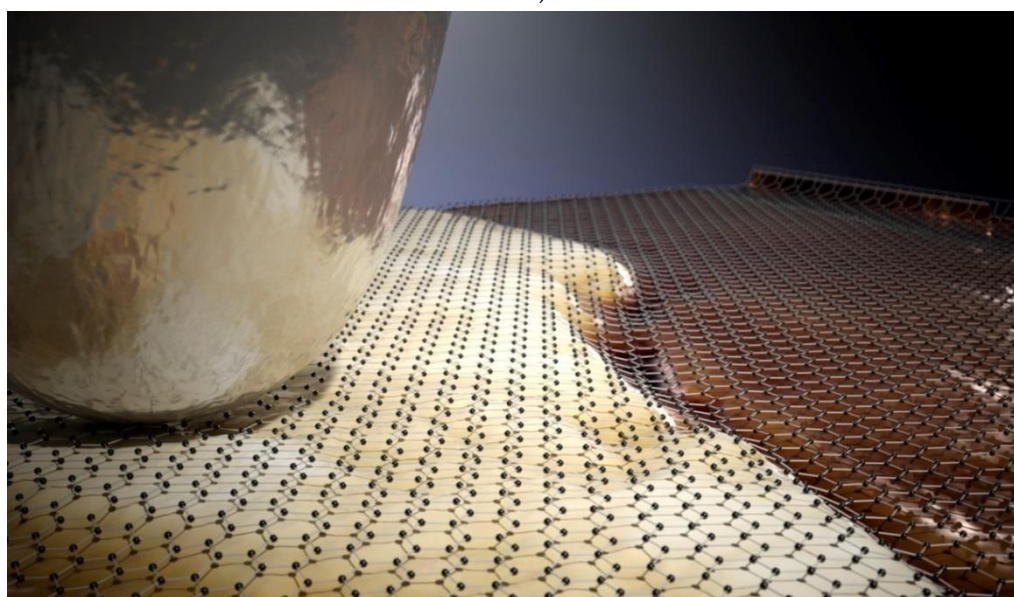
b)

Figure 6.9. Artist impression of the origin of the difference in friction behavior observed in Fig. 8 between graphene on copper and graphene on copper oxide. (a) Loosely adhering graphene on a bare copper substrate tends to bulge up in front of the tip, which leads to higher friction; (b) Tensile strain, stronger graphene-substrate adhesion and larger substrate roughness all suppress the "puckering effect" for graphene on copper oxide; this leads to lower friction.

6.5 Summary

In this chapter, we demonstrated that the presence of a single monolayer of graphene on copper surfaces reduces the sliding friction force between them in ambient by approximately a factor 3 compared to the friction between bare copper surfaces and that it also has a great impact on the static friction behavior. This reduction was shown for surfaces that were completely covered by a monolayer of high-quality graphene. It introduces low surface free energies, minimizes the interaction between contacting asperities, enhances the load capacity and, presumably, causes structural lubricity (superlubricity).

We have not been able to obtain direct experimental evidence that the beneficial effect of the graphene on copper is entirely or partly due to structural lubricity. Angle-dependent measurements did not show a signature of rotational symmetry, which we ascribe to the width of the distribution of domain orientations in the graphene layers that is currently present in even the best large-area graphene samples.

We demonstrated a significant lowering of the friction coefficient measured with friction force microscopy on graphene on top of a locally oxidized copper substrate and we ascribe this to a reduction of the so-called "puckering effect", that otherwise makes the graphene bulge strongly in front of the sliding tip. The increased volume of the copper oxide resulted in tensile strain in the graphene. Next to this tensile strain, also the increased interaction between the graphene and the oxidized substrate and the reduced interaction of the tip with the rougher landscape of the graphene-covered oxide can have made the puckering effect smaller.

Further experiments will be required to distinguish the individual roles of the above effects and to identify other sources of influence on the spectacular, lubricating properties of graphene that were demonstrated here. We believe that our observations may bring new insights in certain technological processes and that they carry the promise to contribute to future developments towards tunable interaction and tunable friction between surfaces.

6.6 Bibliography

1. Novoselov, K.S *et al*. Electric Field effects in Atomically thin carbon films. *Science* **306**, pp. 666-669 (2004)

2. Geim, A.K. & Novoselov, K.S. The rise of graphene. *Nature Materials* **6**, pp. 183-191 (2007)

3. Wallace, P.R. The Band Theory of Graphite. *Physical Review* **71**, pp. 622-634 (1947)

4. Garg, R. *et al*. Work function engeneering in graphene. *Nanomaterials* **4**, pp. 267-300 (2014)

5. Lee, C. *et al*. Measurement of the elastic properties and intrinsic strength of monolayer graphene. *Science* **321**, 358-8 (2008)

6. Xu, X. *et al.* Length-dependent thermal conductivity in suspended single-layer graphene. *Nature Communications* **5**, 3689 (2014)

7. Pop, E., Varshney, V. & Roy, A. Thermal properties of graphene: Fundamentals and applications. *MRS Bulletin* **37**, pp. 1273-1281 (2012)

8. Novoselov *et al.* A roadmap for graphene. *Nature* **490**, pp. 192-200 (2012)

9. Ghosh *et al.* Extremely high thermal conductivity of graphene: Prospects for thermal management applications in nanoelectronic circuits. *Applied Physics Letters* **92**, 151911 (2008)

10. Moser, J., Barreiro, A. & Bachtold, A. Current-induced cleaning of graphene. *arXiv* (2007). doi:10.1063/1.2789673

11. Mayorov, A. *et al.* Micrometer-Scale Ballistic Transport in Encapsulated Graphene at Room Temperature. *Nano Lett* **11**, pp. 2396-2399 (2011)

12. Bunch, S. *et al.* Impermeable Atomic Membranes from Graphene Sheets. *Nano Letters* **8**, pp. 2458-2462 (2008)

13. Chen, S. *et al.* Oxidation Resistance of Graphene-Coated Cu and Cu/Ni Alloy. *ACS Nano* **5**, pp. 1321-1327 (2011)

14. Loh, K., Bao, Q., Ang, P. & Yang, J. The chemistry of graphene. *Journal of Materials Chemistry* **20**, pp. 2277-2289 (2010)

15. Britnell, L. *et al*. Field-Effect Tunneling Transistor Based on Vertical Graphene Heterostructures. *Science* **335**, 947-50 (2012)

16. Schwierz, F. Graphene transistors. *Nature Nanotechnology* **5**, pp. 487-496 (2010)

17. Zhang, H., Gruner, G., & Zhao, Y. Recent advancements of graphene in biomedicine. *Journal of Materials Chemistry B* **1**, 2542 (2013)

18. Wang, X., Zhi, L. & Müllen, K. Transparent, Conductive Graphene Electrodes for Dye-Sensitized Solar Cells. *Nano Letters* **8**, pp. 323-327 (2008)

19. Penkov, O., Kim, H.-J., Kim, H.-J. & Kim, D.-E. Tribology of graphene: A review. *International Journal of Precision Engineering and Manufacturing* **15**, pp. 577-585 (2014)

20. Egberts, P., Han, G., Liu, X., Johnson, C. & Carpick, R. Frictional Behavior of Atomically Thin Sheets: Hexagonal-Shaped Graphene Islands Grown on Copper by Chemical Vapor Deposition. *ACS Nano* **8**, pp. 5010-5021 (2014)

21. Marsden. A.J. *et al*. Friction force microscopy : a simple technique for identifying graphene on rough substrates and mapping the orientation of graphene grains on copper. *Nanotechnology* **24**, 25 (2013)

22. Choi, J.S. *et al*. Friction Anisotropy – Driven Domain Imaging on Exfoliated Monolayer Graphene. *Science* **233**, 607-10 (2011)

23. Li, X. *et al*. Large-Area synthesis of high-quality and uniform graphene films on copper foils. *Science* **324**, pp. 1312-1314 (2009)

24. Li, B., Pan, G., Awan, S. & Avent, N. Techniques for Production of Large Area Graphene for Electronic and Sensor Device Applications. *Graphene and 2D Materials* **1**, pp. 47-58 (2014)

25. Berman, D., Erdemir, A. & Sumant, A. Graphene: a new emerging lubricant. *Materials Today* **17**, pp. 31-42 (2014)

26. Berman, D., Erdemir, A. & Sumant, A. Reduced wear and friction enabled by graphene layers on sliding steel surfaces in dry nitrogen. *Carbon* **59**, pp. 167-175 (2013)

27. Mao, F., Wiklund, U., Andersson, A. & Jansson, U. Graphene as a lubricant on Ag for electrical contact applications. *Journal of Material Science* **50**, pp. 6518-6525 (2015)

28. Kim, K.-S. *et al.* Chemical Vapor Deposition-Grown Graphene: The Thinnest Solid Lubricant. *ACS Nano* **5**, pp. 5107-5114 (2011)

29. Berman, D. *et al*. Macroscale superlubricity enabled by graphene nanoscroll formation. *Science* **348**, pp. 1118-1122 (2015)

30. Hirano, M. Atomistic locking and friction. *Physical Review B* **41**, 11837 (1990)

31.   Hirano, M., Shinjo, K., Kaneko, R. & Murata, Y. Anisotropy of frictional forces in muscovite mica. *Physical Review Letters* **67**, pp. 2642-2645 (1991)

32.   Shinjo, K. & Hirano, M. Dynamics of friction: superlubric state. *Surface Science* **283**, pp. 473-478 (1993)

33.   Hirano, M. *et al*. Observation of Superlubricity by Scanning Tunneling Microscopy. *Physical Review Letters* **78**, 1448 (1997)

34.   Martin, J.M., Donnet, C. & Mogne, Th. Superlubricity of MoS2. *Physical Review B* **48**, 10583 (1993)

35.   Dienwiebel, M. *et al.* Superlubricity of graphite. *Physical review letters* **92**, 126101 (2004)

36.   Liu, Z. *et al.* Observation of Microscale Superlubricity in Graphite. *Physical Review Letters* **108**, 205503 (2012)

37.   Koren, E. *et al*. Adhesion and friction in mesoscopic graphite contacts. *Surface Science* **348**, 6235 (2015)

38.   Pitenis, A., Dowson, D. & Sawyer, G. Leonardo da Vinci's Friction Experiments: An Old Story Acknowledged and Repeated. *Tribology Letters* **56**, pp. 509-515 (2014)

39.   http://appliednanolayers.com/ Visited on 08 February 2017

40.   http://repository.upenn.edu/cgi/viewcontent.cgi?article=1000&context=scn_tooldata Visited on 08 February 2017

41.   https://www.disco.co.jp/eg/products/blade/vt07.html Visited on 08 February 2017

42.   Ying Wang, Y. *et al.* Raman Studies of Monolayer Graphene: The Substrate Effect. *The Journal of Physical Chemistry C* **112**, pp. 10637-10640 (2008)

43.   Malard, L.M. *et al*. Raman spectroscopy in graphene. *Physical Reports* **473**, pp. 51-87 (2009)

44.   Costa, S. *et al.* Resonant Raman spectroscopy of graphene grown on copper substrates. *Solid State Communications* **152**, pp. 1317-1320 (2012)

45.   Platzman, I., Brener, R., Haick, H. & Tannenbaum, R. Oxidation of Polycrystalline Copper Thin Films at Ambient Conditions. *The Journal of Physical Chemistry C* **112**, pp. 1101-1108 (2008)

46.   Feng, X., Kwon, S., Park, J. & Salmeron, M. Superlubric Sliding of Graphene Nanoflakes on Graphene. *ACS Nano* **7**, pp. 1718-1724 (2013)

47. Demirbaş, T. & Baykara, M. Nanoscale tribology of graphene grown by chemical vapor deposition and transferred onto silicon oxide substrates. *Journal of Materials Research* **31**, pp. 1914-1923 (2016)

48. Lee, H., Lee, N., Seo, Y., Eom, J. & Lee, S. Comparison of frictional forces on graphene and graphite. *Nanotechnology* **20**, 325701 (2009)

49. Filleter *et al.* Friction and Dissipation in Epitaxial Graphene Films. *Physical Review Letters* **102**, 086102 (2009)

50. Deng, Z., Smolyanitsky, A., Li, Q., Feng, X.-Q. & Cannara, R. Adhesion-dependent negative friction coefficient on chemically modified graphite at the nanoscale. *Nature Materials* **11**, pp. 1032-1037 (2012)

51. Marchetto, D., Feser, T. & Dienwiebel, M. Microscale study of frictional properties of graphene in ultra high vacuum. *Friction* **3**, pp. 161-169 (2015)

52. Marchetto *et al.* Friction and Wear on Single-Layer Epitaxial Graphene in Multi-Asperity Contacts. *Tribology Letters* **48**, pp. 77-82 (2012)

53. Kim, K. *et al.* Multiply folded graphene. *Physical Review B* **83**, 245433 (2011)

54. Duong, D. *et al.* Probing graphene grain boundaries with optical microscopy. *Nature* **490**, pp. 235-239 (2012)

55. Choi, J.L. & Gethin, D.T. Simulation of atomic force microscopy operation via three-dimensional finite element modelling. *Nanotechnology* **20**, 065702 (2009)

56. Cannara, R., Eglin, M. & Carpick, R. Lateral force calibration in atomic force microscopy: A new lateral force calibration method and general guidelines for optimization. *Review of Scientific Instruments* 77, 053701 (2006)

57. Huang, M. *et al.* Phonon softening and crystallographic orientation of strained graphene studied by Raman spectroscopy. *Proceedings of the National Academy of Sciences* **106**, pp. 7304-7308 (2009)

58. Yin, X. *et al.* Evolution of the Raman spectrum of graphene grown on copper upon oxidation of the substrate. *Nano Research* 7, pp. 1613-1622 (2014)

59. Capasso *et al.* Graphene ripples generated by grain boundaries in highly ordered pyrolytic graphite. *Carbon* **68**, pp. 330-336 (2014)

60. Palacio, M. & Bhushan, B. Normal and Lateral Force Calibration Techniques for AFM Cantilevers. *Critical Reviews in Solid State and Materials Sciences* **35**, pp. 73-104 (2010)

61. Singh, E. *et al.* Graphene Drape Minimizes the Pinning and Hysteresis of Water Drops on Nanotextured Rough Surfaces. *ACS Nano* **7**, pp. 3512-3521 (2013)

62. Meyer, E., Overney, R.M., Dransfeld, K., & Gyalog T., Nanoscience: Friction and Rheology on the Nanometer Scale. *World Scientific Publishing*, Singapore (1998)

63. Restuccia, P. & Righi, M.C. Tribochemistry of graphene on iron and its possible role in lubrication of steel. *arXiv* (2016). doi:10.1016/j.carbon.2016.05.025

64. Klemenz, A. *et al.* Atomic Scale Mechanisms of Friction Reduction and Wear Protection by Graphene. *Nano Letters* **14**, pp. 7145-7152 (2014)

65. Zhang, Q., Diao, D. & Yang, L. Dangling bond induced cross-linking model in nanoscratched graphene layers. *Surface and Coatings Technology* **237**, pp. 230-233 (2013)

66. Berman, D., Deshmukh, S., Sankaranarayanan, S., Erdemir, A. & Sumant, A. Extraordinary Macroscale Wear Resistance of One Atom Thick Graphene Layer. *Advanced Functional Materials* **24**, pp. 6640-6646 (2014)

67. Baumberger, T. & Caroli, C. Solid friction from stick slip down to pinning and aging. *ArXiv,* doi: 10.1080/00018730600732186 (2005)

68. Lahiri, J. *et al.* Graphene growth and stability at nickel surfaces. *New Journal of Physics* **13**, 025001 (2011)

69. He, Y. *et al*. Anomalous interface adhesion of graphene membranes. *Scientific Reports* **3**, 2660 (2013)

70. Wintterlin, J. & Bocquet, M.-L. Graphene on metal surfaces. *Surface Science* **603**, pp. 1841-1852 (2009)

71. Das, S., Lahiri, D., Lee, D.-Y., Agarwal, A. & Choi, W. Measurements of the adhesion energy of graphene to metallic substrates. *Carbon* **59**, pp. 121-129 (2013)

72. Won, M.-S., Penkov, O. & Kim, D.-E. Durability and degradation mechanism of graphene coatings deposited on Cu substrates under dry contact sliding. *Carbon* **54**, pp. 472-481 (2013)

73.	Filleter, T. & Bennewitz, R. Structural and frictional properties of graphene films on SiC(0001) studied by atomic force microscopy. *Physical Review B* **81**, 155412 (2010)

74.	Lee, C. *et al* Frictional Characteristics of Atomically Thin Sheets. *Science* **328**, pp. 76-80 (2010)

75.	Lee, C. *et al.* Elastic and frictional properties of graphene. *Physica Status Solidi (b)* **246**, pp. 2562-2567 (2009)

76.	Spear, J.C. *et al*. The influence of nanoscale roughness and substrate chemistry on the frictional properties of single and few layer graphene. *Nanoscale* 7, 10021 (2015)

77.	Song, S. & Cho, B. Investigation of interaction between graphene and dielectrics. *Nanotechnology* **21**, 335706 (2010)

78.	Koenig, S., Boddeti, N., Dunn, M. & Bunch, S. Ultrastrong adhesion of graphene membranes. *Nature Nanotechnology* **6**, pp. 543-546 (2011)

79.	Das, S. *et al*. Interfacial bonding characteristics between graphene and dielectric substrates. *Nanotechnology* **25**, 045707 (2014)

80.	Berman, D., Erdemir, A., Zinovev, A. & Sumant, A. Nanoscale friction properties of graphene and graphene oxide. *Diamond and Related Materials* **54**, pp. 91-96 (2015)

81.	Verhoeven, G., Dienwiebel, M. & Frenken, J. Model calculations of superlubricity of graphite. *Physical Review B* **70**, 165418 (2004)

82.	De Wit, M. Antonov, P., van Baarle, D. & Frenken., J. On slippery ground: towards superlubricity of graphene. *MSc Thesis*, University of Leiden (2013)

83.	Strictly speaking, the rotation symmetry of the graphite lattice is 120° rather than 60°. However, it is only in the local stacking of the layers that the symmetry is broken from 60° to 120°, which implies that two contacting graphite lattices do lock in every 60° and that there may be a modest modulation in the strength of this effect, such that even multiples of 60° lead to somewhat more friction than odd multiples.

Summary

The phenomenon of friction forms one of the oldest subjects in the history of science and engineering. Even now, many intriguing questions remain to be answered about the contact dynamics of solid interfaces and their behavior at different geometrical scales and under different atmospheric and lubrication conditions. With ever more demanding requirements to efficiency and lifetime of nano- and microelectromechanical systems and to other high-tech devices, the importance of understanding and control of friction and wear increases too. Growing technological requirements for ultra-low friction and wear-rate coefficients as well as precise motion control open new horizons for research into new, revolutionary concepts in lubrication.

In this PhD thesis, I described our work towards reduction and control of dry friction with solutions that promise to meet some of the challenges set by modern technology. In particular, I demonstrated three attempts to make unique nanoscale lubrication phenomena active on the macroscopic scale. In **Chapter 2**, I introduced first experiments to reduce friction in macroscopic contacts, employing the atomic-scale effect of thermolubricity. We used arrays of silicon nanopillars (NPs) that were dimensioned such that each would mimic the mechanical behavior of the apex of a single tip in a Friction Force Microscope (FFM): namely combining a high lateral vibration frequency with a relatively large thermal vibration amplitude, of a significant fraction of an interatomic distance, at room temperature. In **Chapter 3,** I demonstrated how to apply conventional cleanroom techniques to produce large, highly reproducible and well-ordered arrays of such NPs. The philosophy behind the NP approach was to introduce a multitude of thermally activated mechanical contacts on a macroscopic area and translate them all by the low-friction scenario due to thermal vibrations known for a single FFM tip apex. In practice, along with the high mechanical strength and surprising flexibility of the NPs, the first friction experiments demonstrated that the contact area between a slider and the NP array plays a crucial role and that this area should be made as large as possible. Experiments with an Atomic Force Microscope (AFM), using a ball-shape probe as the sliding body, showed that even for a large radius, the ball had sufficient freedom to 'sink' in significantly between the NPs. The NPs were

found to bend sideways, which we expect to lead to severe damping of the thermal fluctuations of the NPs. We proposed a larger NP array of several square centimeters as the next step towards realization of thermolubricity on the macroscopic scale. This should allow one to use larger slider surfaces and minimize alignment difficulties.

The second effect that I explored to lower friction and that is also rooted in subtle effects on the nanoscopic scale, is lubrication with graphite. In contrast with thermolubricity, this lubrication mechanism is well known on the practical, macroscopic scale, that we make use of in everyday life. Materials with a structure like graphite, i.e., with strong atomic layers that weakly interact with each other, enable low friction due to the ease of sliding of these layers over each other. In **Chapter** 4 of this thesis, I also associate this graphitic behavior with the ultralow friction of another solid material that doesn't have intrinsic graphite-like properties, namely Diamond-Like Carbon (DLC). Essential in my approach to unravel the lubrication mechanism of DLC was micropatterning of the studied contacts. This enabled us to strongly limit the apparent area of contact and directly observe the origin and the build-up of an ensemble of third-body elements during sliding. By imaging the contacting surfaces at various stages in the sliding process, we found that the sliding quickly leads to the formation of DLC microparticles that break up into nanoparticles and to subtle transformations of the highest asperities of the DLC surface, both of which we attribute to the high local shear stress levels. Friction on these nanoparticles and modified asperities was found to be much lower than on the rest of the DLC surface. Local Raman spectroscopy showed an increased proportion of sp^2-bonding on the particles and the high regions, which is indicative of local graphitization. We concluded that the first sliding on a DLC surface leads to mechanical and chemical changes towards a more graphitic form of amorphous carbon, which naturally introduces the scenario of graphite lubrication.

In **Chapter 5**, I showed that the friction properties of the investigated, hydrogenated DLC coating in dry and humid environments are surprisingly different from common tribological behavior of this type of coatings. We ascribed this difference largely to the unusual geometry of our experiment: in our measurements, most microcontacts do not leave the actual sliding interface, which is due to the combination of the micropatterned DLC substrate and the ultraflat,

silicon counter-surface, that we used as the slider. This geometry accelerated the formation of the third-body elements and their graphitization. We further showed that water adsorbed from a mildly humid environment can play a lubricating role for the graphitized DLC clusters at low sliding velocities, which we ascribe to capillary condensation of water between them and their DLC substrate. At high humidities, friction is lowered even further, suggesting a hydrodynamic contribution, i.e., water acting directly as a lubricant, for example due to the formation of capillary bridges at the sliding interface between the graphitized DLC particles and DLC asperities and the silicon wafer.

On the atomic scale, the phenomenon underlying graphite lubrication is probably structural lubricity, also known as superlubricity. It is the effect that two perfectly smooth and stiff lattice planes that are incommensurate with each other and only weakly interact can slide over each other with nearly zero friction. Even though this effect has been identified experimentally only on the nanometer scale, graphene, graphite and structurally similar materials should be expected to all exhibit this self-lubricating behavior, also on larger scales. In **Chapter 6**, I reported the results of an experiment to demonstrate structural lubricity on the macroscopic scale. Large-area copper surfaces, completely covered with a high-quality monolayer of graphene, were chosen as the best candidates for this study. We demonstrated that covering copper surfaces with a single monolayer of graphene reduces the sliding friction force between them in ambient by approximately a factor 3, in comparison with bare copper surfaces. We also found a great impact of the graphene on the static friction behavior. The graphene introduces low surface free energies, minimizes the interaction between contacting asperities, enhances the load capacity and, presumably, only locally causes structural lubricity. Unfortunately, even on these low-defect-density surfaces we have not been able to acquire direct proof of the lattice-mismatch mechanism of this friction lowering, by distinguishing a signature of 60° rotational symmetry in angle-dependent friction measurements. The sharp maxima in the friction force, expected every 60°, were simply washed out by the residual width of the distribution of domain orientations in the graphene layers.

Finally, we demonstrated a significant additional lowering of the friction coefficient measured with FFM on graphene on top of a locally oxidized copper substrate. We ascribe this to a reduction of the so-called "puckering effect" that

otherwise makes the graphene bulge strongly in front of the sliding tip. The increased volume of the copper oxide resulted in tensile strain in the graphene. We propose that in addition to this tensile strain, also the increased adhesion between the graphene and the oxidized substrate and the reduced interaction of the tip with the rougher landscape of the graphene-covered oxide made the puckering effect smaller.

The observations presented in this thesis provide new fundamental insights that are of potential relevance to several technological processes. They carry the promise to contribute to future developments towards tunable interaction and tunable friction between surfaces on various length scales.

Samenvatting

Het verschijnsel wrijving vormt een van de oudste onderwerpen in de geschiedenis van wetenschap en techniek. Toch blijven nog steeds veel intrigerende vragen onbeantwoord over de contactdynamica van vaste stoffen en hun mechanische gedrag op verschillende geometrische lengteschalen en over de invloeden van de atmosferische omstandigheden en van smeringsmiddelen. Nu steeds verdergaande eisen worden gesteld aan de efficiëntie en levensduur van nano- en micro-elektromechanische systemen en andere hightech-apparaten, neemt ook het belang van begrip van en controle over wrijving en slijtage toe. De vraag naar ultra-lage wrijvings- en slijtagecoëfficiënten opent nieuwe horizonten voor onderzoek naar nieuwe, revolutionaire concepten in smering.

In dit proefschrift beschreef ik ons onderzoek aan nieuwe mogelijkheden voor reductie en controle van z.g. 'droge' wrijving, d.w.z. wrijving in afwezigheid van vloeibare smeermiddelen zoals olie. Ik heb me daarbij geconcentreerd op drie unieke smeringsverschijnselen, die elk werkzaam zijn op de nanometerschaal, in een poging om deze juist in te zetten op de macroscopische schaal van millimeters en centimeters. In Hoofdstuk 2 introduceerde ik de eerste experimenten om wrijving in macroscopische contacten te verminderen, door gebruik te maken van een effect op de atomaire schaal dat bekend staat onder de naam *thermolubriciteit*. Ik paste hierbij regelmatige structuren toe van silicium nanopilaren (NP's) die zodanig waren gedimensioneerd dat elke pilaar het mechanische gedrag zou nabootsen van het uiterste puntje van de naald in een atomaire-kracht- of wrijvingskrachtmicroscoop (FFM). Dit gedrag wordt gekenmerkt door de combinatie van een hoge zijdelingse trillingsfrequentie, in het bereik van 1 GHz of meer, met een relatief grote thermische trillingsamplitude bij kamertemperatuur, minimaal een significante fractie van een interatomaire afstand. In Hoofdstuk 3 heb ik laten zien hoe conventionele cleanroomtechnieken kunnen worden ingezet om grote, zeer reproduceerbare rijen van silicium NP's te produceren. De filosofie van de NP-aanpak was om een macroscopisch contactoppervlak volledig uit te voeren in de vorm van een groot aantal thermisch geactiveerde, mechanische contacten, die alle met lage wrijving kunnen transleren vanwege het thermische vibratie-effect dat eerder is waargenomen voor één individuele FFM-naaldpunt.

Onze experimenten toonden aan dat de NP's mechanisch zeer sterk zijn en verrassend flexibel. Eerste wrijvingsmetingen lieten zien dat het cruciaal is om het contactgebied zo groot mogelijk te maken tussen het veld met de NP's en het object dat daaroverheen moet schuiven. Zo bleek in experimenten met een atoomkrachtmicroscoop (AFM), waarin een balvormig object werd gebruikt als glijlichaam, dat zelfs een bal met een relatief grote diameter voldoende vrijheid had om significant in te zinken tussen de NP's. De NP's bleken hierbij zijwaarts te buigen. Naar onze verwachting leidt het tot een ernstige demping van de beweging van de NP's, waardoor het thermische smeringseffect verloren gaat. Als volgende stap naar de realisatie van thermolubriciteit op macroscopische schaal, stellen we een uitbreiding voor naar nog grotere velden met NP's, bijvoorbeeld van meerdere vierkante centimeters. Hierdoor worden weliswaar grotere schuifoppervlakken mogelijk, maar wordt tegelijkertijd wel een lastig uitlijningsprobleem geïntroduceerd.

Het tweede effect dat ik onderzocht heb om wrijving te verlagen, is smering met grafiet. In tegenstelling tot thermolubriciteit, is grafietsmering goed bekend op de praktische, macroscopische schaal, die we in het dagelijks leven gebruiken. Materialen met een structuur zoals grafiet, d.w.z. met sterke atoomlagen die met elkaar slechts een zwakke interactie hebben, maken een lage wrijving mogelijk dankzij het gemak waarmee deze atoomlagen over elkaar glijden. In Hoofdstuk 4 van dit proefschrift associeer ik dit gedrag van grafiet met de lage wrijving van een ander vast materiaal dat zelf geen intrinsieke grafietachtige eigenschappen heeft, namelijk Diamond-Like Carbon (DLC), een amorfe vorm van koolstof met een diamantachtig karakter. Essentieel in mijn aanpak om het smeringsmechanisme van DLC te ontrafelen was de microstructurering van de bestudeerde contacten. Dit zorgde ervoor dat we het contactoppervlak sterk konden beperken en de oorsprong en de opbouw konden volgen van slijtagedeeltjes – de zogenaamde 'third bodies'. Door de contactvlakken te bestuderen na verschillende stappen van het glijproces, vonden we dat het glijden snel leidt tot de vorming van DLC-microdeeltjes die vervolgens in nanodeeltjes kunnen opbreken. Daarnaast vonden we ook subtiele veranderingen in structuur en gedrag van de hoogst uitstekende delen van het DLC-oppervlak, die waarschijnlijk ook in contact waren gekomen met het tegenoppervlak. Beide effecten associëren wij met de hoge, lokale druk, zowel loodrecht op het contactvlak als parallel daaraan. De wrijving bleek op deze

nanodeeltjes en gewijzigde contactgebieden veel lager te zijn dan op de rest van het DLC oppervlak. Lokale raman-spectroscopie bracht een verhoogd aandeel aan het daglicht van sp^2-bindingen tussen de koolstofatomen op deze plekken. Dat type bindingen vormt een sterke aanwijzing voor de vorming van grafiet. We concluderen dat de eerste glijbewegingen over een DLC-oppervlak leiden tot mechanische en chemische veranderingen van de DLC-coating van een diamantachtig karakter naar een meer grafietachtige vorm. Het is deze grafietvorm die de wrijving verlaagt, zoals we dat van grafiet gewend zijn (zie hierboven), precies op die plaatsen waar de DLC-coating in contact komt met het tegenoppervlak.

In Hoofdstuk 5 heb ik laten zien dat de wrijvingseigenschappen van een gehydrogeneerde DLC-coating in droge en vochtige omgevingen verrassend sterk kunnen afwijken van het typische, tribologische gedrag van dit soort coatings. We hebben dit verschil toegeschreven aan de unieke geometrie van ons experiment: in onze metingen blijven de meeste microcontacten voortdurend bestaan, als gevolg van de combinatie van het microgestructureerde DLC-substraat en het ultravlakke, daar overheen glijdende silicium-oppervlak. Deze geometrie versnelde de vorming van de 'third-body' elementen en van grafiet. Verder bleek vanuit de vochtige omgeving gecondenseerd water bij lage glijsnelheden een smerende rol te kunnen spelen voor de gegrafitizeerde DLC clusters. Wij associëren dit effect met capillaire condensatie van water tussen deze clusters en het DLC-substraat; de clusters plakten er daardoor extra goed aan vast. Bij hoge vochtigheid werd de wrijving nog verder verlaagd. Wij schrijven dat toe aan het hydrodynamische gedrag van water dat direct als een smeermiddel optreedt als zich capillaire bruggen vormen tussen de gegrafitizeerde DLC-deeltjes en de hoogste DLC-contactgebieden aan de ene kant en het siliciumoppervlak aan de andere.

Dat de wrijving van grafiet zo laag is, is waarschijnlijk voor een belangrijk deel toe te schrijven aan een structureel effect op de atomaire schaal, dat bekend staat onder de namen *superlubriciteit* en *structurele lubriciteit*. Het is het verschijnsel dat twee perfecte roostervlakken, die niet op elkaar passen, vrijwel zonder wrijving over elkaar kunnen glijden. Hoewel dit effect op experimentele wijze alleen op de nanometerschaal is aangetoond, vertonen grafeen, grafiet en structureel vergelijkbare materialen dit smeringsmechanisme mogelijk ook op grotere lengteschalen. In Hoofdstuk 6 rapporteerde ik de resultaten van een

experiment om structurele lubriciteit op de macroscopische schaal aan te tonen. Wij hebben als optimale 'kandidaat' voor deze studie gekozen voor grote koperoppervlakken, die volledig bedekt waren met een hoogwaardige monolaag van grafeen. We hebben laten zien dat de aanwezigheid van het grafeen de wrijvingskracht tussen de koperoppervlakken vermindert met ongeveer een factor 3. Niet alleen de dynamische wrijvingskracht was sterk verlaagd, maar ook het statische wrijvingsgedrag werd door het grafeen veranderd. Deze waarnemingen kloppen met de verwachting dat het grafeen lage oppervlakte-vrije-energieën introduceert, de wisselwerking tussen de contacten minimaliseert, de laadcapaciteit verbetert en superlubriciteit veroorzaakt. Helaas is het ons, ondanks de goede kwaliteit van het gebruikte grafeen, niet gelukt om direct bewijs te verkrijgen voor het rooster-gerelateerde smeringsmechanisme. Met name was er geen teken van 60° rotatiesymmetrie in de hoekafhankelijke wrijvingsmetingen. De scherpe maxima in de wrijvingskracht, die elke 60° zouden moeten optreden, werden uitgesmeerd door de breedte van de verdeling van domeinoriëntaties in de grafeenlagen.

Tenslotte, maten wij een significante, extra verlaging van de wrijvingscoëfficiënt met FFM op grafeen op een plaatselijk geoxideerd kopersubstraat. We schrijven deze extra verlaging toe aan een vermindering van het zogenaamde *rimpeleffect*, waardoor het grafeen zich voor de FFM-naald omhoog kan plooien. Het verhoogde volume van het koperoxide resulteerde waarschijnlijk in extra trekspanning in het grafeen. We denken dat er naast deze trekspanning ook andere effecten een rol spelen die de wrijving op het grafeen verlagen op de geoxideerde plekken. Met name zijn het de sterkere adhesie tussen het grafeen en het geoxideerde substraat en de verminderde wisselwerking van de FFM-naald met het ruwere landschap van het grafeenbedekte oxide, die het rimpeleffect kleiner maken.

De in dit proefschrift beschreven experimenten leveren nieuwe fundamentele inzichten op, die van mogelijk belang zijn voor verschillende technologische processen. Ze leveren een bijdrage aan toekomstige ontwikkelingen op het terrein van instelbare interactie, wrijving en slijtage tussen oppervlakken op verschillende lengteschalen, van atomair tot macroscopisch.

List of publications

1.Yanson, A.I., Antonov, P.V., Rodriguez, P. & Koper, M. Influence of the electrolyte concentration on the size and shape of platinum nanoparticles synthesized by cathodic corrosion. *Electrochimica Acta* **112**, pp. 913-918 (2013)

2.Yanson, A.I., Antonov, P.V., Yanson, Y.I. & Koper, M. Controlling the size of platinum nanoparticles prepared by cathodic corrosion. *Electrochimica Acta* **110**, pp. 796-800 (2013)

3.Antonov, P.V., Zuiddam, M.R. & Frenken, J.W.M. Fabrication of high-aspect ratio silicon nanopillars for tribological experiments. *Journal of Micro/Nanolithography, MEMS and MOEMS* **14(4)**, 044506 (2015)

4.Antonov, P.V. & Frenken, J.W.M. Towards thermolubricity on silicon nanopillar subsrates: contact dynamics and effect of relative humidity, in preparation. (Chapter 2 of this thesis)

5.Antonov, P.V. & Frenken, J.W.M. Tribological behaviour of graphene grain boundaries on single crystal copper films, in preparation. (Chapter 6 of this thesis)

6.Antonov, P.V., Valefi, M. & Frenken, J.W.M. Dynamic and static tribological properties of micropatterned DLC under different humidities, in preparation. (Chapter 5 of this thesis)

Acknowledgements

My time as a PhD student at Leiden University and ARCNL was very interesting, challenging and educational. This was also a period over which I was lucky to meet and work with a lot of bright and talented people. Without guidance, advice and support of many of them, the work described in this thesis would not have been possible.

First, I am very grateful to my supervisor, Joost Frenken, for his patient guidance, creative ideas and solutions. Joost, thank you for keeping me inspired and motivated over these years. I am also deeply indebted to Jan Verhoeven for our long and fruitful scientific discussions, his advice and his continuous willingness to help.

Further, I would like to acknowledge Ellie van Rijswijk, Romy Metz, Rosa Andrea and Maria Teuwissen for their administrative support; Arend-Jan van Calcar, Sander van Leeuwen, Hinco Schoenmaker, Emiel Wiegers, Geert Koning and Arjen Geluk for their professional technical assistance; the staff members of Kavli Nanolab (TU Delft) and AMOLF Nanolab for their support and education in nanofabrication; Tijn van Omme, Jaap Kokorian and Merlijn van Spengen for experimental assistance and giving a possibility to use the micro-Raman spectrometer in TU Delf; Richard van Rijn and all from ANL for providing the graphene samples for our study; Mahdiar Valefi, Krijn Bustraan and Wim van der Zande for introduction to ASML and their professional advices. And of course my former colleagues. I am thankful to all of you for sharing your knowledge and all amazing moments we had together: Petr Dudin, Matthijs van Spronsen, Marien Bremmer, Rik Mom, Martin de Wit, Dirk and Gert-Jan van Baarle, Johan Bakker, Violetta Navarro-Paredes, Marc de Voogd, Steven Kleijn, Sander Roobol, Jorinde van de Vis, Christina Sfiligoj, Amir Saedi, Görsel Yetik, Dmitry Kurilovich, Oscar Versolato, Joris Scheers, Renfeng Hu, Alessandro Antoncecchi, Thomas Meijvogel, Reinout Jaarsma and Thomas Cohen Stuart and all others. In particular, I would like to acknowledge Alex Yanson for his continuous support and for introducing me to the Netherlands, to Leiden and to Leiden University in particular.

My dear friends, Yuriy Yanson and Alexandra Hunts, Sergey Bezrukavnikov and Inna Medvedeva, Sergio Paya Gonzalbez and Elena Beletkaia – thank you for

Curriculum Vitae

Pavlo V. Antonov was born on August the 5th, 1990, in Kharkov, Ukraine. There, he attended High School #16, from which he graduated in 2007. That year, Antonov started his academic training at the Physics and Technology Faculty of the Kharkov National University. In 2011 he received his BSc degree in Applied Physics. His first research project focused on magnetron sputtering of thin metal films and on the design of a set-up for ion- and plasma-assisted processing of micro- and nanostructures. This experimental project established a collaboration between the University and the Scientific Center for Physical Technologies, under the supervision of Yuriy Rybalko and Prof. Dr. Vladimir I. Farenik. Antonov continued his MSc studies in Applied Physics at the same faculty. He conducted his final MSc project in 2012 during an internship in the Catalysis and Surface Chemistry group of Prof. Dr. Marc T.M. Koper at the Leiden Institute of Chemistry of Leiden University, The Netherlands. The project, under daily supervision of Dr. Alex Yanson, was devoted to cathodic corrosion of platinum, as a method to synthesize nanoparticles. In February 2013, Antonov graduated with honors from the Kharkov National University.

In October 2012 Antonov joined the Interface Physics group of Prof. Dr. Joost W.M. Frenken at the Huygens-Kamerlingh Onnes Laboratory of Leiden University as a PhD student. His research project was aimed at understanding, controlling and reducing dry, unlubricated friction in macroscopic contacts by means of the inherently atomic-scale effects of thermolubricity and superlubricity. In particular, the project focused on understanding the tribological behavior of artificial nanostructures, of graphene coatings and of diamond-like carbon coatings. In parallel to his own research, Antonov also supervised a number of BSc and MSc student projects aimed at unraveling the physical mechanisms of ice-skating. Shortly after Prof. Dr Joost W.M. Frenken started as the Director of the new Advanced Research Center for Nanolithography (ARCNL) in Amsterdam, early 2014, Antonov also moved to ARCNL, where he continued his PhD research.

During his PhD time, Antonov was a member of the Central Works Council of NWO (FOM) and the first Works Council of ARCNL.

In March 2017, Antonov started as a design engineer at the Research department of ASML in Veldhoven. His work focuses on solving friction and wear problems in the context of modern nanolithography technology.